Alma Mater Studiorum · University of Bologna

School of Science
Department of Physics and Astronomy
Master Degree in Physics

Study of antideuteron production from $\overline{\Lambda}_b$ at the LHC

Supervisor:
Prof. Francesca Bellini

Co-supervisor:
Dr. Nicolò Jacazio

Submitted by:
Marta Razza

Academic Year 2023/2024

Abstract

This thesis presents a study of a newly proposed decay channel of the $\overline{\Lambda}_b$ baryon into antideuterons at the LHC. This analysis is motivated by the implications for the observation of such a channel for indirect dark matter searches and our understanding of antinuclei formation mechanisms via coalescence. In the universe, the production of antinuclei is highly suppressed. Specifically, for kinetic energies per nucleon below 1 GeV/n, the antideuteron flux from astrophysical sources is expected to be approximately three orders of magnitude lower than the predicted flux from processes involving dark matter particles, e.g. Weakly Interacting Massive Particles (WIMPs).

In this study, proton-proton collisions at the highest-reached LHC energy of $\sqrt{s} = 13.6$ TeV are simulated using the Monte Carlo event generator `PYTHIA`, from which the production of $\overline{\Lambda}_b$ is obtained. Coalescence models are then applied to the antinucleons produced in the final state to produce antideuterons. In particular, two coalescence models are presented: one based on a classical description of the process and a state-of-the-art coalescence model based on a quantum mechanical approach. For both models, a first estimate of the branching ratio of the $\overline{\Lambda}_b \to \overline{d} + X$ process is provided, never reported before in the literature. Furthermore, the acceptance of the ALICE and LHCb detectors is compared, evaluating their potential to detect antideuterons produced from $\overline{\Lambda}_b$ decays.

Contents

Introduction

One of the open problems of modern physics is understanding the nature of Dark Matter (DM). Many experimental efforts and techniques are employed to obtain further proof of the existence of DM and the first evidence of a non-gravitational interaction. Considering theoretical models based on the hypothesis that DM particles are the so-called weakly interacting massive particles (WIMPs), one of the possible final states from their annihilation could consist of the formation of quark-antiquark pairs that can lead to the production of antinuclei. A possible signal of "primary" antinuclei produced in DM annihilation and found in cosmic rays would suffer from the background constituted by "secondary" antinuclei produced by the interaction of primary cosmic rays with the interstellar matter. According to current estimates, below a kinetic energy per nucleon of 1 GeV/n, the expected flux of secondary antinuclei is about 1-2 orders of magnitude lower than the expected flux for primary antinuclei, making cosmic antideuterons and antihelium nuclei promising smoking gun for dark matter annihilation in space. In 2018, the Alpha Magnetic Spectrometer (AMS-02) announced the potential detection of 6 events of $^3\overline{\mathrm{He}}$ and 2 events of $^4\overline{\mathrm{He}}$. Thus, if the preliminary observations of AMS-02 were confirmed, they may represent a breakthrough in the searches for cosmic antinuclei. In this rich physics context, a recent and pioneering study focused on the production of antinuclei from the decay of the heavy baryon $\overline{\Lambda}_b$, formed as a consequence of the hadronization of the $\bar{b}$ produced by DM annihilation. At the LHC, we have the opportunity to investigate these processes at $\sqrt{s} = 13.6$ TeV, shedding light on several unresolved aspects of the universe.

The goal of this thesis, in particular, is to obtain a first prediction of the branching ratio of the $\overline{\Lambda}_b \to \overline{d} + X$ channel and to identify possible regions of interest for experimental measurements. Proton-proton collisions are simulated using the Monte Carlo event generator `PYTHIA`, tuned to enhance baryon production over meson production, in particular, the $\overline{\Lambda}_b$. A coalescence-based model is then used to simulate the production of antideuterons formed by antinucleons from $\overline{\Lambda}_b$ decay and from the underlying event, highlighting the significance of the contribution of $\overline{\Lambda}_b$ decays to the overall (anti)nucleon and (anti)deuteron production. The original part of this work consists of the full chain of simulation from the pp collision to the formation of an antideuteron to the estimate of the branching ratio. A final study is conducted to compare the acceptance of the ALICE and LHCb detectors for antideuterons produced from $\overline{\Lambda}_b$ decay, to motivate future measurements at the LHC.

Chapter 1

Antinuclei in cosmic rays and dark matter search

At the beginning of the 20th century, the physicist Victor Hess proved the existence of cosmic rays. During that period, scientists were trying to understand why the radiation present in the environment was greater than what could be produced by natural radioactivity. In 1912, Hess, to solve the puzzle, used an air balloon equipped with an electroscope and demonstrated that the quantity of charged particles increased with altitude. This meant that the unknown radiation did not originate from Earth (like natural radioactivity) but came from outer space, hence the name Cosmic Rays. The cosmic rays were extensively studied, further information is available on them and their composition.
Several years later, in 1929, Paul Dirac, in an attempt to reconcile the new theories of Relativity and Quantum Mechanics, hypothesized that for each negatively charged electron, there should exist a corresponding particle with a positive charge but with equal mass, the positron. Just a few years later, in 1932, Carl D. Anderson [28], while studying cosmic rays using photographic emulsions in a magnetic field, noticed some traces resembling those of electrons but with an apparent wrong curvature; these were positrons. The road for the study of antimatter was opened, and in 1955, the antiproton was observed by Emilio Segrè and Owen Chamberlain [38] at the Lawrence Berkeley National Laboratory and the antineutron was later discovered. At that point, it was logical to think that, just like ordinary matter, antiprotons and antineutrons could form antinuclei, as indeed observed at CERN PS [52] in 1965.

Today, light antinuclei in space are subject of experimental search, and the observation by AMS-02 of few cosmic antihelium candidates is under debate; furthermore, their origin and formation mechanism have to be fully understood. According to state-of-the-art models, antideuteron and antihelium can be produced by hadronic collisions between primary cosmic rays, predominantly protons, and the interstellar medium, mainly composed of hydrogen and helium. On the other hand, extensions of the Standard Model of particle physics predict the possibility of producing antimatter from dark matter, giving a new meaning to its observation.

1.1 Dark Matter

Most of the information about our galaxy, as well as the rest of the Universe, comes mainly from electromagnetic emission. The existence of dark matter, which does

not emit electromagnetic radiation, was inferred indirectly through its gravitational effects on ordinary matter [69]. The mystery of dark matter today is similar to the problem of observed anomalies in the motion of Mercury, whose final solution had to wait for the advent of Einstein's theory of general relativity. In large astrophysical systems spanning from galactic to cosmological scales, we see certain anomalies that can only be explained either by assuming the existence of a large amount of unseen dark matter or by assuming a deviation from the known laws of gravitation and general relativity. Fritz Zwicky conducted a detailed study of the Coma Cluster in the early 1930s. He estimated its total mass on the basis of the number of visible galaxies and their brightness, as well as the radial velocities of the galaxies determined from the Doppler shift of emitted light. Zwicky found that the individual galaxies within the cluster were moving too fast for the cluster to remain stable. To explain this, he proposed the existence of an invisible mass, which he termed *dark matter*, exerting gravitational attraction without emitting light. Such dark matter was estimated to be at least 500 times more abundant than visible matter. Subsequent discoveries in X-ray astronomy revealed that much of this missing mass was in the form of hot gas, but even considering the gas, there was still a significant missing mass contribution in the total mass compared to the visible matter. The strongest evidence supporting the existence of dark matter arises from analyzing the rotational velocities of stars and gas clouds within the galactic halo as a function of the distance from the center of the galaxy. Spiral galaxies, such as our own Milky Way, contain $\sim 10^{11}$ stars arranged in the form of a central nucleus, known as a bulge, and a flattened rotating disk. The rotational speed of a star with mass m around the galaxy's center is determined by the requirement of stable orbits, where gravitational force equals centrifugal force:

$$\frac{G_N m M_r}{r^2} = \frac{m v^2}{r} \tag{1.1}$$

from which:

$$v(r) = \sqrt{\frac{G_N M_r}{r}} \tag{1.2}$$

M_r is the total mass of stars and interstellar medium within the distance r from the center of the galaxy. Most stars in a spiral galaxy are located within the central spherical bulge, characterized by a radius denoted r_s. If $\overline{\rho}$ is the average density of stars in the bulge, we have $M_r = \overline{\rho}\ \frac{4}{3}\pi r^3$ for $r < r_s$, it follows that:

$$v(r) = \sqrt{\frac{4}{3}\pi G_N \overline{\rho}} \cdot r \propto r \qquad \text{for} \quad r < r_s \tag{1.3}$$

Considering now the expected law for a star orbiting outside the galactic bulge, we have:

$$v(r) \propto 1/\sqrt{r} \qquad \text{for} \quad r > r_s \tag{1.4}$$

In the outer region, the rotational speed is that of the ionized hydrogen clouds rotating around the center of the galaxy. These clouds emit radiation with a very well-known wavelength equal to 21 cm, spin-flip radiation. Considering the Doppler effect on this signal, the astrophysicist Vera Rubin [60], almost 40 years later Zwicky studies, was able to find the clouds' orbital velocity.
In almost all cases, after a rise near $r = 0$, the velocities remain constant, as shown in the figure below.

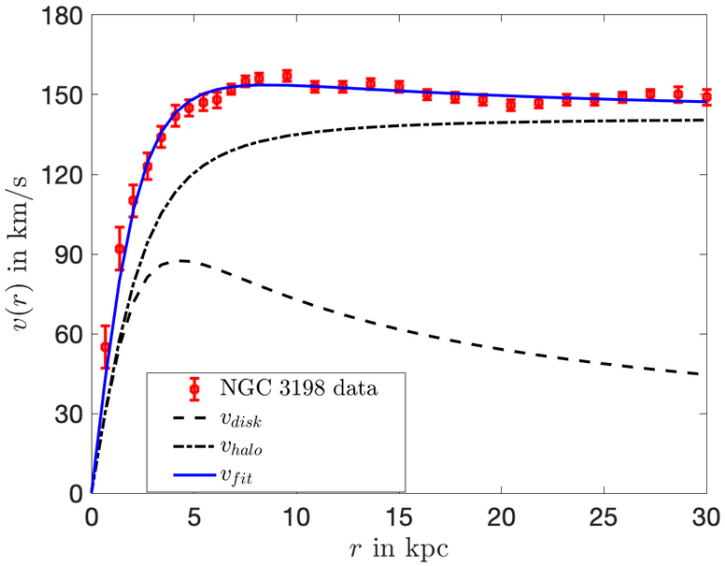

Figure 1.1: Rotation curve for the spiral galaxy NGC3198. From: [71].

From the data, it is clear that, at high values of r, the observed velocities are higher than those predicted by Eq. [1.2]. This suggests a contribution from a halo of dark matter. The evidence for dark matter in the Universe from the dynamics of objects is strong at all observed astrophysical scales, from galaxies to galaxy clusters.

From the astroparticle point of view, a fundamental question arises: What constitutes dark matter? During the past few decades, numerous candidates have been proposed, ranging from *baryonic* to *non-baryonic* entities. Among the latter, candidates can also be categorized as either *hot*, if they were relativistic at the time when galaxies started to form, or *cold*, if their motion was non-relativistic at that time.

WIMPs (Weakly Interacting Massive Particles), hypothetical particles beyond the Standard Model of particle physics, are one of the most investigated cold dark matter candidates. They do not interact with ordinary matter via strong nor electromagnetic interactions, but only via weak interaction. The predicted masses of WIMPs typically fall within the range of 10 GeV/c^2 to a few TeV/c^2. A supersymmetric extension of the standard model justifies one of the most promising WIMP candidates, the so-called *neutralino* [55].

1.1.1 WIMPs interactions

WIMPs can annihilate into several final states, and the dominant annihilation processes are those at the lowest order in perturbation theory with two vertices. These processes are characterized by two-body final states: fermion-antifermion pairs $f\bar{f}$, W^+W^-, Z^0Z^0, two Higgs bosons, one ordinary gauge boson, and a Higgs boson. Since the expected neutralino mass is on the order of, or greater than, 10 GeV/c^2, the annihilation channel into light fermions will always be accessible. Another important aspect that has to be considered is the helicity constraint. Neutralinos are Majorana fermions that, in the limit of zero relative velocity, have null relative orbital angular momentum; in addition, due to Fermi statistics, they must have spins

oppositely directed, and the total angular momentum is consequently equal to zero. In the final state, the two fermions $f\bar{f}$ will have opposite spins. From this configuration, a helicity factor is introduced in the decay probability into this final state that is proportional to the mass of the fermion m_f. To better understand this, we can consider the case of decay of a spinless particle such as a charged pion. Let us consider the two possible decays: $\pi^+ \to \mu^+\nu_\mu$ and $\pi^+ \to e^+\nu_e$, in the π^+ rest frame the respective momenta of the two final-state particles will be opposite. Now, if the neutrino helicity is -1, its spin has to be antiparallel to the momentum. Due to the conservation of the angular momentum, the muon also has helicity equal to -1, and the same is true considering the other decay channel. Based on this, the first decay should be suppressed compared to the second one because the energy in the final states would be higher ($m_\mu \gg m_e$).
However, experimentally, the decay into positron-neutrino is suppressed by a factor $\sim 10^4$, and this is related to the helicity factor.
We have:

$$\Gamma_{\pi\to\mu} \simeq \text{(helicity factor)(phase space factor)} \simeq \left(1 - \frac{v_\mu}{c}\right) p^2 \frac{dp}{dE_0} \tag{1.5}$$

where v_μ is the muon velocity, p the muon momentum and the total energy is $E_0 = m_\pi = p + \sqrt{p^2 + m_\mu^2}$ with ($c = 1$). After some algebraic steps:

$$\Gamma_{\pi\to\mu} \simeq \left(1 - \frac{v_\mu}{c}\right) p^2 \frac{dp}{dE_0} = \frac{m_\mu^2}{4}\left(1 - \frac{m_\mu^2}{m_\pi^2}\right)^2 \tag{1.6}$$

Comparing this expression to the one obtained for the other decay channel, it is possible to compute the ratio between them:

$$R = \frac{\Gamma_{\pi\to e}}{\Gamma_{\pi\to\mu}} = \frac{m_e^2\left(1 - \frac{m_e^2}{m_\pi}\right)^2}{m_\mu^2\left(1 - \frac{m_\mu^2}{m_\pi^2}\right)^2} \simeq \frac{m_e^2}{m_\mu^2}\frac{1}{\left(1 - \frac{m_\mu^2}{m_\pi^2}\right)} \simeq 1.27 \cdot 10^{-4} \tag{1.7}$$

Going back to the annihilation of two WIMPs, if we compare the branching ratios of the final state into a pair of $b\bar{b}$ and that into a pair of lighter quarks, we will find that the latter will be suppressed compared to the former. Therefore, neutralinos predominantly decay into the accessible fermions with the highest mass. Annihilation into light quarks (such as u, d, s, and c) and leptons (e and μ) is negligible compared to annihilation into heavy quarks (such as b and t) and the τ lepton. Direct decay into massless particles is forbidden, making decay into neutrinos virtually negligible. If the neutralino is heavy enough to annihilate into a top quark ($m_\chi > m_t = 173$ GeV/c^2), then in most commonly considered models, annihilation occurs almost exclusively into $t\bar{t}$.

1.1.2 Dark Matter searches

The study of dark matter can be approached in different ways, as schematically shown in the figure below. Direct detection of dark matter aims to observe the

interaction between dark matter particles and ordinary matter using two main techniques. The first involves the usage of large tanks filled with hundreds of liters of a noble element in the liquid state (such as Xenon or Argon), where a collision between a dark matter particle and one of the atomic nuclei of the liquid produces a flash of light. In the second technique, these collisions are looked for using absorptive crystals (for example, germanium), where the interaction results in the release of energy, which manifests itself as an increase in temperature. In both cases, the effects to be measured are microscopic and extremely rare. For this reason, experiments of this kind must be heavily shielded from any source of disturbance, primarily cosmic rays, which, by passing through the detectors, can generate fake signals. Therefore, underground laboratories were built to obtain a high level of shielding. Another possibility consists, at high-energy colliders such as the LHC, in the creation of dark matter particles by colliding known particles, in the same way that the Higgs boson is produced in proton-proton collisions. Since dark matter does not interact significantly with ordinary matter, the underlying signature is a large transverse-momentum imbalance in proton-proton collisions.

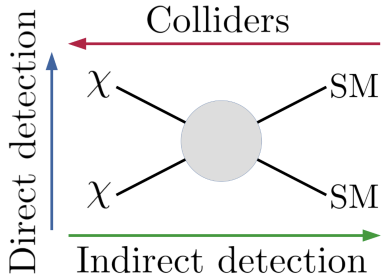

Figure 1.2: Different approaches to the hunt for Dark Matter. In direct detection, dark matter interacts with ordinary matter, such as nucleons. In indirect detection, dark matter self-annihilates or decays into Standard Model particles in outer space. In dark matter searches at the collider, dark matter candidates are produced in the laboratory. From: [48].

Indirect detection of dark matter exploits, instead, the possibility that dark matter particles annihilate, similarly to ordinary matter, generating particles such as gamma rays, charged particles (electron, positron, etc.), and neutrinos. This adds to cosmic radiation of astrophysical origin, but is subdominant.

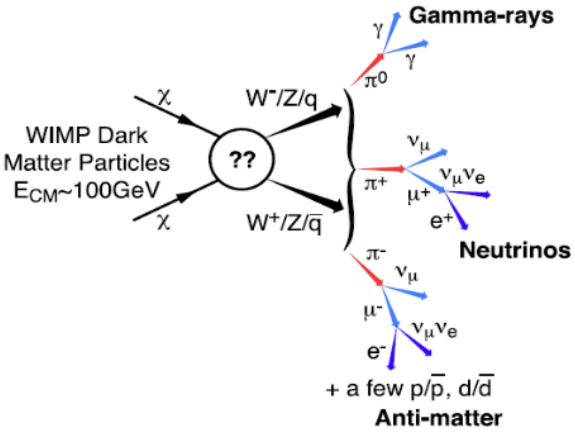

Figure 1.3: Possible annihilation channels for dark matter WIMPs into standard model particles and gamma-ray photons. From: [41].

In any case, the search for stable antiparticles in cosmic radiation is a promising method for searching for a possible dark matter signal.

Antimatter, indeed, is not as abundant as primary radiation, and recent results, found by experiments such as HEAT [32], PAMELA [53], and AMS-02 [68] and reported in Fig. 1.4, have shown an excess of positrons in the cosmic ray spectrum [69]. Most dark matter annihilation or decay models can naturally reproduce the observed rise of the positron fraction (green curve in Fig. 1.4), even if this requires cross sections much larger than predicted. Other alternative explanations exist; as illustrated in Fig. 1.4 below, the presence of a nearby pulsar (red curve) or adjusting current models of cosmic-ray propagation (blue curve) could reproduce both the positron excess and the electron spectrum.

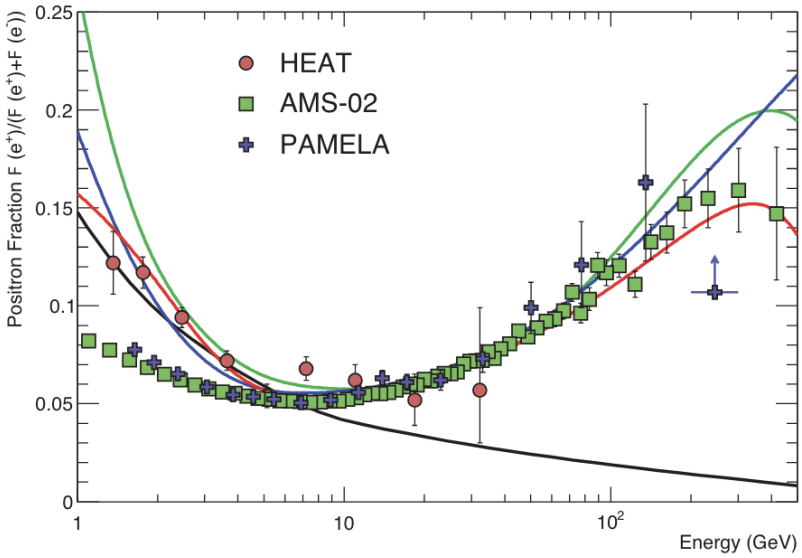

Figure 1.4: The positron fraction in cosmic rays measured by HEAT, PAMELA, and AMS-02. The solid black line is a model of pure secondary production, and the three colored thin lines show three representative attempts to model the positron excess with different phenomena: green is for dark matter decay, blue is for propagation physics, red is for production in pulsars. The ratio below 10 GeV depends on the polarity of the solar magnetic field. From: [58].

It has to be noted that antimatter is of crucial importance not only for its implications for dark matter searches but also because matter seems to surround us with a clear imbalance, which is one of the major unknowns in cosmology and particle physics.

1.2 Cosmic antinuclei and Dark Matter

Research on dark matter using positrons or gamma rays relies on a slight excess above other significant astrophysical sources that constitute a large background. This implies considerable challenges in identifying a potential signal. The case of antiprotons, observed by experiments like BESS [54], PAMELA [22], and AMS-02 [24], is also extremely challenging because it is consistent with many theoretical

models predicting sources other than dark matter, but it sets limits on astrophysical production and propagation scenarios. In this paragraph, however, we aim to explore another aspect related to dark matter studies: *cosmic antinuclei*.

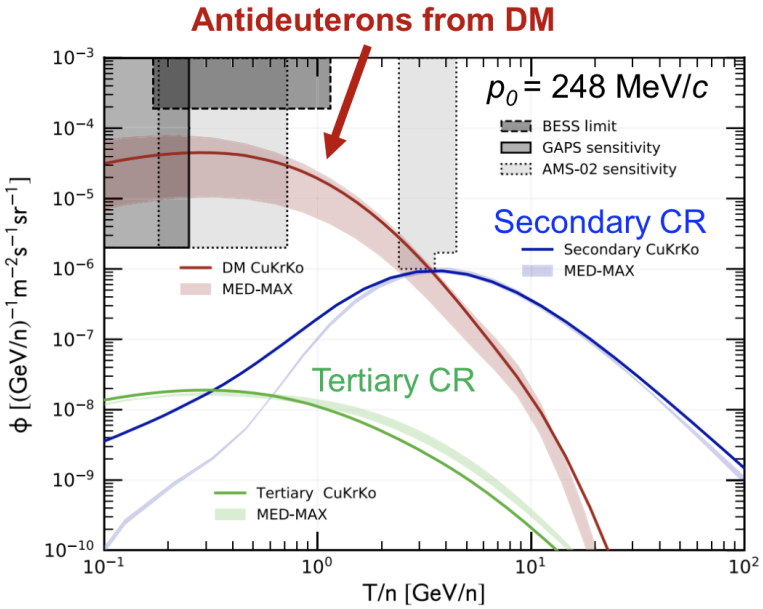

Figure 1.5: Comparison between the expected flux produced by dark matter interactions and the expected flux due to cosmic rays interacting with interstellar matter as a function of kinetic energy per nucleon. Notice that below 1 GeV/n, the red line dominates the blue one. Modified from: [47].

Antinuclei represent an extremely promising evidence for dark matter because, unlike positrons or antiprotons, they have a very low background of astrophysical processes at low energies. This is because there are many astrophysical processes capable of producing antimatter, which makes the production from dark matter less evident, while antinuclei require specific threshold energies and are very rarely produced by cosmic ray collisions with interstellar medium particles. As these processes occur under very particular conditions, for antinuclei, the ratio between primary and secondary cosmic ray flux is higher compared to the case of matter particles, as shown in Fig. [1.5][47]. Therefore, their potential observation would constitute an unequivocal signal of new physics.

1.2.1 The BESS Experiment

From the first BESS [78] (Balloon-borne Experiment with Superconducting Spectrometer) balloon flight in 1993, the BESS Collaboration has completed a total of 11 balloon missions, including two long-duration Antarctic flights, with the final flight occurring in 2008. The original BESS-Polar experiment flew over Antarctica in late 2004, followed by the BESS-Polar II mission, which collected data for 24.5 days of Antarctic flight from December 2007 to January 2008. In a coaxial cylindrical geometry, providing geometric acceptance of 0.23 m^{2}sr, several components were arranged: a solenoidal magnet (0.8 T), filled by inner drift chambers (IDC) and a jet-type drift tracking chamber (JET); an aerogel Cherenkov counter and a time-of-flight system. Other details are shown in Fig. [1.6].

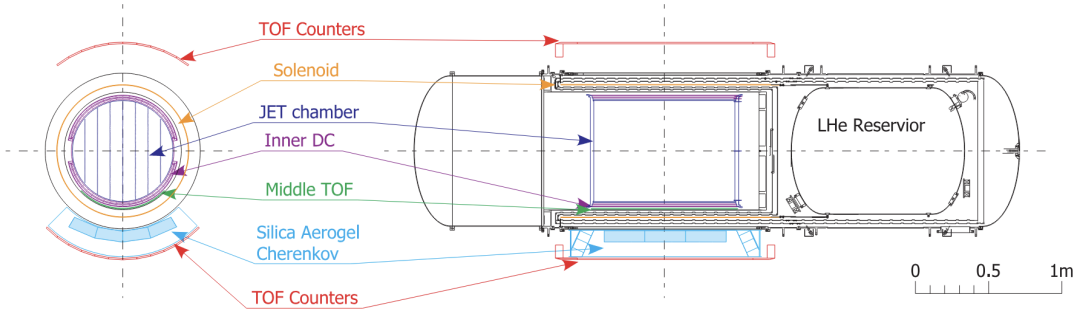

Figure 1.6: The BESS-Polar II experiment. From: [72].

With BESS-Polar II [10], a precise measurement of the low-energy antiproton spectrum below 1 GeV was performed. The antihelium search has established a new limit in the ratio of possible antihelium to measured helium of 6.9×10^{-8} at 95% confidence, the lowest limit to date [62]. With respect to antideuteron search, the BESS collaboration did not report any event, as throughout its missions, they were able to provide an upper limit on antideuteron flux: $\Phi_{\overline{d}} < 5.5 \times 10^{-5} \mathrm{m}^{-2}\mathrm{sr}^{-1}(\mathrm{GeV/n})^{-1}$.

1.2.2 The AMS-02 experiment

Since May 2011, AMS-02, installed on the International Space Station [23, 25], has been operating continuously to measure charged cosmic ray spectra with energies up to the TeV region and with high energy photon detection capability up to a few hundred GeV. AMS-02 also aims to carry out measurements of the nuclear component of the cosmic ray spectrum and to search for indirect signatures of dark matter.

As shown in Fig. [1.7], the AMS-02 experiment is a solenoidal magnetic spectrometer composed of several detectors. The Transition Radiation Detector is used to suppress low-mass particles such as electrons, pions, and kaons and provides a measurement of the relativistic factor γ. The ToF is capable of measuring the particle transit time and, as a result, the velocity of the particle up to $\beta \approx 0.8$ through the detector and provides the trigger for the other sub-detectors. The particle momentum is then extracted using the magnetic field 0.15 T. In the high-velocity region, there is a proximity-focusing Ring Imaging Cherenkov (RICH) detector composed of a dual radiator with silica aerogel and sodium chloride.

Using AMS-02, the most precise antiproton spectrum was obtained in the range $1 - 450$ GV [65]. In 2018, the Collaboration has also announced a few candidate events with mass and charge consistent with antihelium, six $^3\overline{\mathrm{He}}$ and two $^4\overline{\mathrm{He}}$ [70], which, however, have not been confirmed to date.

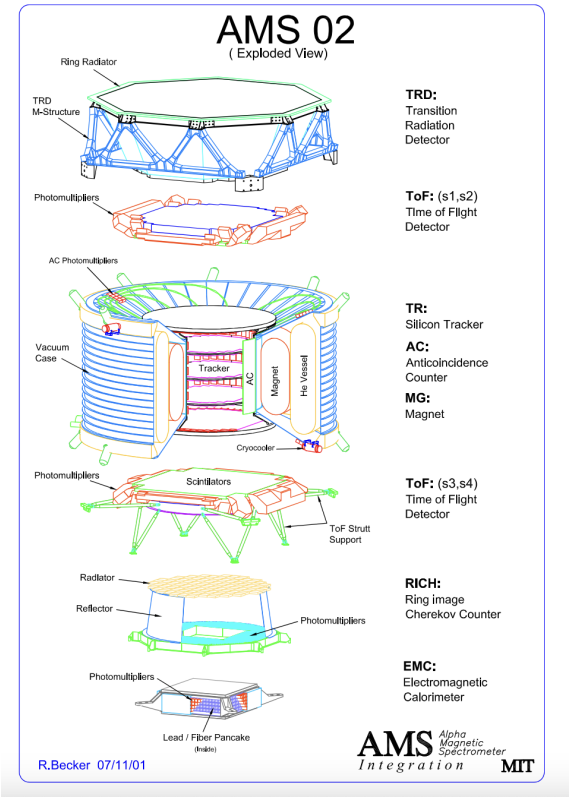

Figure 1.7: The AMS-02 experiment. From: [31].

1.2.3 The GAPS experiment

The GAPS (General AntiParticle Spectrometer) experiment [30], installed on an air balloon, aims to measure the fluxes of antiprotons, antideuterons, and antihelium [61] during long-duration flights (approximately 35 days each) above Antarctica.

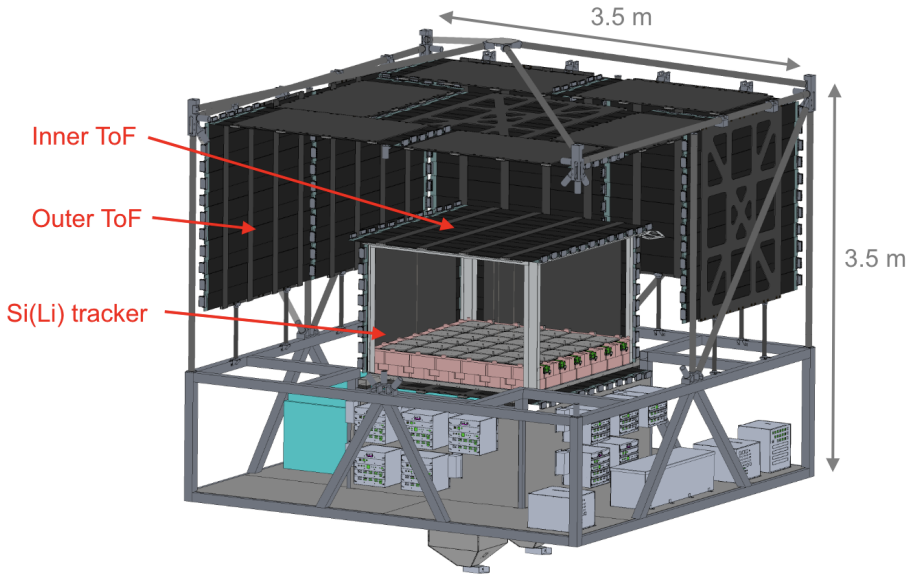

Figure 1.8: GAPS: 10 layers of Si(Li) detectors surrounded by the inner and outer TOF plastic scintillators. From: [30, 72].

The GAPS detection method captures antiparticles within a target material, leading to the formation of exotic atoms. A time-of-flight (TOF) system measures the velocity, energy, and direction of the incoming antiparticles. Antiparticles decelerate because of energy loss and come to a stop within the target material, resulting in the creation of exotic atoms in excited states. These exotic atoms then de-excite, emitting Auger electrons and atomic X-rays. Using the known atomic number of the target, the Bohr formula for atomic X-ray energy allows for a unique determination of the captured particle mass. Ultimately, the antiparticle is captured by a nucleus, which undergoes annihilation and emits annihilation products such as pions and protons. The mean number of these products is proportional to the number of antinucleons, providing a discriminant to differentiate incoming antideuterons from other particles like antiprotons. Antiprotons represent a significant background in GAPS antideuteron measurements, as they can also form exotic atoms and emit atomic X-rays and annihilation products. However, antideuterons are distinguishable from antiprotons through atomic X-rays and annihilation products. This is possible because antiproton and antideuteron events produce different characteristic X-rays emission lines enabling efficient separation. Furthermore, the stopping range of antideuterons, approximately twice that of antiprotons with the same β, allows excellent discrimination.

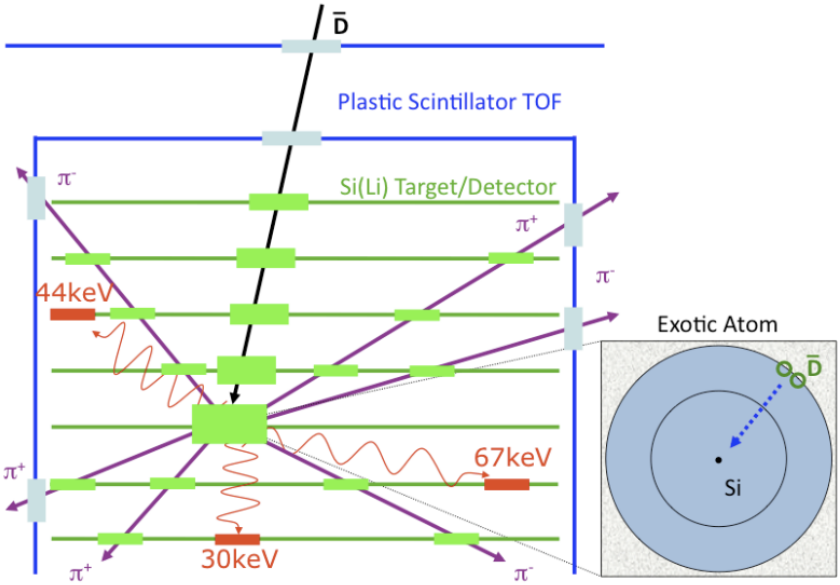

Figure 1.9: GAPS detection method: an antiparticle slows down and stops in the Si(Li) target, forming an exotic atom. The atomic X-rays will be emitted as they de-excite, followed by the pion (and proton) emission during nuclear annihilation. From: [30].

GAPS offers a unique approach to investigating dark matter by specifically examining low-energy antideuterons using distinct detection techniques. By simultaneously detecting atomic X-rays and charged particles resulting from the decay of exotic atoms, along with precise timing and depth sensing of incoming particles, GAPS provides exceptional capabilities for identifying particles, enabling the selection of antideuterons from among other cosmic-ray particles.

1.3 Antihelium flux through $\overline{\Lambda}_b$ decay

The possible observation of antihelium in cosmic rays by AMS-02 (or by any of the future experiments) has profound implications for astrophysics and particle physics. The standard astrophysical sources are expected to produce a negligible amount of antihelium, making any significant detection a potential signal for new physics, particularly DM annihilation. A recent work by Winkler and Linden [74] focused on the possibility that antihelium nuclei could result from the decay of $\overline{\Lambda}_b$ baryons, a previously neglected process. Quarks and gluons are typically produced in dark matter annihilation, and after the hadronization process, protons and neutrons can be produced, as well as the corresponding antiparticles. In rare cases, these antinucleons can bind to form light antinuclei such as antideuteron or antihelium. Models commonly use a "coalescence condition" in which antinucleons with relative momenta below a certain coalescence momentum threshold (p_c) can combine to form antinuclei. In these models, the value of p_c is adjusted based on experimental collider data (from e^+e^- or pp collisions). Since antideuteron and antihelium production rates are low, most studies use an "event-averaged" approach. This method first calculates antiproton and antineutron fluxes and then matches particles between events to estimate antinuclei yields, assuming no correlation between individual antiparticle momenta. However, this assumption is violated by displaced-vertex decays. Some studies [45] have explored event-by-event coalescence, but have focused only on prompt antinucleus production, excluding those from long-lived resonances to avoid cross-mixing between particles with similar momenta but different phase spaces. Consequently, the decay of intermediate particles into multi-nucleon final states has been neglected. Thus, using an event-by-event approach, the idea is to explore the production of antinuclei by including contributions from multiple antiparticle states produced at single displaced vertices. Using two state-of-the-art event generators: `PYTHIA` and `Herwig`, the antihelium spectrum was extracted in [74]. The transition rate $f(b \to \overline{\Lambda}_b) = 0.1^{+0.04}_{-0.03}$ measured at LEP is underestimated by a factor ~ 3 using the first one while the latter is able to reproduce it. To solve this problem, a tuned version of `PYTHIA` was used, in which diquark formation in hadronization (probQQtoQ) was increased. Following an approach to coalescence common in literature for similar studies, the first condition to form antihelium nuclei requires that antinucleons lie within a sphere in momentum space of radius $2^{2/6}p_c/2$. The other condition is that antinucleons have to originate either from the initial vertex or from the same parent particle vertex. The p_c values are determined separately for the two event generators via a fit to ALEPH antideuteron data [63] and ALICE antihelium data [11]. Two different scenarios were considered: the first one considers a dark matter particle with $m_\chi = 67$ GeV that annihilates into bottom quarks, and the second one involves a dark matter particle with $m_\chi = 80$ GeV that annihilates through light mediators (ϕ) with masses of 14 GeV, which subsequently decay to $b\bar{b}$ final states. To extract the local antihelium flux and spectrum, a standard two-zone diffusion model is used based on AMS-02 B/C and antiproton data. The propagation of low-energy cosmic rays is adjusted for heliospheric effects using an improved force-field description that includes charge-sign effects. Tritons, which decay into antihelium before reaching Earth, are included additively in the antihelium flux.

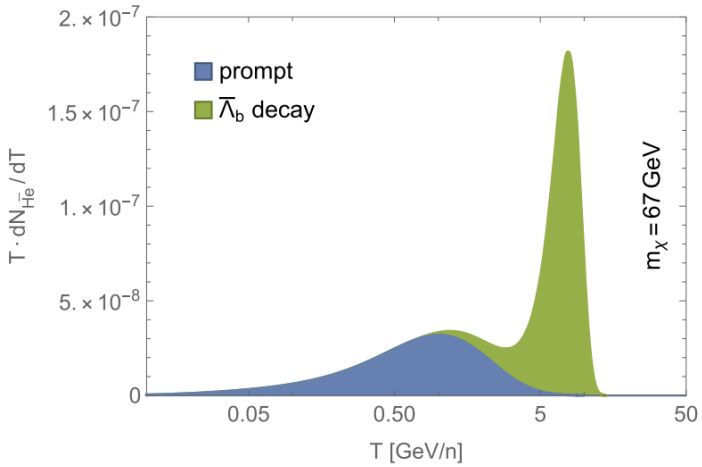

Figure 1.10: The antihelium injection spectrum from dark matter annihilation is generated using the PYTHIA event generator. The contributions of prompt events and those induced by $\overline{\Lambda}_b$ decays are presented separately. The antihelium flux resulting from $\overline{\Lambda}_b$ decays is nearly twice as large as that from prompt events and dominates overwhelmingly the production of high-energy antihelium. From: [74].

In Fig. [1.10], the antihelium injection spectrum from 67 GeV dark matter annihilation, generated using PYTHIA, reveals that approximately 60% of the antihelium flux is produced by decays displaced $\overline{\Lambda}_b$. Additionally, the energy boost from $\overline{\Lambda}_b$ decays is effectively transferred to antihelium nuclei, which dominate the high-energy range where AMS-02 events are detected.

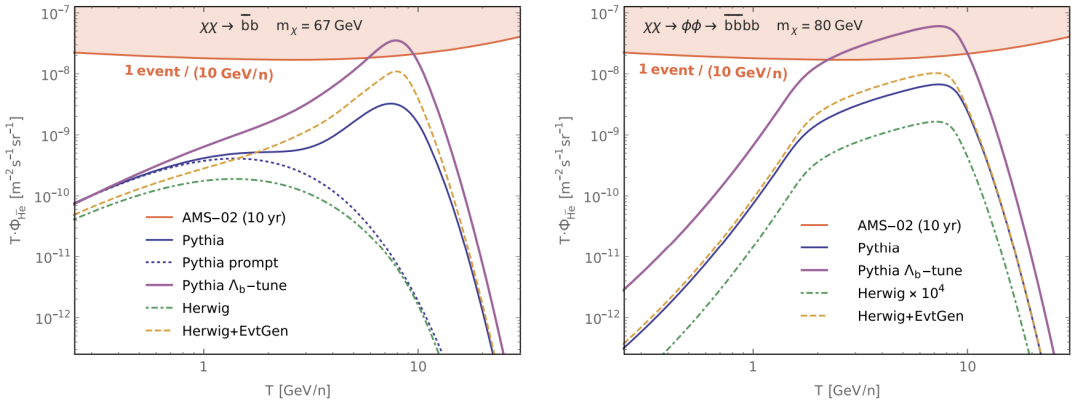

Figure 1.11: The antihelium flux from dark matter annihilation is shown with the AMS-02 10-year sensitivity (in orange). (Left) These results indicate that $\overline{\Lambda}_b$ decays substantially increase the number of detectable antihelium events. (Right) Similar results, but for dark matter annihilation via 14 GeV light mediators. In this case, PYTHIA predicts no prompt events, with all antihelium production occurring through $\overline{\Lambda}_b$ decays. From: [74].

In Fig. [1.11], the integrated and differential antihelium flux at Earth is presented. Considering the $\overline{\Lambda}_b$ decay channel in the tuned version of PYTHIA, the total antihelium flux increases by a factor of about three while the number of detectable antihelium events rises by more than a factor of ten, compared to the default tune [35]. The results obtained with two generators are not the same because even if with Herwig the $\overline{\Lambda}_b$ flux is four times higher than the default PYTHIA implementation, the resulting branching ratios are the following: $\mathrm{BR}(\overline{\Lambda}_b \to \overline{\mathrm{He}}^3) \simeq 3 \times 10^{-6}$ in PYTHIA,

and BR$< 10^{-9}$ in `Herwig`. The key difference between `PYTHIA` and `Herwig` lies in their underlying hadronization models: `PYTHIA` employs the Lund String model [29], while `Herwig` uses a cluster model [73]. The second setup with dark matter mass at 80 GeV and mediator mass at 14 GeV shows that the antihelium flux is enhanced by about three times, and the $\overline{\Lambda}_b$ flux is increased, reducing prompt antihelium production.

In conclusion, the possibility that dark matter annihilations could produce a detectable flux of antihelium was considered, challenging the previous assumption that dark matter typically yields a negligible antinuclei flux. The model used by Winkler and Linden accounts for contributions from displaced-vertex decays of $\overline{\Lambda}_b$ baryons, which were not considered in earlier studies, and opens for a new opportunity to detect a high-energy antihelium signal. Even if the results obtained with the two event generators are different, this study lays the foundation for exploring rare decays of $\overline{\Lambda}_b$ in colliders that could lead to the formation of antihelium.

Chapter 2

(Anti)nuclei in high energy processes

The mechanisms of antinuclei formation in high-energy interactions are still being studied, but, in general, the models that describe this process can be grouped into Statistical Hadronisation Models (SHM) and Coalescence Models. In SHM [33], hadrons are formed from the decay of massive, colorless objects called clusters or fireballs. These clusters emerge in the final stages of a collision and their decay into hadrons is treated statistically. In statistical hadronization models, also called *thermal* models, the key thermodynamic variables include temperature, which determines the average kinetic energy of particles and influences the probability of forming heavier states such as nuclei, depending on their mass. The chemical potential regulates the balance between particle production and annihilation, affecting baryon and meson abundances. The entropy density impacts the expansion and disorder of the system. All possible multi-hadronic states within a cluster, consistent with conservation laws, are equally likely. The SHM assumes that nuclei are formed at the so-called *chemical freeze-out*, which means that the abundances of particles are fixed under equilibrium conditions. The SHM represents a macroscopic model because the predictions about the hadron yields are based on equilibrium conditions without accounting for the microscopic production mechanism. Furthermore, the model does not provide a detailed description of the internal structure of bound objects or the way in which they are formed. On the other hand, the microscopic details of cluster formation, starting from the coalescence model itself, do not require a chemical equilibrium and focus on the conditions of vicinity in phase space (or overlap of the wave functions) between the particles produced in a collision. The coalescence models can provide detailed information on the formation of individual nuclei based on their position and momentum, whereas the SHM can only predict the final abundances of nuclei without considering the microscopic process that generated them. Coalescence was first introduced by Butler and Pearson [37] in 1963 to explain how free protons and neutrons, produced in proton-nucleus collisions at the CERN SPS, can combine to form light nuclei, such as deuterons or antideuterons. In this approach, nucleons that are close in both space and momentum can merge to form a nucleus when the system produced in high-energy hadronic or nuclear interactions decouples. In this model, the main parameter is represented by the *coalescence momentum* p_c that governs the probability of forming a bound state. Given the goal of this dissertation, attention will be paid to coalescence models, as

they are used in the study of antideuteron formation.

2.1 Coalescence model

A crucial element of the analysis performed in this work is the coalescence model [37, 46] that allows us to describe antideuteron formation in high energy interactions, such as pp or heavy-ion collisions. The process states that two (anti)nucleons can combine to form an (anti)nucleus if they are close enough in the phase space at the point in the system's evolution when all collisions among hadrons in the final state have ceased, a stage known as the *kinetic freeze-out*. Identifying $\vec{p_1}$ and $\vec{p_2}$ as the momenta of the two (anti)nucleons involved, the simplest coalescence condition translates into

$$|\vec{p_1} - \vec{p_2}| < p_c. \tag{2.1}$$

The quantity used to determine whether two or more (anti)nucleons have the possibility to form a nucleus of atomic number A, is the *coalescence probability* B_A, which can be used to extract the momentum distribution of the nuclei starting from the momentum distribution of the nucleons:

$$E_A \frac{d^3N}{dp_A^3} = B_A \left(E_p \frac{d^3N_p}{dp_p^3} \right)^Z \left(E_n \frac{d^3N_n}{dp_n^3} \right)^N \tag{2.2}$$

the momentum distribution of a (anti)nucleus with mass number A, is given by the product of the momentum distributions of the protons and neutrons that constitute the nucleus, multiplied by the probability B_A that the process occurs. E_A and p_A are the nucleus energy and momentum, while E_p, p_p and E_n, p_n are respectively the energy and momentum for the proton and neutron. Considering now an equal distribution in energy for protons and neutrons such that $p_p = p_n = \frac{p_A}{A}$, the Eq. [2.2] becomes:

$$E_A \frac{d^3N}{dp_A^3} = B_A \left(E_{p,n} \frac{d^3N_{p,n}}{dp_{p,n}^3} \right)^A \tag{2.3}$$

corresponding to the formula used to experimentally determine the coalescence parameter, as it excludes the contribution of neutrons, which are typically difficult to detect.

2.2 Coalescence model: quantum mechanical approach

A more accurate treatment of the coalescence model takes into account that coalescence is a quantum mechanical process. In this way, the classical definition of phase space is replaced by a description based on the Wigner formalism. The concept of utilizing the Wigner function of the deuteron to explain their formation was initially presented by Scheibl and Heinz in 1999 [64]. The Wigner function of a system is defined as:

$$W(x,p) = \frac{1}{\pi\hbar} \int_{-\infty}^{\infty} \psi^*(x+y)\psi(x+y)e^{2ipy/\hbar}dy \tag{2.4}$$

where $\psi(x)$ represents the wave function of the system under consideration, which in this case is the one of the deuteron. The Wigner function provides the probability that a deuteron exists with a specific relative momentum and separation between its constituents. The process of deriving the production spectrum of deuterons begins by considering a proton and a neutron in a reference frame where their center of mass is in non-relativistic motion. The yield of deuterons, $\frac{d^3N_d}{dp_d^3}$, can be determined by projecting the deuteron density matrix ρ_d onto the two-nucleon density matrix ρ_{pn}:

$$\frac{d^3N_d}{d^3p_d} = \mathrm{tr}(\rho_d \rho_{pn}) \tag{2.5}$$

Here, ρ_d represents a pure state, denoted as $|\phi_d\rangle\langle\phi_d|$, and ρ_{pn} is expressed as $\rho_{pn} = |\psi_p\psi_n\rangle\langle\psi_n\psi_p|$, where N_p and N_n are the average multiplicities of protons and neutrons per event, respectively. By evaluating the trace in the above expression, one obtains:

$$\frac{d^3N_d}{d^3p_d} = S\int d^3x_1 d^3x_2 d^3x_1' d^3x_2' \phi_d^*(x_1,x_2)\phi_d(x_1',x_2')\langle\psi_n^\dagger(x_2')\psi_p^\dagger(x_1')\psi_p(x_1)\psi_n(x_2)\rangle \tag{2.6}$$

where $S = \frac{3}{8}$ is a factor that accounts for spin and isospin degeneracy. The deuteron wave function can be factorized into a plane wave describing the motion of the center of mass with momentum p_d and an internal wave function φ_d:

$$\phi_d(x_1,x_2) = (2\pi)^{-3/2}\exp\left\{ip_d\cdot\frac{x_1+x_2}{2}\right\}\varphi_d(x_1-x_2) \tag{2.7}$$

The two-nucleon density ρ_{pn} is replaced with the two-body Wigner function W_{np}, resulting in:

$$\begin{aligned}\langle\psi_n^\dagger(x_2')\psi_p^\dagger(x_1')\psi_p(x_1)\psi_n(x_2)\rangle = \int \frac{d^3p_n}{(2\pi)^3}\frac{d^3p_p}{(2\pi)^3}W_{np}\left(p_n,p_p,\frac{x_2+x_2'}{2},\frac{x_1+x_1'}{2}\right)\\ \times e^{ip_n(x_2-x_2')}e^{ip_p(x_1-x_1')}\end{aligned} \tag{2.8}$$

By applying the coordinate transformations $r_p = (x_1 + x_1')/2$, $r_n = (x_1 + x_1')/2$, $r = r_n - r_p$, $\zeta = x_1 - x_1' - x_2 + x_2'$, $\rho = (x_1 - x_1' + x_2 - x_2')$, and $p = p_n + p_p$, $q = (p_n - p_p)/2$, along with Eq. [2.8] and Eq. [2.7] into Eq. [2.6], one derives:

$$\frac{d^3N_d}{dp_d^3} = \frac{S}{(2\pi)^6}\int d^3q\int d^3r_p d^3r_n \mathcal{D}(r,q)W_{np}(p_d/2+q,p_d/2-q,r_n,r_p) \tag{2.9}$$

where $D(r,q)$ is the Wigner function of the deuteron. Assuming a Gaussian wave function for the deuteron:

$$\varphi(r) = (\pi r_d^2)^{-3/4}\exp\left(-\frac{r^2}{2r_d^2}\right) \tag{2.10}$$

where $r_d = 3.2$ fm is the characteristic size parameter of the deuteron wave function, and r is the relative distance between the two nucleons inside the deuteron, the corresponding Wigner function is:

$$D(r,q) = 8e^{-r^2/r_d^2 - q^2r_d^2} \tag{2.11}$$

The function W_{np} can be factorized into a momentum-dependent part, $G_{np}(p_d/2 + q, p_d/2 - q)$ and a spatial-dependent part $H_{np}(r_n, r_p) = h(r_n) \cdot h(r_p)$. This assumption implies a transition from a full quantum mechanical treatment to a semi-classical picture. If the distributions of the protons and neutrons are assumed to be uncorrelated, a Gaussian form for the spatial distributions can be used:

$$h(r) = (2\pi\sigma^2)^{-3/2} \exp\left(-\frac{r^2}{2\sigma^2}\right) \tag{2.12}$$

with these assumptions, the Eq. [2.6] becomes:

$$\frac{d^3N_d}{dp_d^3} = \frac{S\zeta}{(2\pi)^6} \int d^3q \, 8e^{-q^2a^2} G_{np}\left(p_d/2 + q, p_d/2 - q\right) \tag{2.13}$$

where the factor ζ is given by:

$$\zeta = \left(\frac{r_d^2}{r_d^2 + 4\sigma^2}\right)^{3/2} \tag{2.14}$$

that depends on the size of the nucleon emission source, denoted as σ.
Eq. [2.13] illustrates the formation of a deuteron from a proton-neutron pair, which has a relative momentum of $2q$ in their center-of-mass frame. The probability for this process is given by:

$$w = S\zeta 8e^{-q^2r_d^2} \tag{2.15}$$

The coalescence probability is suppressed for large $q^2r_d^2$.

2.3 Coalescence tested with experimental data

Over the first ten years of operations at the CERN Large Hadron Collider (LHC), A Large Ion Collider Experiment (ALICE) has accumulated large data samples from pp, p–Pb, and Pb–Pb collisions, enabling precise measurements of light nuclei and anti-nuclei production across various center-of-mass energies. These measurements have provided essential experimental input and significantly advanced theoretical and phenomenological investigations, particularly in relation to the coalescence model. In pp and p–Pb collisions, experimental results appear to support the coalescence model, whereas in heavy-ion collisions[1], coalescence models that neglect the source size fail to reproduce the experimental data, suggesting a correlation between the coalescence process and the size of the particle-emitting source. In this section, an overview of the main experimental results will be provided, but before analyzing the different collision systems, it is necessary to introduce some fundamental concepts: *rapidity* and *pseudorapidity*, *multiplicity* and *centrality*.

[1]The final state of heavy-ion collisions is characterised by a spatial extension of a few femtometer in radius and multiplicities between $10^2 - 10^3$ charged particles per unit of rapidity at midrapidity. For this reasons, heavy-ion collisions are also referred to as *large systems*. Conversely, pp and p-Pb collisions are characterised by low final-state charge-particle multiplicities and small radii of the order of 1 fm, thus labelled as *small systems*.

Rapidity and Pseudorapidity

The rapidity y of a particle is defined as:

$$y = \frac{1}{2} \ln \left(\frac{E + p_z c}{E - p_z c} \right) \tag{2.16}$$

In a collider this quantity is related to the angle between the beam axis and the emission direction. In fact, for a particle moving in the xy-plane (i.e., perpendicular to the beam axis), $p_z = 0$, and thus $y = \frac{1}{2}\ln(1) = 0$. However, for a particle moving along $\pm z$ (i.e., along the beam axis), $E = \pm p_z c$, and therefore $y \to \pm\infty$. It is useful to define the concept of central rapidity: a particle has central rapidity if $|y| < 0.5$. For Lorentz transformations along z, the rapidity (with a boost in E and p_z) transforms as

$$y' = y + \ln \sqrt{\frac{1-\beta}{1+\beta}} \tag{2.17}$$

where $\beta = v/c$. This expression can be simplified, yielding:

$$y' = y - \tanh^{-1} \beta \tag{2.18}$$

This transformation law, particularly simple, has an important consequence. Suppose that two particles are emitted from a collision, with rapidities y_1 and y_2. An observer in a reference frame S' moving with velocity v along the beam axis will observe the two particles with rapidities y_1' and y_2'. The difference in rapidity in the laboratory frame is $y_1 - y_2$, while in the frame S' it will be:

$$y_1' - y_2' = y_1 - \tanh^{-1}\beta - (y_2 - \tanh^{-1}\beta) = y_1 - y_2 \tag{2.19}$$

so the difference in rapidity between two particles is invariant under arbitrary Lorentz boosts along the z-axis. This is why rapidity is a key quantity in high-energy collisions.
Starting from the definition of rapidity and using the energy-momentum relation, we get:

$$y = \frac{1}{2} \ln \left(\frac{(p^2c^2 + m_0^2c^4)^{1/2} + p_z c}{(p^2c^2 + m_0^2c^4)^{1/2} - p_z c} \right) \tag{2.20}$$

$$= \frac{1}{2} \ln \left(\frac{p^2c^2 \left(1 + \frac{m_0^2c^4}{p^2c^2}\right)^{1/2} + p_z c}{p^2c^2 \left(1 + \frac{m_0^2c^4}{p^2c^2}\right)^{1/2} - p_z c} \right) \tag{2.21}$$

In the case of ultra-relativistic particles, where $pc \gg m_0c^2$, it is possible to use a binomial expansion to approximate the quantities under the square roots in Eq. [2.21]. Denoting by θ the angle between the particle's momentum and the beam axis, we can write $\cos\theta = p_z/p$. By carrying out the calculations, we obtain the following relation:

$$y \simeq -\ln \tan \frac{\theta}{2} \tag{2.22}$$

where the exact equality holds for particles moving at the speed of light. Thus, pseudorapidity η is defined as:

$$\eta = -\ln \tan \frac{\theta}{2} \tag{2.23}$$

For ultra-relativistic particles, we have $y \simeq \eta$.

Multiplicity and Centrality

The charged particle multiplicity N_{ch} is defined as the number of charged particles produced during a collision at a given center-of-mass energy. It is useful to divide events into classes based on the average multiplicity of charged particles per unit of pseudorapidity, $\langle dN_{ch}/d\eta \rangle$.
In heavy-ion collisions at the LHC, colliding nuclei move along the beam direction at ultra-relativistic speeds, meaning at velocities close to c, where the kinetic energy of the colliding systems is much greater than their rest mass. The ions, therefore, undergo significant Lorentz contraction, causing them to appear deformed in the laboratory reference frame. Due to the extended size of the nuclei ($r_{Pb} \approx 5.5$ fm), the geometry of the collision varies for each event. In heavy-ion physics, the impact parameter b is typically defined as the distance between the centers of the two nuclei in the transverse plane to the beam axis. The degree of overlap between the two colliding nuclei, which depends on b, is referred to as centrality; the impact parameter thus determines the size of the system's initial volume, with more central collisions having smaller b i.e larger overlap.
Experimentally, the coalescence parameter as a function of transverse momentum p_T has been found to be approximately constant (it depends on how uncertainties are treated, more precise measurements at the LHC suggest that B_2 varies with p_T [12]) in light particle collisions, as can be seen in the Fig. [2.1] where ep collisions are considered. In contrast, in the Fig. [2.2] showing AA collisions, the coalescence parameter decreases with increasing centrality of the collision, and for each centrality, it increases with p_T.

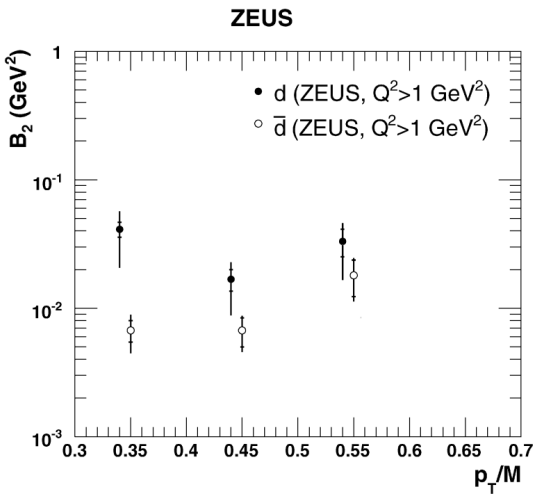

Figure 2.1: The coalescence parameter B_2 for deuterons (d) and antideuterons ($\overline{d}$) is shown as a function of p_T/M, produced in deep-inelastic scattering ep collisions. The inner error bars represent statistical uncertainties, while the outer ones combine statistical and systematic uncertainties in quadrature. To enhance clarity, the data points for particles and antiparticles are slightly offset horizontally from the corresponding p_T/M values. Modified from: [40].

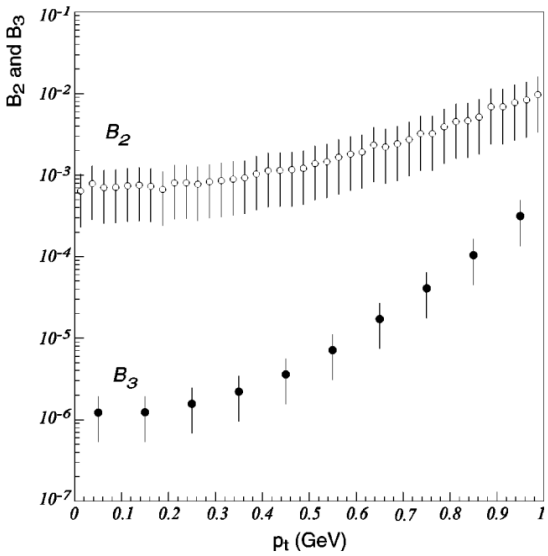

Figure 2.2: The coalescence factors B_2 (open circles, representing deuterons) and B_3 (solid circles, representing ^{3}He) are calculated from the yield ratios d/p^2 and $^3\mathrm{He}/p^3$ as functions of p_T, in the rapidity interval $0.22 < y/y_{\mathrm{beam}} < 0.25$. These results are obtained from Au+Au collisions with beam momentum per nucleon of 11.6 GeV/c. From: [26].

Considering now pp collision the coalescence parameter is shown for three different values of center-of-mass energy as a function of the transverse momentum per nucleon p_T/A in Fig. [2.3] where it can be seen that B_2 is not constant as a function of p_T. In addition, these measurements show that the coalescence parameter for deuterons and antideuterons is compatible and does not exhibit significant dependence on the collision energy within the uncertainties.

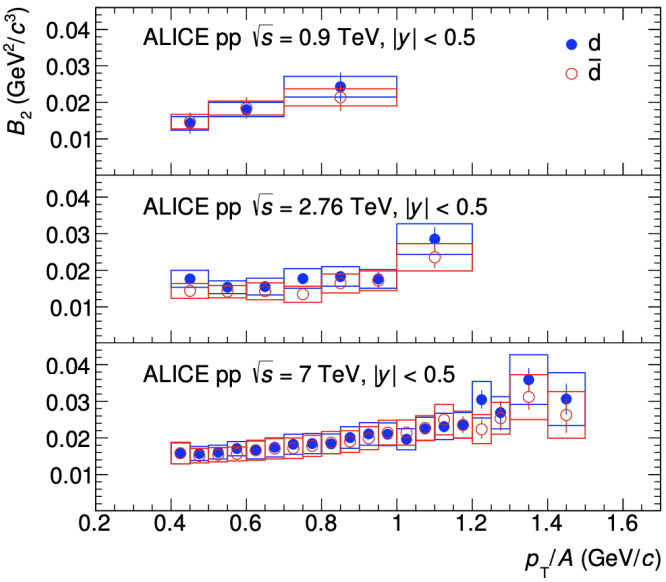

Figure 2.3: The coalescence parameter B_2 of (anti)deuterons (red, blue) was computed as a function of p_T/A in inelastic pp collisions at center-of-mass energies of $\sqrt{s}$ = 0.9, 2.76, and 7 TeV. The statistical uncertainties are represented by error bars, while the systematic uncertainties are shown by boxes. From: [12].

As shown in section 2.1, a simplified picture of the coalescence process neglects

the size of the source, but treating the process as in section 2.2, we can adopt a formalism able to define the phase space dependence. The probability of coalescing corresponds to the overlapping probability between the nucleon pair (initial state) and the nucleus (final bound state) wave functions. Using this description and performing several computations [34], we can extract the following expression for the coalescence probability:

$$B_A = \frac{2J_A+1}{2^A}\frac{1}{\sqrt{A}}\frac{1}{m_T^{A-1}}\left(\frac{2\pi}{R^2+(\frac{r_A}{2})^2}\right)^{\frac{3}{2}(A-1)} \tag{2.24}$$

where J_A is the total angular momentum of the nucleus, m_T is its transverse mass, r_A is its radius and R is the radius of the source.
Another important consideration is that the coalescence parameter is highly dependent on the average charged-particle multiplicity density at central rapidity ($|y| < 0.5$) $dN_{ch}/d\eta$, for a given value of p_T/A, as shown in Fig. [2.4]. The multiplicity density ($dN_{ch}/d\eta$) is proportional to the volume of the system and scales with the cube of the source radius. The B_A parameter shows a strong dependence on the size of the particle-emitting region, also referred to as the source. As the volume of the source increases, the distance between produced nucleons grows, leading to a reduction in the coalescence probability. This effect is less prominent in small collision systems, such as pp or pPb collisions, where the size of the produced nucleus is typically larger than the size of the emitting region.

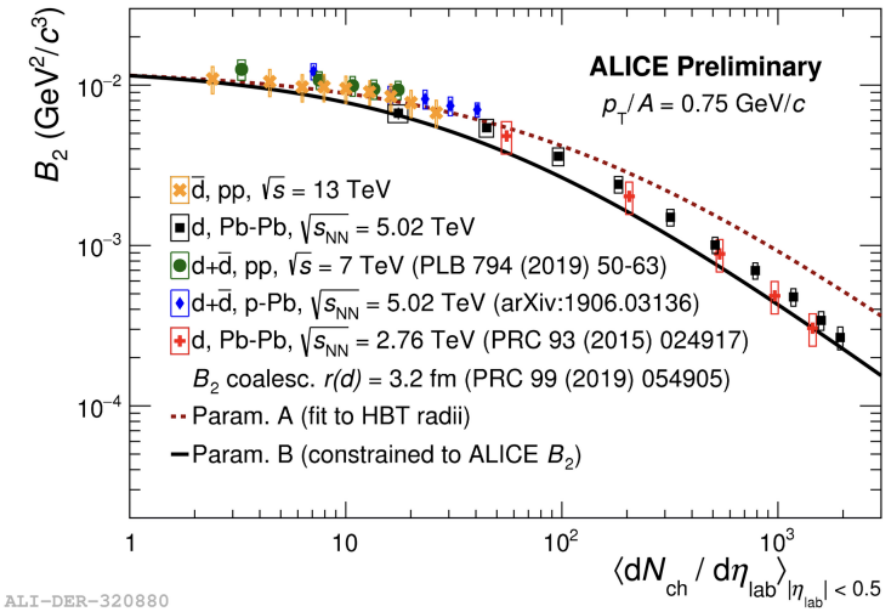

Figure 2.4: The coalescence parameter B_2, as a function of the mean charged-particle multiplicity density $\langle dN_{\rm ch}/d\eta_{\rm lab}\rangle$ for a fixed value of $p_T/A = 0.75$, GeV/c, is compared to the coalescence calculations from [34]. Two distinct parameterizations for the system size as a function of $\langle dN_{\rm ch}/d\eta_{\rm lab}\rangle$ are utilized. From: [43].

In conclusion, the coalescence probability depends on:

- the size of the nucleon-emitting source

- the size of the cluster to be formed (i.e., its wave function)
- the transverse momentum (or transverse mass) of the nucleons

therefore, a state-of-the-art coalescence approach based on Wigner formalism is needed to obtain the best description of the coalescence mechanism.

2.4 Monte Carlo approach to coalescence

The creation of light nuclei happens when clusters of nucleons merge. Historically, in small systems like electron-positron annihilations or proton-proton collisions, this process usually focuses on the momentum difference, ignoring the dimension of the interaction region. On the other hand, for heavy-ion collisions, models mainly consider the size of the interaction area and often neglect or simplify momentum correlations between nucleons. To account for both factors, a per-event coalescence model based on the Wigner function is used. This model accurately describes the size of the source for baryon emissions and the coalescence factor, measured by ALICE in proton-proton collisions. In Section 2.2, starting from Eq. [2.9], we factorized the Wigner function W_{np} into a momentum-dependent component G_{np} and a spatially dependent component H_{np}. Thus, to proceed, it was necessary to specify the Wigner function. One possible approach is to determine the phase-space distribution via simulations. In fact, both perturbative and non-perturbative evolution of strong interactions in MC generators are based on momentum eigenstates and, therefore, only provide information on the momentum correlations of nucleons. In this way, within the Wigner function model, it is possible to combine the two nucleon momentum correlations obtained through QCD-inspired event generators with a simple analytical model for the spatial distribution. Furthermore, Eq. [2.13] becomes a general expression that can, in principle, be used to describe the production of other nucleon-like systems with small binding energies, provided the approximate wave function of the produced system is given. In Section 2.3, experimental results on the coalescence parameter as a function of transverse momentum p_T and multiplicity are presented. Similarly, it is possible to show that the Wigner function model, combined with QCD-inspired event generators, can be used.

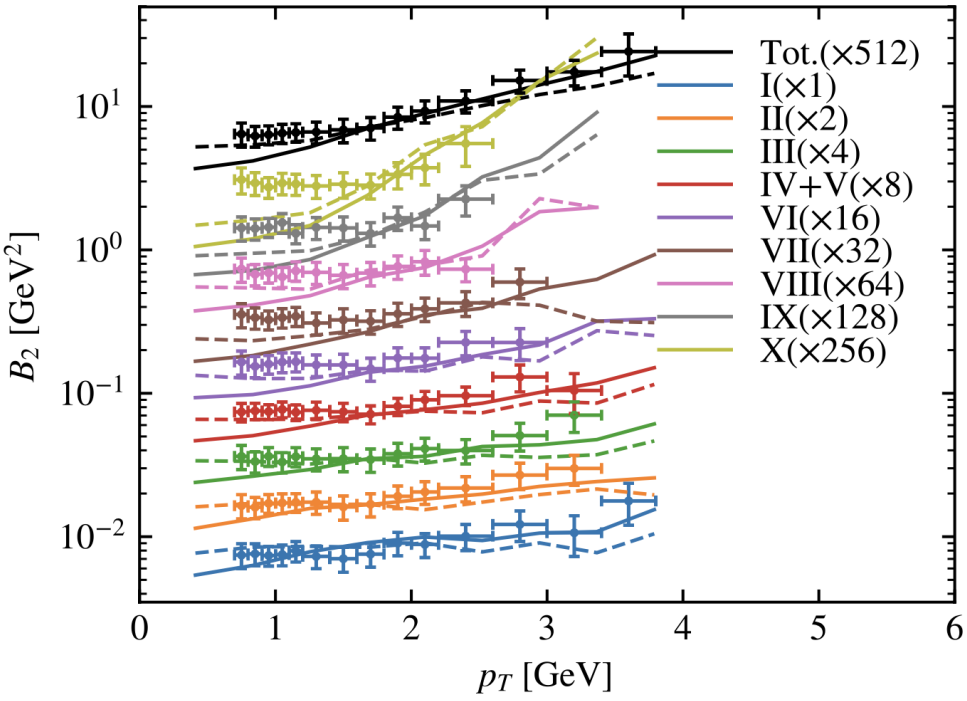

Figure 2.5: The coalescence factor B_2, measured by the ALICE collaboration for various multiplicity classes, is compared to the predictions obtained from the WiFunC model, using the Wigner function based coalescence, used in cascade to PYTHIA 8.2 (solid lines). For reference, the results from the standard coalescence model (dashed lines) are also included. Class I represents the highest multiplicities, with the multiplicity decreasing as the class number increases. From: [45].

Specifically, when looking in Fig. [2.5] of B_2 as a function of p_T for different multiplicities, we can observe that, by comparing standard coalescence models (dashed lines) with a Wigner function-based model such as WiFunC (solid lines) from [45], the dependence of B_2 on multiplicity is stronger in the latter obtaining a better description of the data. Furthermore, although the slope of B_2 increases even for simple models, it increases more significantly in PYTHIA with WiFunC. This suggests that, although two-particle correlations are not the only effect responsible for the growing slope of B_2, they cannot be neglected for pp collisions within the kinematic range considered.

Chapter 3

ALICE and LHCb

In this chapter, the main characteristics of the ALICE and LHCb detectors located at the LHC are presented. While ALICE has worked and continues to work on measurements concerning nuclei and antinuclei, the LHCb experiment has recently joined the research in this field. Furthermore, upgrades of the respective experiments developed for RUN 3 at the LHC are presented.

3.1 The ALICE detector

A Large Ion Collider Experiment (ALICE) shown in Fig. [3.1], part of the Large Hadron Collider (LHC) and located 56 meters underground at interaction point 2 of the LHC, is a dedicated heavy-ion collision experiment. The experiment aims to investigate the properties of the Quark-Gluon Plasma (QGP), a state of matter characterized by a hot and dense environment where quarks and gluons are no longer confined. This plasma is believed to have existed in the early moments after the Big Bang and is recreated in high-energy heavy-ion collisions.
ALICE's research is not limited to heavy-ion collisions like lead-lead (Pb-Pb) but also includes proton-proton (pp) collisions. With its broad physics program and unique goals, ALICE is equipped with sophisticated particle identification systems and advanced tracking capabilities that can operate in high-multiplicity environments and detect particles at low momenta.
The ALICE detector, known as ALICE1 during Run 1 and Run 2, underwent upgrades during Long Shutdown 2 (2019-2021). The updated ALICE detector, known as ALICE2, has been active in Run 3. The upgraded detector is focused on studying the interactions of heavy quarks (charm and bottom) and the thermal radiation emitted from the QGP using dielectron measurements. Additionally, ALICE provides high-precision measurements in jet quenching phenomena, particle production, and correlations between hadrons, as well as collective effects in high-multiplicity pp collisions. The ALICE detector weighs 10,000 tons and measures 26 meters in length, 16 meters in height, and 16 meters in width. It is symmetrically designed around the beam pipes. The z-axis corresponds to the beam axis, and the xy-plane forms the transverse plane in the detector reference frame.
ALICE comprises various subdetectors that provide detailed information on particle interactions. The central barrel houses a solenoidal magnet with a magnetic field of 0.5 T. Surrounding the apparatus is a magnet from the former LEP experiment inherited from the L3 detector.

The main components of ALICE include:

- **Inner Tracking System (ITS)**: Responsible for tracking particle trajectories.
- **Time Projection Chamber (TPC)**: Used for momentum and charge particle tracking.
- **Time of Flight (TOF)**: Identifies particles by measuring their velocity.
- **Transition Radiation Detector (TRD)**: Helps reconstruct charged particles within $|\eta| < 0.9$, allows event triggering, and differentiates electrons from background pions.
- **Electromagnetic Calorimeter (EMCal)**: Detects high-energy photons and electrons, especially from decays of hadrons or neutral mesons.
- **Photon Spectrometer (PHOS)**: Provides precise measurements of photons with high spatial and energy resolution.
- **High Momentum Particle Identification Detector (HMPID)**: Uses Cherenkov radiation to identify hadrons at large transverse momentum.

In the forward region, the Muon Spectrometer detects muons from hadronic decays within the rapidity range $-4 < \eta < -2.45$, utilizing silicon pixel sensors. Additionally, the Zero-Degree Calorimeters (ZDC) determine the centrality of collisions, while the Fast Interaction Trigger (FIT) is used to measure interaction times, luminosity, and multiplicity. The FIT detector consists of two Cherenkov radiators, FT0-A and FT0-C, placed 3.3 meters from the collision point.

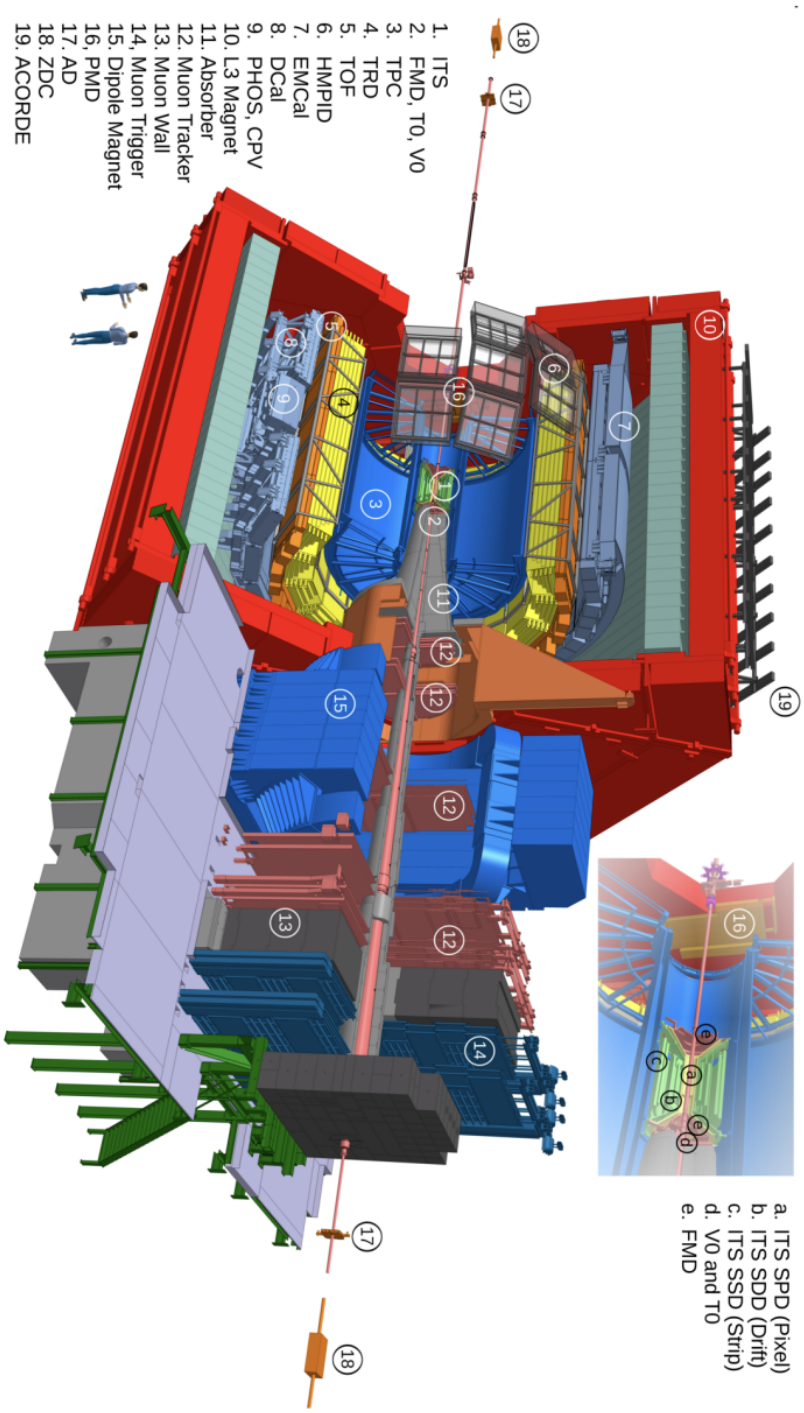

Figure 3.1: Overview of the ALICE detector. From: [43].

3.1.1 ALICE upgrades for Run 3

Inner Tracking System

The Inner Tracking System (ITS), as shown in Fig. [3.2], is the initial detector encountered by particles produced in the collision vertex. It is positioned in the

central barrel and spans a pseudorapidity range of $|\eta| < 1.3$. Being the detector closest to the interaction point, its primary objective is to reconstruct the primary vertex of the collision, track and identify low-momentum particles, and reconstruct secondary vertices resulting from weak decays of primary particles, typically with lifetimes $\tau \sim$ cm/c. The upgraded version, ITS2, is both slimmer and lighter than its predecessor, ITS1. A summary comparison between ITS1 and ITS2 is presented in Table [3.1].

	ITS1	**ITS2**
Technology	Hybrid pixel, strip, drift	MAPS ALPIDE
Readout Rate	1 kHz	50 kHz (Pb-Pb) 400 kHz (p-p)
No. of layers	6	7
Radius of innermost layer	39 mm	22.4 mm
Pointing resolution **($p_T = 500\,\mathrm{MeV}/c$)**	$\sim 240\,\mu$m (z) $\sim 120\,\mu$m (rϕ)	$\sim 50\,\mu$m (z) $\sim 40\,\mu$m (rϕ)
Material budget	1.1% X_0	0.36% X_0 (Inner Barrel) 1.1% X_0 (Outer Barrel)

Table 3.1: Comparison between the main properties of ITS1 and ITS2. From: [59].

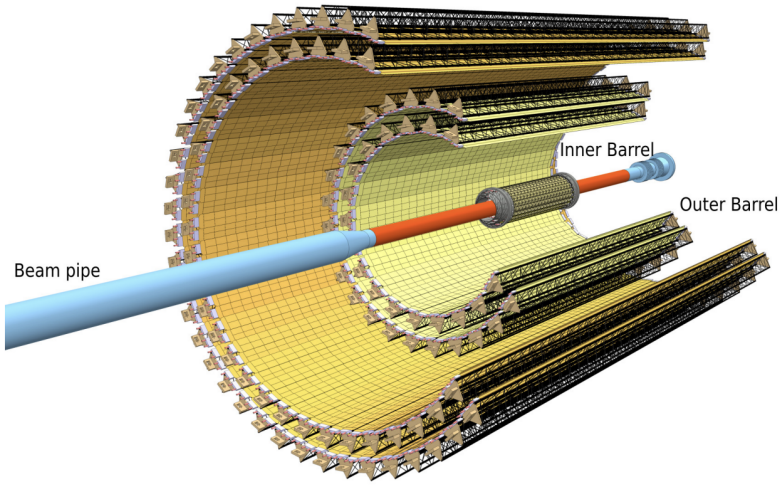

Figure 3.2: Schematic layout of the upgraded ITS. From: [59].

The ITS2 consists of seven concentric layers, which are divided into two components: the Inner Barrel, comprising the three innermost layers, and the Outer Barrel, which is made up of the four outermost layers. All layers are equipped with ALPIDE (Monolithic Active Pixel Sensors) made of silicon (see ref. [20] for further details). The area covered by silicon pixels in ITS2 has also been expanded. Covering an area of approximately 10 m^2, ITS2 represents the largest silicon tracker using MAPS ever built for a high-energy physics experiment. The fast digital pixel sensors enable an increase in the readout rate by approximately 100 times compared to ITS1. This allows the readout rate to exceed 50 kHz in Pb-Pb collisions and reach up to 400 kHz in proton-proton collisions. These increased rates enhance the statistical precision

of measurements and contribute to reduced background levels. ITS2 features nearly 12.5 billion ALPIDE pixels, each measuring 27×29 μm^2. This reduction in pixel size results in improved granularity and segmentation. Furthermore, the material budget and the impact of multiple scattering are reduced to 0.36% X_0 in the inner layers and to 1.10% X_0 in the outer layers, accomplished through the use of pixel sensors instead of strip detectors. A key objective of the ITS upgrade was to improve the resolution of the impact parameter and the collision vertex reconstruction. This was achieved by decreasing the radial distance of the first layer of the Inner Barrel from the beam axis to 22.4 mm (compared to 39 mm in ITS1). Consequently, the resolution of the impact parameter in ITS2 was significantly improved, reaching $5, \mu$m $\times$ $5, \mu$m in $(z \times r\phi)$, as shown in Fig. [3.3].

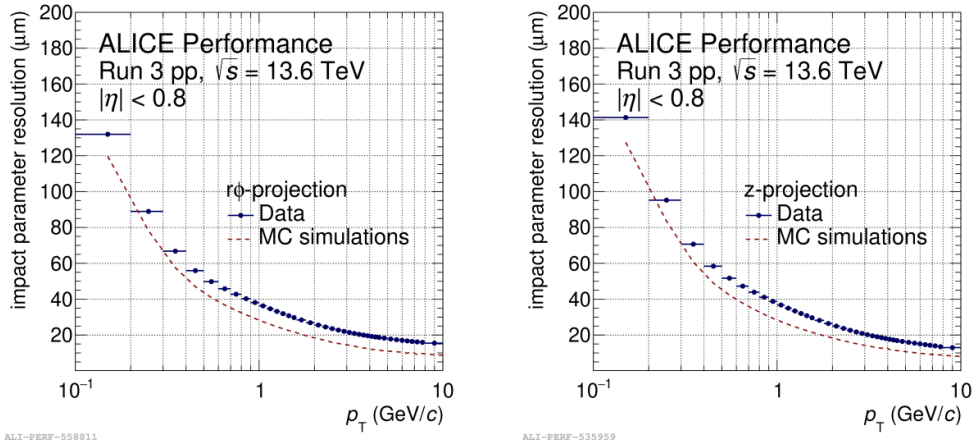

Figure 3.3: The resolution of the impact parameter as a function of transverse momentum is shown for the transverse $r\phi$ plane (left panel) and the longitudinal z plane (right panel), based on measurements from pp collisions at $\sqrt{s} = 13.6$ TeV. The data (in blue) are compared with results from Monte Carlo simulations (in red). From: [59].

A comparison of the impact parameter resolution for ITS1 and ITS2 is illustrated in Fig. [3.4]. The ITS2 upgrade significantly enhances tracking efficiency from 60% to 90%, and it also improves the transverse momentum resolution for low-momentum particles, achieving an excellent tracking capability for particles with a transverse momentum of approximately $p_T \sim 120$ MeV/c.

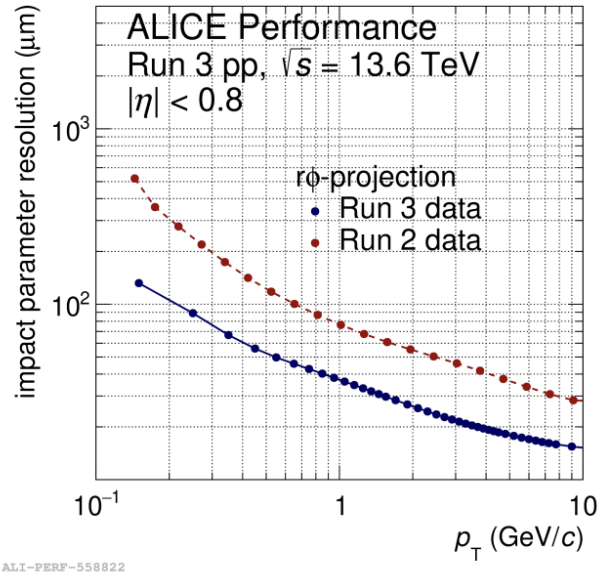

Figure 3.4: The impact parameter resolution in the $r\phi$ plane as a function of p_T is compared between data from pp collisions at $\sqrt{s} = 13.6$ TeV in Run 3 (blue) and data from $\sqrt{s} = 13$ TeV in Run 2 (red). From: [59].

Time Projection Chamber

The Time Projection Chamber (TPC) in the ALICE experiment is a gas detector used for tracking and particle identification. Its primary function is to measure the energy lost by charged particles traversing the detector. This energy loss, combined with momentum and charge information, enables particle identification. Different particles lose energy at different rates depending on their charge and mass. For example, particles with a charge $z = 1$ (such as protons, kaons, pions, electrons, etc.) can be distinguished from particles with $z = 2$ (e.g., helium-3 nuclei). Furthermore, equally charged particles with varying masses (e.g., pions and kaons) can be differentiated based on their energy loss at a given momentum. The TPC is a cylindrical chamber filled with a gas mixture of Ne-CO_2-N_2 (90-10-5) and covers a pseudorapidity region of $|\eta| < 0.9$ and full azimuth. When charged particles pass through, they ionize the gas, creating electrons and positive ions that drift toward the anode. The ionization electrons are collected at the readout chambers after drifting, and the energy loss is recorded. The TPC was upgraded for Run 3 (more details in [42]) to enable continuous and triggerless readout by replacing the Multi-Wire Proportional Chambers (MWPCs) with Gaseous Electron Multipliers (GEMs). The GEM-based readout system significantly increases the readout rate (by nearly 100 times compared to MWPCs) and reduces ion backflow, which could affect the performance of the TPC. This is achieved by stacking four GEM foils, each with specific voltage differences across gaps. As electrons pass through the GEMs, they create avalanches that amplify the signal. The new TPC design minimizes ion backflow to about 1% and achieves an energy loss resolution of 5-10% and a momentum resolution of about 1%.

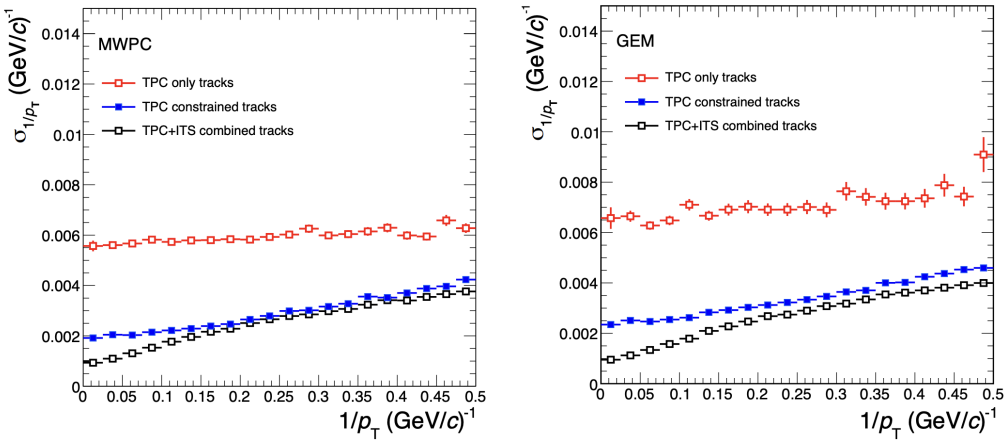

Figure 3.5: The resolution in $1/p_T$ as a function of $1/p_T$ is presented for MWPC (left panel) and GEM readout (right panel). The open red squares represent tracks based only on TPC information, while the closed blue squares indicate TPC track fits that include the vertex point. The open black squares correspond to the results from combined fits to TPC and ITS track points. From: [49].

Time Of Flight

The Time of Flight (TOF) detector in the ALICE experiment is crucial for identifying particles by measuring the time it takes them to travel from the collision point to the TOF detector layer. In particular, the TOF detector, positioned 3.7 m from the beam axis, relies on Multi-gap Resistive Plate Chambers (MRPC) to accomplish this task. For Run 3, significant upgrades were implemented to ensure better particle identification and higher readout performance to accommodate increased collision rates. The TOF detector covers a cylindrical array with an active area of approximately 141 m^2, organized into 18 azimuthal sectors. Each sector contains about 90 MRPCs, giving a total of 1593 strips. To enhance spatial resolution and reduce occupancy, each MRPC strip is segmented into 96 pads. The readout involves 152,928 channels, which enables fine granularity and improved performance in tracking the time of flight of particles. For Run 3, the electronics of the TOF were redesigned for continuous readout, ensuring a seamless capture of data during high-luminosity periods. MRPCs are gaseous detectors made up of two resistive plates held at a high voltage. These plates create a uniform electric field, and the gap between them is filled with gas. In this gap, charged particles ionize the gas molecules as they pass through, generating electron avalanches that multiply due to the electric field. A unique aspect of MRPC technology is the subdivision of the gap into smaller sections using resistive floating plates, which allows for five distinct mini-avalanche events. This design helps improve the time resolution by isolating and amplifying the signal in each gap. For Run 3, the intrinsic time resolution of the MRPC, which was around 50 ps, remained one of its key advantages. The new readout system for Run 3 significantly reduces dead time and can handle a much higher event rate. The Run 3 upgrades achieved a resolution of around 60-80 ps, a significant improvement over previous runs, allowing for more precise particle identification.

The primary function of the TOF detector is to assist in particle identification. By measuring the time difference, Δt, between a particle's emission and detection and using the track length l, the particle's velocity β can be calculated. From this, the

mass m of the particle is inferred using the following relation:

$$m = p\sqrt{\left(\frac{\Delta t}{l}\right)^2 - 1} \tag{3.1}$$

Here, p is the particle's momentum, which is provided by the TPC. This method allows the TOF to distinguish between particles with different masses, such as electrons, pions, kaons, and protons. As shown in Fig. [3.6], the Run 3 enhancements improved the performance for a wide range of momenta. In particular, particles such as electrons, pions, kaons, and protons can be clearly identified within the $|\eta| < 0.9$ pseudorapidity range.

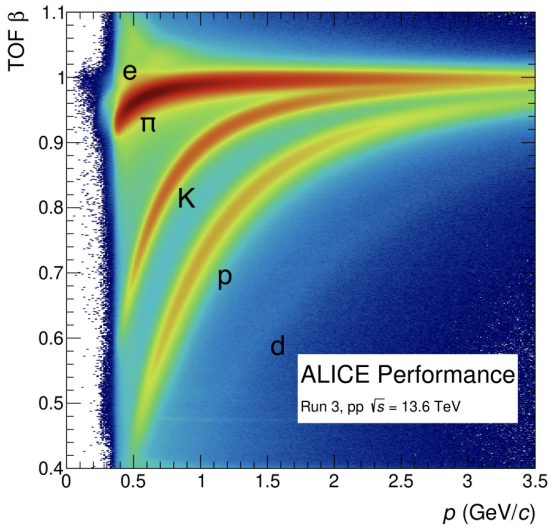

Figure 3.6: TOF Beta versus Momentum performance for pp collisions at $\sqrt{s} = 13.6$ TeV during Run 3, showing clear separation of particle species based on their mass and velocity.

3.2 The LHCb detector

The LHCb (Large Hadron Collider beauty) experiment [2], part of CERN's Large Hadron Collider (LHC), is designed to investigate the subtle differences between matter and antimatter through precision measurements of B-mesons and other heavy flavor particles. LHCb focuses on studying violation and rare decays of CP. The ALICE collaboration has contributed significantly to the understanding of light nuclei and antinuclei production mechanisms through numerous results. However, there remains a gap in data for the intermediate energy range, bridging the GeV energies from fixed-target experiments at the SpS and the TeV energies at the LHC. The LHCb experiment, with its forward spectrometer geometry and the capability to introduce noble gas targets into the LHC beam pipe, is ideally positioned to address this gap. An overview of the LHCb detector is given below.

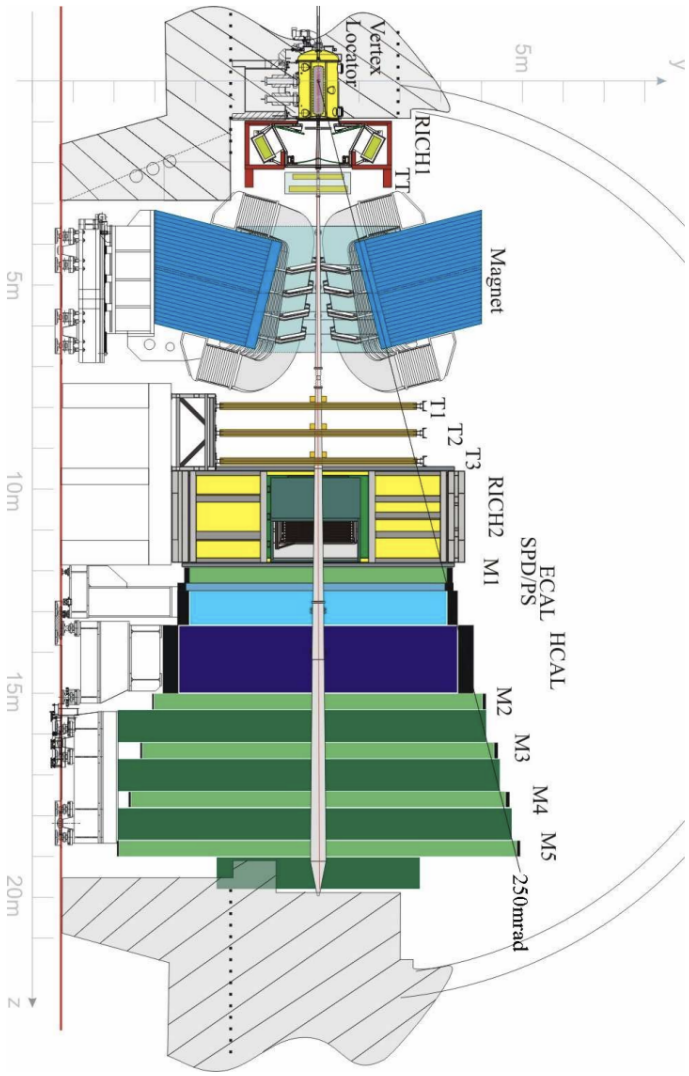

Figure 3.7: Overview of LHCb detector. From: [43].

The LHCb detector is a forward spectrometer with a single-arm design covering the pseudorapidity range $2 < \eta < 5$ and a dipole magnet with a magnetic field of 1.1 T. This is ideal for studying hadrons containing b and c quarks, as these are produced at high pseudorapidity in pp collisions. The detection strategy of the experiment revolves around precise tracking, vertexing, and particle identification, allowing accurate measurements of heavy-flavor hadron decays. The detector is composed of multiple subsystems:

- **Vertex Locator (VELO)**: Essential for precise vertex reconstruction, enabling the accurate identification of primary and secondary vertices associated with b-hadron and c-hadron decays.
- **Tracking System**: Upstream Tracker (UT) and Scintillating Fiber (SciFi) Tracker. These detectors ensure high-precision tracking of charged particles and provide momentum measurements across the detector's pseudorapidity acceptance.

- **RICH Detectors**: Allow us to perform the particle identification (PID). There are two RICH detectors, RICH1 and RICH2. Located upstream of the dipole magnet, RICH1 is optimized to identify low-momentum particles (below 60 GeV/c). RICH2 is located downstream of the magnet and is designed to identify high-momentum particles (above 10 GeV/c). Like RICH1, it utilizes spherical mirrors and photon detectors to capture Cherenkov light, but its configuration is optimized for higher energies.

- **Electromagnetic Calorimeter (ECAL)**: Measure the energy of electrons and photons through electromagnetic showers.

- **Hadronic Calorimeter (HCAL)**: Measure the energy of hadrons. It consists of iron absorber plates and scintillating tiles. The HCAL contributes to particle identification by providing hadronic energy measurements, especially for jets and other high-mass particles.

- **Muon System**: The LHCb muon system is crucial for identifying muons, which are common in many B-meson decays. The system consists of five stations (M1–M5) located at the downstream end of the detector. Each station contains multiple layers of multi-wire proportional chambers (MWPCs), with the innermost region equipped with Gas Electron Multiplier (GEM) detectors for better performance in the highest occupancy areas. The muon system provides fast and reliable muon identification, which is used in both the trigger system and the offline analysis.

3.2.1 LHCb upgrades for Run 3

During Long Shutdown 2 (LS2), the LHCb detector underwent major upgrades to extend its physics potential and cope with the higher luminosity and event rates expected during Run 3 and Run 4 [6]. The luminosity is projected to increase by a factor of five, up to $L \sim 2 \times 10^{33}$ cm^{-2} s^{-1}, creating a more challenging radiation environment and significantly higher detector occupancy. To address these challenges, the detector was redesigned with a focus on improving radiation hardness, increasing granularity, and enabling faster readout speeds. Additionally, a new trigger system was implemented to handle the much larger data volumes.

Tracking System Upgrades

The tracking system saw some of the most significant upgrades to ensure high efficiency at higher event rates. The upgrades included complete replacements of the Vertex Locator (VELO), the TT tracker, and the Outer Tracker (OT) systems, with new technologies designed to improve spatial resolution and cope with the increased luminosity.
The Vertex Locator (VELO), essential for identifying primary and secondary vertices, underwent substantial improvements. The semi-circular strip modules used in Run 2 were replaced by advanced pixel modules. This new L-shaped pixel detector reduces the minimum distance from the beamline from 8.2 mm to 5.1 mm, enhancing the resolution of the impact parameter and vertex reconstruction. The layout of the VELO modules was also optimized for higher efficiency. Without the need

for the L0 hardware trigger in Run 3, the pile-up sensors were removed, and the remaining modules were re-arranged to ensure all particles in the detector acceptance pass through at least four modules. Furthermore, to cope with the harsher radiation environment close to the beamline, an innovative micro-channel cooling system was introduced. This system uses evaporative CO_2 circulating in narrow capillaries around the sensors, maintaining a stable operating temperature of approximately -25°C, improving the reliability and longevity of the sensors.
The Upstream Tracker (UT) replaced the previous TT tracker stations. The UT features silicon microstrip detectors in a four-layer configuration that offers improved granularity and radiation resistance. The strip pitch was reduced to 93.5 µm in the inner region and 187.5 µm in the outer region, improving the spatial resolution. The UT stations are now positioned closer to the beam by approximately 7 cm, contributing to better track reconstruction and momentum resolution.
The Scintillating Fibre (SciFi) tracker is the new main tracker located downstream of the magnet. It uses scintillating fibers grouped into 96 multi-layered mats, each 2.4 meters long with a diameter of 250 µm. The fibers are read out by Silicon PhotoMultipliers (SiPMs), which are maintained at -40°C to minimize noise and radiation damage. Each station is composed of four layers, ensuring redundancy and high efficiency in track reconstruction. The SciFi system covers an active area of 340 m^2 and provides a resolution better than 100 µm. This detector was specifically designed to deal with the high detector occupancy anticipated in Run 3.

Particle Identification System Upgrades

The particle identification (PID) system underwent several updates to handle higher data rates and improve performance. The RICH (Ring Imaging Cherenkov) detectors were upgraded with a redesigned optical system. Specifically, the focal length of the spherical mirrors in RICH1 was increased from 2.7 m to 3.7 m to reduce the high hit density in the central region of the detector. Moreover, the existing Hybrid PhotoDetectors (HPDs) were replaced with multianode photomultiplier tubes (MaPMTs), capable of sustaining the higher event rate expected during Run 3. This upgrade ensures that the PID system can continue to deliver high-quality particle identification, even under higher-luminosity conditions. The calorimeter and muon systems retained their previous structure, but the readout electronics were replaced to adapt to the new data acquisition rates.
The hardware L0 trigger, used in previous runs, was removed due to its inefficiency in handling higher luminosities. Instead, LHCb now uses a purely software-based trigger strategy, where the first trigger level (HLT1) operates on Graphics Processing Units (GPUs). This system performs partial event reconstruction at the 30 MHz input rate, reducing the event rate to 1 MHz. The HLT2 system then performs a full offline-quality event reconstruction asynchronously, reducing the data rate to about 10 Gb/s.
These changes ensure that LHCb can continue to explore new physics in the years to come with higher precision and efficiency.

Chapter 4

PYTHIA 8.3 Monte Carlo generator

PYTHIA [35] is a Monte Carlo event generator widely used in high-energy physics, capable of simulating particle collisions at various energy scales. Its latest version, PYTHIA 8.3, incorporates a comprehensive set of tools to model particle interactions, particularly focusing on the strong interaction, Quantum Chromodynamics (QCD), and phenomena extending beyond the Standard Model (BSM). The program also includes features tailored for simulations involving heavy ions, as well as astrophysical events such as dark matter annihilation into Standard Model particles.

4.1 Introduction to PYTHIA

PYTHIA event generation is structured into three main levels:

- **Process level:** Handles the hard scattering process and short-lived resonances, typically treated perturbatively at high energy scales.
- **Parton level:** Involves initial- and final-state radiation, parton showers, and multi-parton interactions. Color reconnection occurs at this stage to address the underlying event structure.
- **Hadron level:** Describes hadronization, where partons are confined into color-singlet hadrons through the string model. Additionally, unstable hadrons decay at this level.

At the core of PYTHIA is the MC method, which uses pseudo-random numbers to simulate particle interactions. The program employs a variety of MC techniques to generate physical events from theoretical distributions.
The internal event generation mechanism is divided into three stages:

- **Hard process:** The initial stage, where the main interaction (e.g., scattering of quarks or leptons) occurs.
- **Parton shower:** Initial and final-state radiation, including soft-gluon emissions and collinear parton splittings.
- **Hadronization:** The non-perturbative phase where partons combine into hadrons, modeled via string fragmentation.

PYTHIA is designed to handle a wide range of processes:

- **QCD processes:** Including both hard and soft QCD interactions, with an accurate treatment of light and heavy quarks, as well as gluon interactions.
- **Electroweak processes:** Involves the production of photons, W/Z bosons, and other electroweak particles.
- **Beyond Standard Model:** PYTHIA supports BSM theories such as supersymmetry (SUSY) and hidden valley models, extending its versatility in theoretical research.

In conclusion, one of the main characteristics of PYTHIA is that it is highly tunable, with parameters for parton showers, multi-parton interactions, and hadronization. The default tune, Monash 2013, provides a balanced configuration for most applications, although experiment-specific tunes are available. Users can also employ automatic tuning tools to optimize the parameters for specific datasets or experiments.

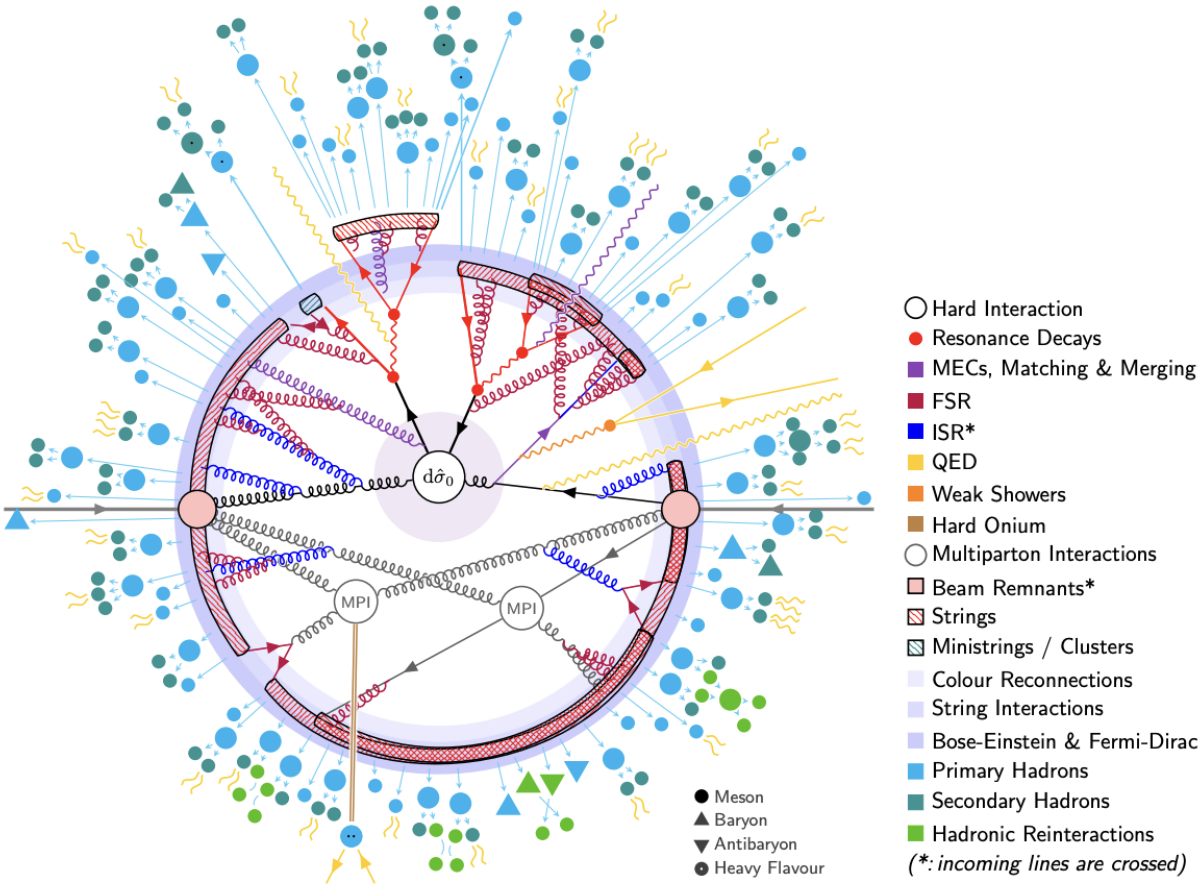

Figure 4.1: Simplified structure of PYTHIA 8.3, showing key components across the Process, Parton, and Hadron levels. From: [35]

4.2 Lund String Model

The Lund String Model is a widely used theoretical framework in PYTHIA for describing the hadronization process, which is how quarks and gluons produced in high-energy collisions transition into observable hadrons. The model builds on the

principle of confinement in QCD, which states that quarks cannot exist as free particles but must always be bound together in hadrons due to the increasing strength of the color force as they move apart.

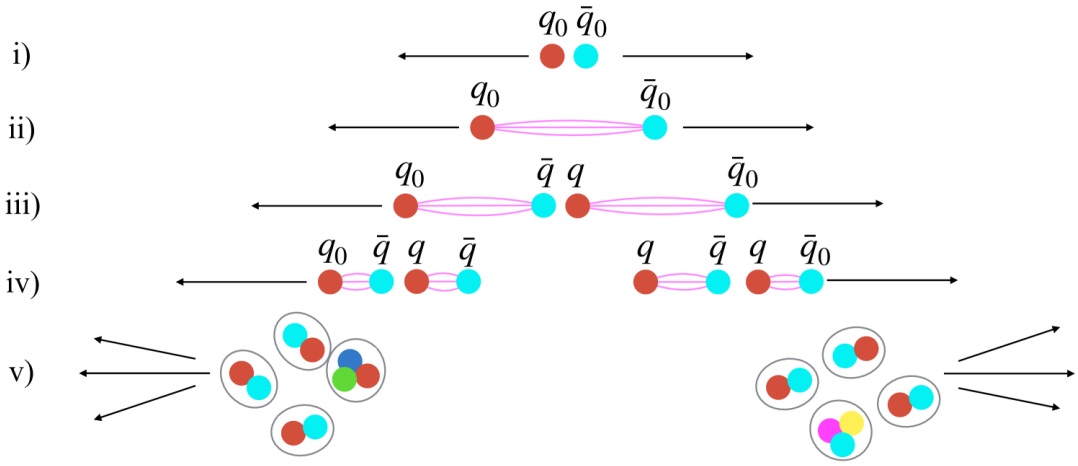

Figure 4.2: i) The initial quark and antiquark move away from each other after the collision. ii) A color string starts forming between them as they separate. iii) As the string stretches, it breaks at some point, producing a new quark-antiquark pair from the vacuum. iv) More string breaks happen as the process continues, creating additional pairs. v) The fragmentation results in jets composed of final-state hadrons, which are formed by the combination of quarks and antiquarks. From: [27]

In the Lund String Model, quarks and gluons are connected by a one-dimensional "string" of color field, Fig. [4.2]. When two quarks are pulled apart in a collision, this string stretches. Unlike the force in electromagnetism, which weakens with distance, the color force between quarks increases linearly as the string stretches. This linear increase in force continues until it reaches a point where it becomes energetically favorable to create a new quark-antiquark pair from the vacuum. The energy from the stretched string is then used to form these new quarks, which materialize as part of a new hadron. The key idea is that the string can break into smaller pieces, with each break corresponding to the formation of a new hadron. As the string fragments, quarks and antiquarks combine to form mesons (quark-antiquark pairs), or two quarks and a third quark combine to form baryons (three-quark systems). This process continues until the energy of the string is depleted, leaving only stable hadrons. The string fragmentation model is highly successful at describing the distributions and properties of the hadrons observed in high-energy particle collisions. In `PYTHIA`, the Lund String Model is implemented as the default hadronization mechanism for most processes involving quarks and gluons. It is responsible for simulating the transition from a high-energy parton-level interaction, where quarks and gluons are produced, to a final state where these partons are bound into hadrons that can be detected in experiments. The model relies on a few key parameters, which are typically tuned to experimental data to reproduce observed particle spectra and event shapes accurately. The string itself is modeled as a relativistic object, where the energy stored in the string is proportional to its length. As the string stretches between two moving quarks, it gains energy, and once the energy density reaches a critical threshold, a quark-antiquark pair is produced. This breaking of the string is treated as a probabilistic process, where the proba-

bility of string breaking and the resulting momentum distribution of the produced hadrons follow certain rules dictated by the model. The Lund String Model also accounts for various important effects such as color reconnection, where the color flow in a collision event can change due to interactions between different strings, and baryon production, which involves more complex string junctions where multiple quarks combine to form baryons. One of the strengths of the Lund String Model is its ability to describe a wide range of phenomena in hadron-hadron, lepton-hadron, and even heavy-ion collisions. The model parameters, such as the string tension (the force per unit length along the string) and the probability for string breaking, can be adjusted to fit different experimental conditions, making it a versatile tool for studying particle physics. In summary, the Lund String Model plays a crucial role in PYTHIA by providing a detailed and physically motivated description of the hadronization process. By modeling the confinement of quarks and the fragmentation of the color string, it allows PYTHIA to simulate realistic final states that closely match the particles observed in collider experiments.

4.3 Comparison between PYTHIA and data

In this section, the aim is to present some comparisons between the experimental data and the results obtained through PYTHIA in order to understand the level of reliability this event generator has in terms of describing the physics under study.

The integrated yields of charged particles in pp collisions at $\sqrt{s} = 13$ TeV for three transverse momentum ranges ($2 < p_T < 10\,\mathrm{GeV}/c$, $4 < p_T < 10\,\mathrm{GeV}/c$, and $6 < p_T < 10\,\mathrm{GeV}/c$) are shown as a function of the average multiplicity density in the middle pseudo-pseudorapidity ($|\eta| < 0.5$) in Fig. [4.3]. Both the charged-particle yields and the average multiplicity are self-normalized. The yields for high-p_T charged particles ($p_T > 4\,\mathrm{GeV}/c$) increase more rapidly than the overall charged-particle multiplicity. However, this increase is less pronounced for lower-p_T particles. The trend of the data is qualitatively well reproduced by PYTHIA 8, but for $p_T > 6$ GeV/c the model significantly overestimates the ratio by a factor greater than 1.5.

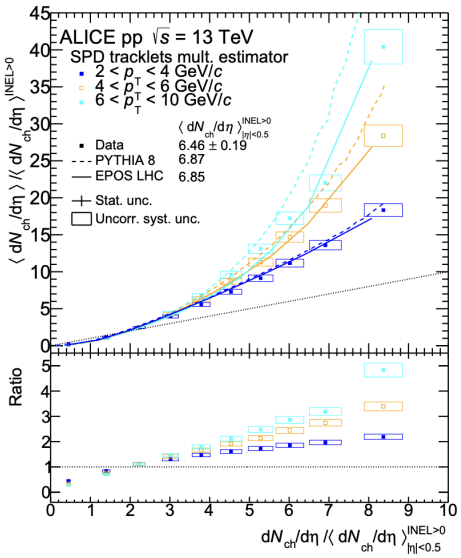

Figure 4.3: The self-normalized yields of charged particles, integrated over three different p_T intervals, are shown for pp collisions at $\sqrt{s} = 13$ TeV as a function of the charged-particle density at mid-pseudorapidity. Data are compared with predictions from `PYTHIA 8` (dashed lines). A dotted line is added to highlight the difference between the data and the linear dependence. The deviations from the linear trend are displayed in the lower panel. From: [13].

In Fig. [4.4], the distribution of the average charged-particle density $\langle dN_{\mathrm{ch}}/d\eta \rangle$ measured in the pseudorapidity range $|\eta| < 1.8$ in pp collisions at $\sqrt{s} = 13$ TeV is reported. The data points have been symmetrized by averaging the results obtained in $+\eta$ and $-\eta$, which were found to be consistent with the statistical uncertainties. The measurements are compared to Monte Carlo simulations using `PYTHIA 6` (Perugia-2011), `PYTHIA 8` (Monash-2013), and `EPOS LHC`. Among the simulations, `PYTHIA 6` provides better agreement with the data than `PYTHIA 8`, with `PYTHIA 8` overestimating the data.

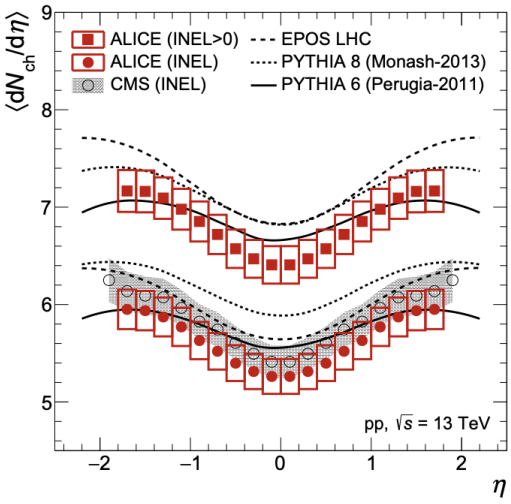

Figure 4.4: The charged-particle pseudorapidity density in the central pseudorapidity region $|\eta| < 0.5$ in pp collisions at $\sqrt{s} = 13$ TeV were measured at the LHC. The uncertainties are calculated as the quadratic sum of statistical and systematic contributions. The lines represent predictions from MC event generators (see text for details). From: [21].

The p_T spectra for different hadrons as measured by ALICE in pp collisions at $\sqrt{s} = 13$ and 7 TeV are compared in Fig. [4.5] to predictions from various Monte Carlo models, including `PYTHIA 8` (Monash 2013 tune), `PYTHIA 6` (Perugia 2011 tune), and `EPOS-LHC`, by means of the model-to-data ratio. For protons and antiprotons ($p + \bar{p}$, panel h), `PYTHIA 8` and `PYTHIA 6` give a good agreement with the data in the range $1 < p_T < 5$ GeV/c. Below 1 GeV/c and above 5 GeV/c, the production is overestimated by up to a factor of two.

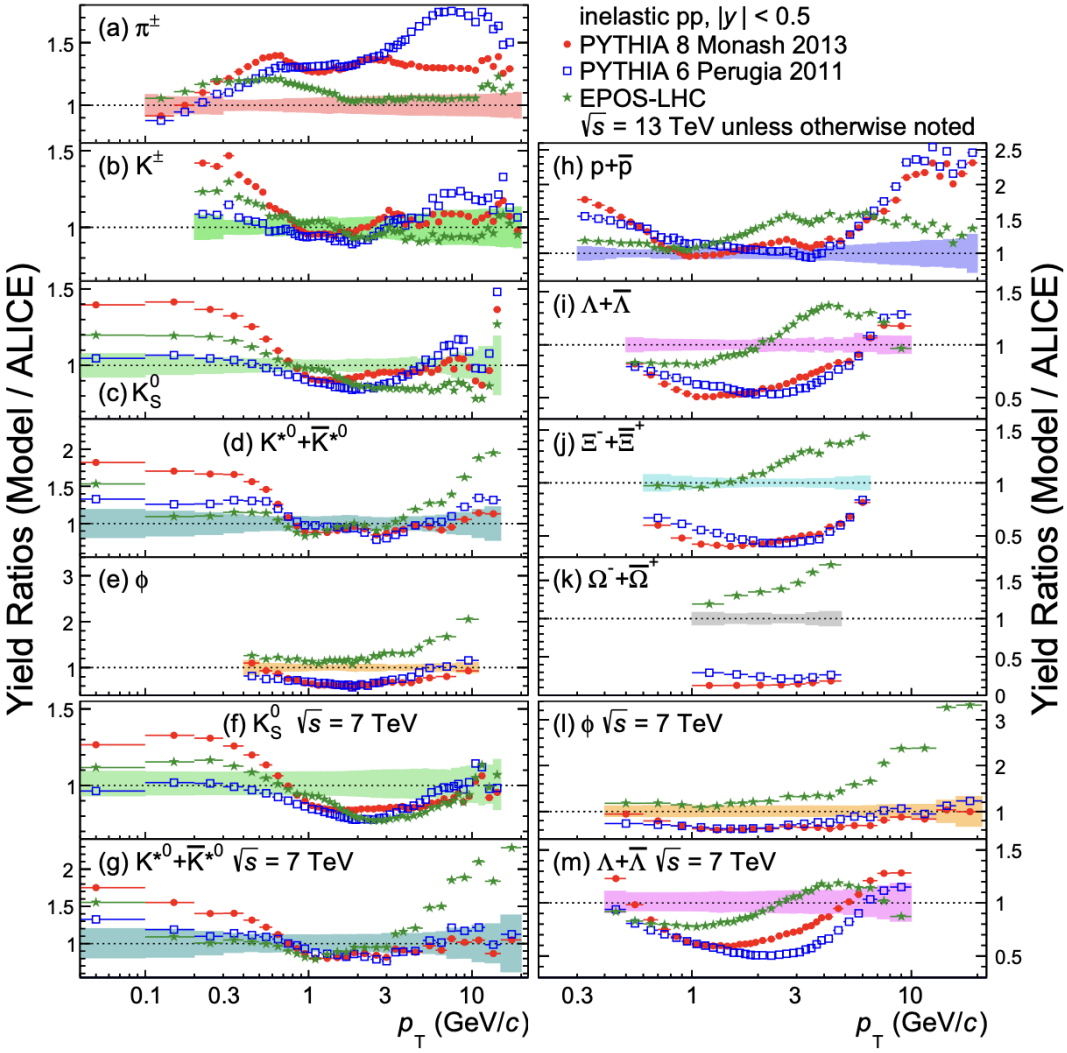

Figure 4.5: Ratios of p_T spectra from `PYTHIA 8` (Monash 2013), `PYTHIA 6` (Perugia 2011), and `EPOS-LHC` model predictions to the p_T spectra measured by ALICE for various hadrons. The data correspond to pp collisions at $\sqrt{s} = 13$ TeV, with specific panels showing the results for 7 TeV. From: [17].

4.3.1 Predictions on baryon to meson ratio

In the chapter concerning the analysis conducted for this thesis work, we will analyze and vary one of the parameters of the `PYTHIA` simulation that affects the baryon-to-meson production ratio. For this reason, some of the experimental results obtained at the LHC have been chosen to be presented. Fig. [4.6] shows the integrated proton-to-pion (p/π) yield ratios as a function of $\langle dN_{\rm ch}/d\eta \rangle$ for pp, p–Pb, and Pb–Pb at different center-of-mass energies. The data points from ALICE are compared with

PYTHIA 8 and HERWIG 7 predictions. The p/π ratio shows a significant increase as a function of multiplicity in pp collisions at $\sqrt{s} = 13$ TeV, reaching a plateau at higher multiplicities. All considered versions of PYTHIA 8 overpredict the data. HERWIG 7 provides a more consistent description of the experimental data. The color ropes implementation in PYTHIA 8, which simulates a higher effective string tension during hadronization, results in an even stronger increase in the p/π ratio at high multiplicity, exceeding the experimental measurements. This suggests that the current color rope implementation overestimates the contribution of baryons at high charged-particle densities. In general, none of the models perfectly reproduces the ratio p/π across the entire multiplicity range, highlighting the need for further tuning of the models to fully capture the dynamics of baryon production in high-energy collisions.

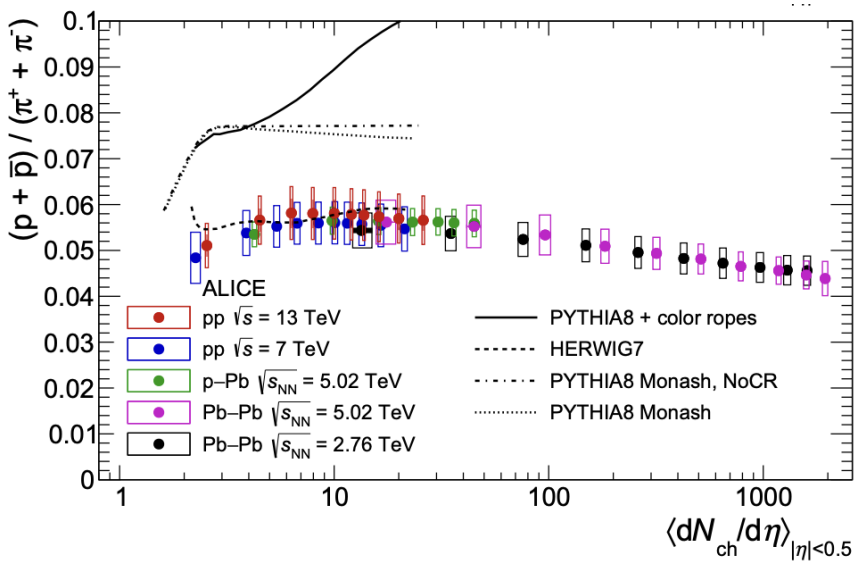

Figure 4.6: p_T-integrated p/π yield ratios as a function of charged-particle multiplicity density, measured by ALICE in pp, p–Pb, and Pb–Pb collisions at various center-of-mass energies. Data are compared with predictions from PYTHIA 8 (Monash and color ropes) and HERWIG 7. Modified from: [14].

The plot in Fig. [4.7] compares the p_T-dependent baryon-to-meson ratios obtained from experimental data with those simulated using the PYTHIA 8 event generator. The data represents results from pp collisions at $\sqrt{s} = 13$ TeV, measured at mid-rapidity ($|y| < 0.5$) and forward rapidity ($2.5 < y < 4.5$) by ALICE and LHCb, respectively. The key baryon-to-meson ratios displayed are Λ_c^+/D^0, Λ/K_S^0, and p/π^+. Additionally, the $\Lambda_b^0/(B^0 + B^+)$ ratio is shown, as measured by LHCb in the forward region. The PYTHIA predictions are compared with the Monash 2013 tune and different CLR-BLC tunes (Modes 0, 2, and 3), which implement various fragmentation models. Although the Monash tune, which is optimized for e^+e^- collisions, tends to underestimate the baryon-meson ratios for beauty, charm, and strange hadrons at low p_T, a better agreement is observed for the p/π^+ ratio. The CLR-BLC tunes, particularly Modes 2 and 3, show improved agreement with experimental results for beauty and strange hadrons, especially at higher p_T values ($p_T > 2$ GeV/c).

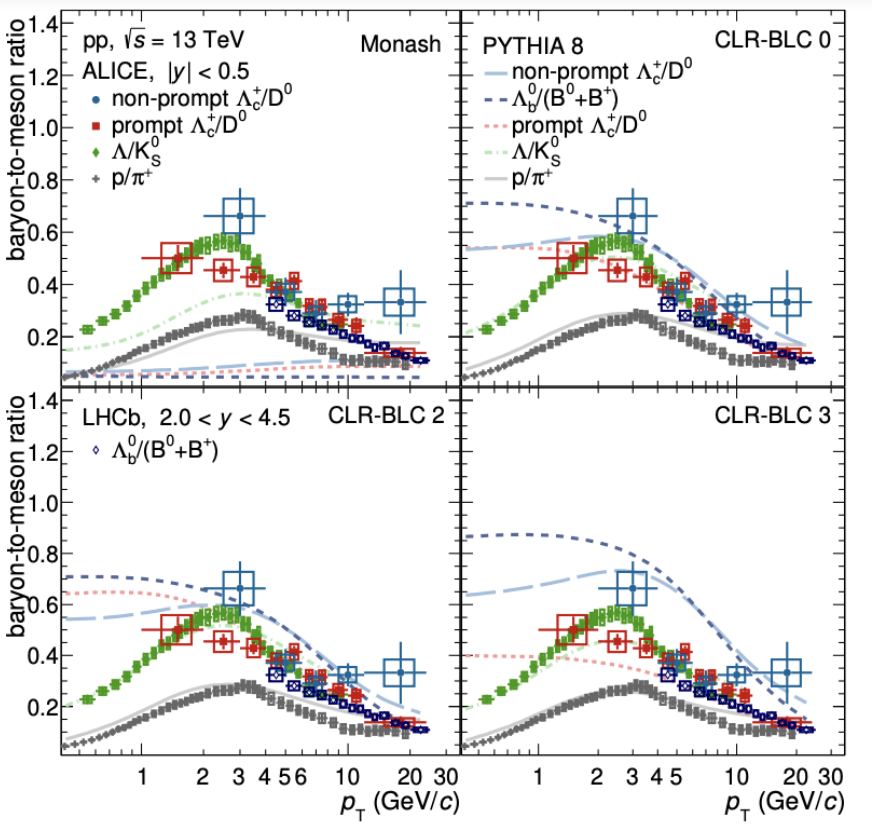

Figure 4.7: The non-prompt Λ_c^+/D^0, prompt Λ_c^+/D^0, Λ/K_S^0, and p/π^+ ratios were measured in proton-proton collisions at $\sqrt{s} = 13$ TeV at midrapidity ($|y| < 0.5$) and are compared to the $\Lambda_b^0/(B^0 + B^+)$ ratio, which was recorded by the LHCb Collaboration at forward rapidity ($2.5 < y < 4$). These experimental results are then contrasted with predictions from the `PYTHIA` 8 Monte Carlo generator, utilizing the Monash 2013 tune and the CLR-BLC tunes (modes 0, 2, and 3), all within the corresponding rapidity ranges, to assess their agreement with the data. From: [19]

4.3.2 Predictions on the production cross sections ratio

The $\overline{\Lambda}_b$ will play a crucial role throughout this dissertation; for this reason, some of the experimental results on production cross-section ratios are presented below. The results presented in Fig. [4.8] demonstrate that the ratio $\sigma(\Lambda_b)/\sigma(\overline{\Lambda}_b)$ is consistent with unity in the selected ranges of p_T and rapidity [39]. This observation indicates that no significant baryon-antibaryon asymmetry is present within the uncertainties of the measurement. Specifically, the ratio remains consistent with unity across all p_T bins, with a small statistical fluctuation in the highest p_T bin. The rapidity distribution also does not show a significant deviation from unity, supporting the hypothesis of symmetric production rates for Λ_b and $\overline{\Lambda}_b$ in pp collisions at $\sqrt{s} = 7$ TeV. The data were compared to predictions from `POWHEG` and `PYTHIA`, both of which assume equal production of baryons and antibaryons in this kinematic region. The theoretical predictions are shown as lines in Fig. [4.8], and the agreement with the data suggests that the current theoretical models accurately describe the symmetry in baryon and anti-baryon production at this energy scale. The error bars in the figure include both statistical and systematic uncertainties, and the shaded areas represent the uncertainties on the theoretical predictions.

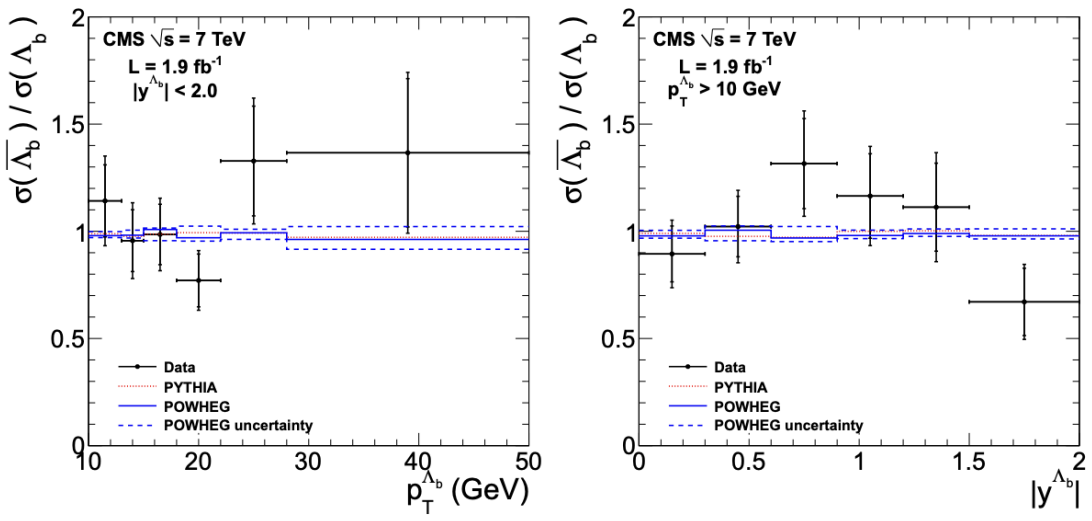

Figure 4.8: Measured ratio of the cross-sections $\sigma(\Lambda_b)/\sigma(\overline{\Lambda}_b)$ as a function of transverse momentum p_T (left) and rapidity $|y|$ (right), compared to theoretical predictions from `POWHEG` and `PYTHIA`. The data points show no significant deviation from unity, indicating symmetric production of Λ_b and $\overline{\Lambda}_b$ baryons. The error bars include both statistical and systematic uncertainties. From: [39].

The Fig. [4.9] shows the ratio of the production cross-sections of Λ_b^0 baryons to B^0 mesons as a function of transverse momentum p_T, recently measured by the LHCb Collaboration in pp collisions at a center-of-mass energy of $\sqrt{s} = 13\,\text{TeV}$. The data sample corresponds to an integrated luminosity of 5.4 fb^{-1}. The ratio of the production cross sections is given by:

$$\frac{\sigma(\Lambda_b^0)}{\sigma(B^0)} = \frac{N_{\Lambda_b^0}}{N_{B^0}} \times \frac{B(B^0)}{B(\Lambda_b^0)} \times \frac{\epsilon_{\text{acc}}(B^0)}{\epsilon_{\text{acc}}(\Lambda_b^0)} \times \frac{\epsilon_{\text{rec}}(B^0)}{\epsilon_{\text{rec}}(\Lambda_b^0)} \tag{4.1}$$

where $N_{\Lambda_b^0}$ and N_{B^0} represent the yields of Λ_b^0 baryons and B^0 mesons, respectively, extracted from invariant mass fits. The branching fractions of the relevant decay channels are denoted by $B(\Lambda_b^0)$ and $B(B^0)$. The terms ϵ_{acc} and ϵ_{rec} represent the acceptance and reconstruction efficiencies, respectively, for each hadron. The results show a significant p_T-dependence of the ratio, with a larger Λ_b^0 to B^0 production ratio at low transverse momentum. The experimental data are compared to theoretical predictions from models like `PYTHIA8` and `EPOS4HQ`, as well as statistical hadronization models (SHM). At low p_T, `PYTHIA` is not consistent with the data, but the description improves at p_T higher than 15 GeV/c.

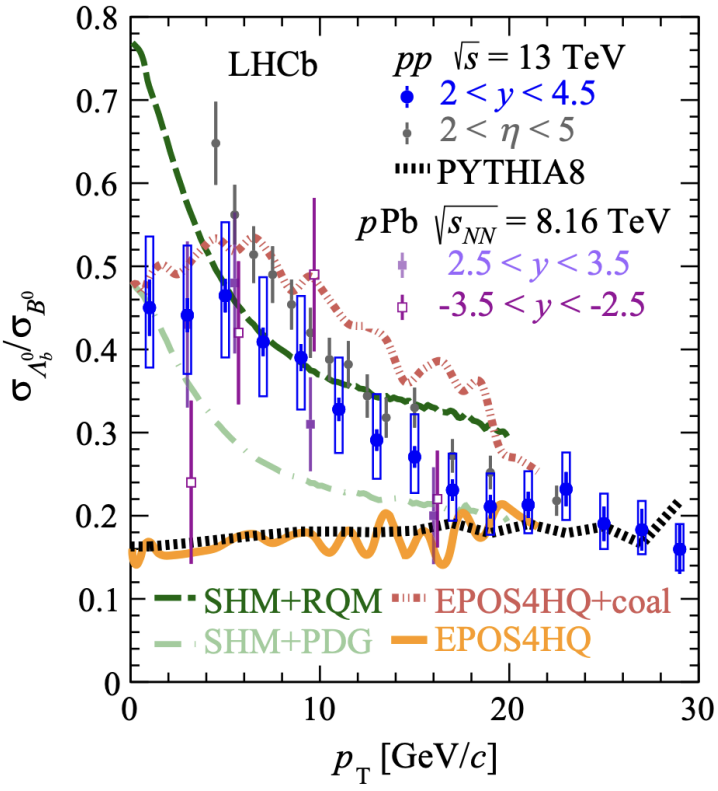

Figure 4.9: Ratio of the production cross-sections of Λ_b^0 baryons to B^0 mesons as a function of transverse momentum p_T, measured by the LHCb Collaboration at $\sqrt{s} = 13\,\text{TeV}$. The data are compared to theoretical predictions from `PYTHIA8` and `EPOS4HQ`. The error bars represent the statistical and systematic uncertainties. From: [5].

4.4 $b\bar{b}$ Production in `PYTHIA`

In `PYTHIA`, the cross section for $b\bar{b}$ production is computed using matrix elements derived from perturbative QCD, which are convoluted with the proton Parton Distribution Functions (PDFs). These PDFs describe the momentum distribution of partons within the nucleons, which is crucial for calculating the cross section in proton-proton collisions. At leading order (the simplest level of approximation in a perturbative expansion in Quantum Field Theory (QFT), particularly in Quantum Chromodynamics (QCD)), the dominant production mechanism for $b\bar{b}$ pairs is gluon-gluon fusion ($g + g \to b\bar{b}$). However, `PYTHIA` also accounts for heavy-quark production through additional processes, such as parton-shower splittings, where a gluon from the parton shower undergoes a splitting ($g \to b\bar{b}$). These splittings occur during both the initial and final state parton evolution, allowing for $b\bar{b}$ production beyond the hard process. In particular, three main mechanisms contribute to heavy-flavor production:

- **Pair creation**: The hard process is initiated by the $g + g \to b\bar{b}$ subprocess. Here, the parton shower can modify the kinematics by producing additional radiation but does not alter the overall cross section.
- **Flavour excitation**: A gluon from one of the incoming partons may split into a $b\bar{b}$ pair prior to the hard scattering, introducing heavy quarks into the hard subprocess.

- **Gluon splitting**: Gluons emitted in the parton shower (typically in the final state) can split into $b\bar{b}$ pairs, producing additional heavy quarks.

These processes, in particular, the gluon splitting, become increasingly important at high energies, such as those encountered at the LHC. In Fig. [4.10], we present a schematic view of the different production mechanisms for $b\bar{b}$ quark pairs, highlighting both the hard-process contributions and the gluon-splitting processes during the parton shower.

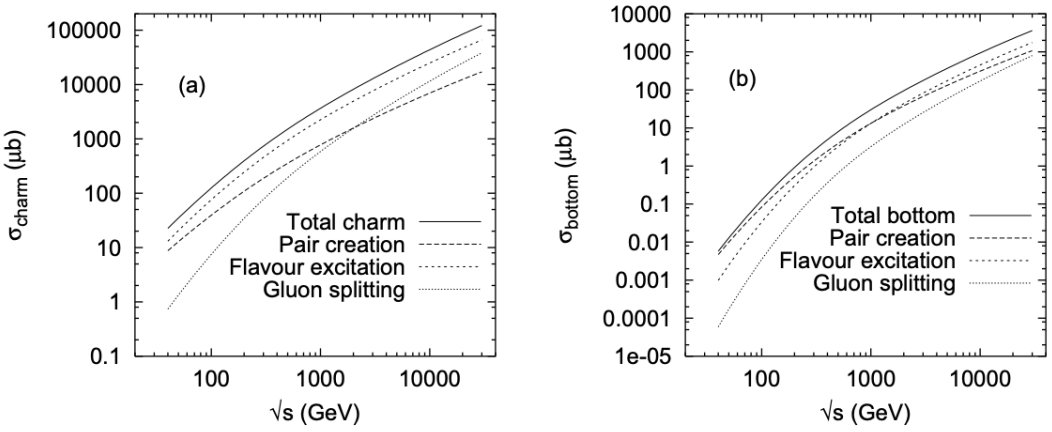

Figure 4.10: Heavy-flavor production mechanisms in proton-proton collisions. The diagram shows both the leading-order processes ($g + g \to b\bar{b}$) and gluon-splitting ($g \to b\bar{b}$) during parton showers. From: [56].

4.4.1 Comparison with ALICE Results

The ALICE collaboration measured the $b\bar{b}$ production cross sections in proton-proton collisions at different center-of-mass energies, as presented in Fig. [4.11]. Specifically, this figure shows the beauty-quark production cross section, $d\sigma_{b\bar{b}}/dy|_{y=0}$, as a function of $\sqrt{s}$. The measurements include contributions from various decay channels: $b \to D$, $b \to J/\psi$, and $b \to e$, providing an extensive set of experimental data points across a broad energy range. The experimental points are compared with both theoretical predictions and simulations:

- **FONLL** (Fixed Order Next-to-Leading Logarithms): This is represented by the blue shaded band, which takes into account the uncertainties related to the renormalization and factorization scales, as well as the heavy-quark masses and parton distribution functions (PDFs). FONLL is a well-established pQCD framework that provides accurate predictions for heavy-quark production.

- **NNLO** (Next-to-Next-to-Leading Order): Represented by the green dashed lines with the shaded uncertainty band, these calculations include higher-order QCD corrections, which improve the precision of the cross-section predictions.

- `PYTHIA` **Simulations**: The figure also compares the ALICE data with `PYTHIA` 6 and `PYTHIA` 8 predictions utilizing POWHEG, which incorporates next-to-leading-order corrections.

The ALICE results, denoted by different markers corresponding to the decay channels, are in good agreement with the FONLL and NNLO predictions across the full energy range. The beauty production cross sections measured by ALICE at $\sqrt{s} = 5.02$ TeV, using non-prompt D mesons and other decay channels, lie within the uncertainty bands of the theoretical models, confirming the validity of the perturbative QCD calculations. The results obtained with `PYTHIA` simulations show good agreement with the data in the range $5 < \sqrt{s} < 7$ TeV.

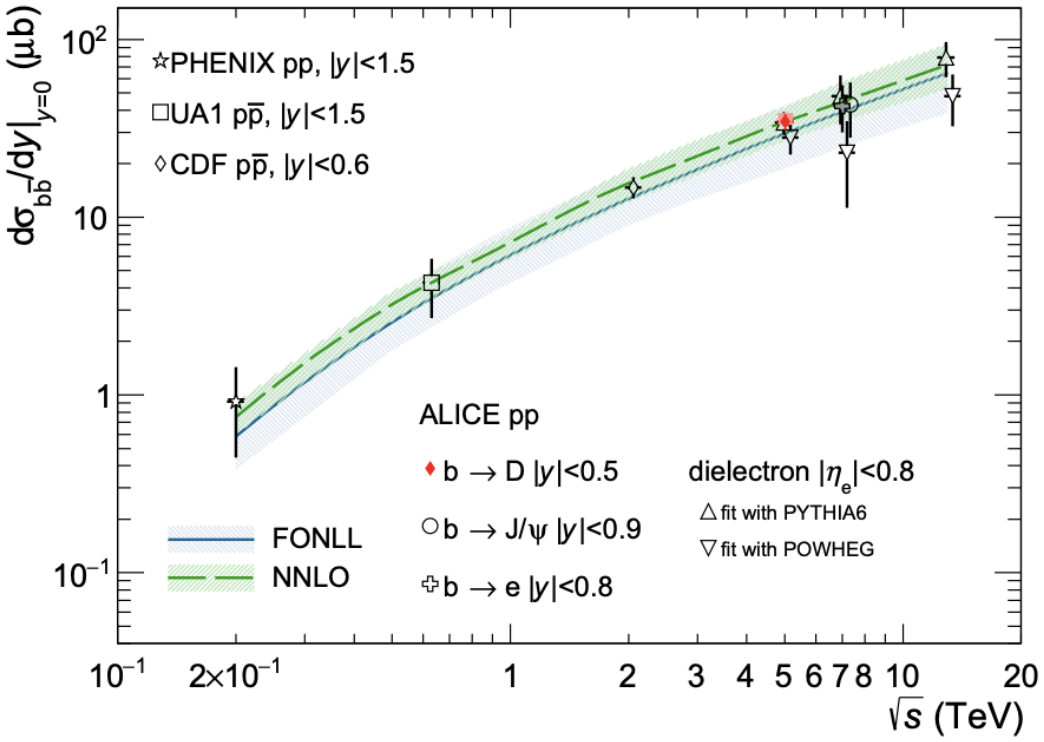

Figure 4.11: Beauty production cross section $d\sigma_{b\bar{b}}/dy|_{y=0}$ as a function of center-of-mass energy $\sqrt{s}$. The data points represent experimental measurements from ALICE and other experiments, compared with theoretical predictions from FONLL (blue) and NNLO (green). From: [16].

Chapter 5

Experimental study of the Λ_b baryon and its properties

This chapter aims to provide an overview of the properties of the bottom baryon Λ_b. It will present its characteristics and the current knowledge about this particle, deriving from experimental results.

In the quark model, Λ_b^0 is an isospin-0 state consisting of u, d, and b quarks. The lowest state of Λ_b^0 is expected to have $J^P = \frac{1}{2}^+$. However, quantum numbers such as isospin I, total angular momentum J, or parity P have not yet been directly measured.

5.1 Λ_b mass

The mass of the Λ_b^0, as reported by the Particle Data Group (PDG) [77], is:

$$m_{\Lambda_b^0} = 5619.60 \pm 0.17\,\text{MeV}/c^2$$

Below, the most recent measurement of the Λ_b mass is presented as reported in the literature.

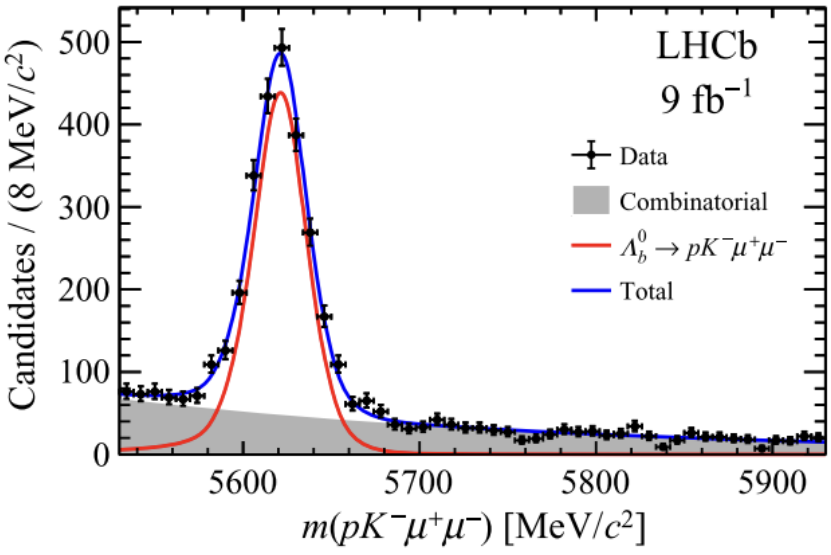

Figure 5.1: Mass distribution reconstructed via the decay: $\Lambda_b^0 \to pK^-\mu^+\mu^-$. From: [4].

The plot in Fig. [5.1] shows the invariant mass distribution of the decay candidates $\Lambda_b^0 \to pK^-\mu^+\mu^-$, collected by the LHCb experiment with a pp collision integrated luminosity of 9 fb^{-1} at center-of-mass energies of 7, 8, and 13 TeV. To identify Λ_b^0 candidates, the data were reconstructed from proton (p), kaon (K^-), and dimuon ($\mu^+\mu^-$) tracks, all originating from a common vertex. In the plot, the black points represent the experimental data, whereas the red and blue curves correspond to fits performed on the mass distribution. The red line represents the $\Lambda_b^0 \to pK^-\mu^+\mu^-$ signal component, while the blue line represents the total fit, including both the signal and the combinatorial background (shown as the grey area). The peak of the distribution around 5620 MeV/c^2 corresponds to the Λ_b^0 signal, and the width of the peak is consistent with the expected detector resolution.

5.2 Λ_b lifetime

The lifetime of the Λ_b, as reported by the PDG [77], is:

$$\tau_{\Lambda_b} = 1.471 \pm 0.009 \text{ ps}.$$

From this, we can easily derive the *decay length* as:

$$c\tau_{\Lambda_b} \simeq 441.3\ \mu m \tag{5.1}$$

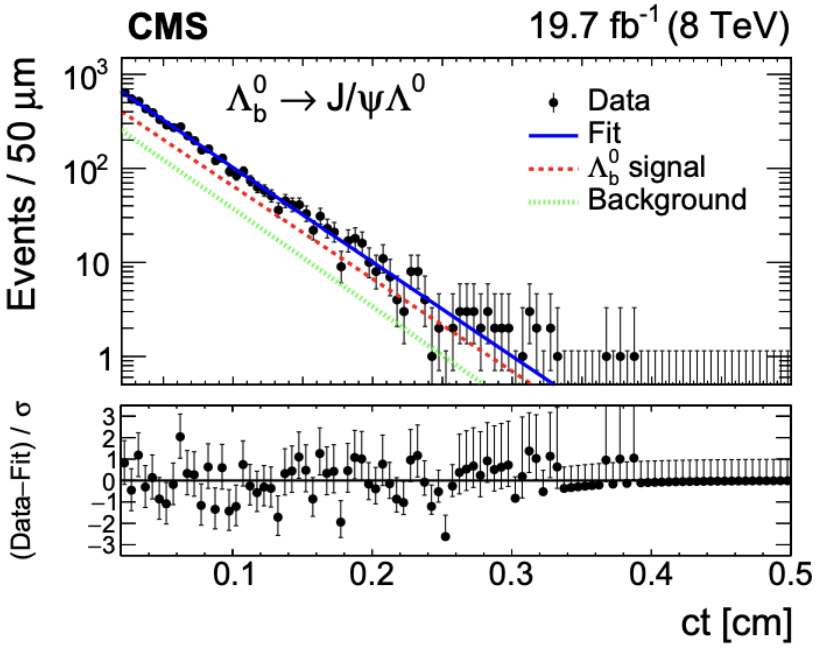

Figure 5.2: The ct distribution for Λ_b^0 candidates. The solid curve represents the total fit, which includes contributions from both the signal (dashed line) and the background (dotted line). The lower sub-panel shows the residuals, which are the differences between the observed data and the fit, normalized by the statistical uncertainty in the data points. From: [66].

The CMS Collaboration [66] measured the lifetime of the Λ_b^0 baryon using data collected at $\sqrt{s} = 8$ TeV, corresponding to an integrated luminosity of 19.7 fb^{-1}. The decay channel analyzed was $\Lambda_b^0 \to J/\psi\Lambda^0$, where J/ψ decays into two oppositely

charged muons ($\mu^+\mu^-$), and Λ^0 decays into a proton and a pion ($p\pi^-$). The analysis utilizes the proper decay time distribution (ct) of the candidates Λ_b^0 to extract the lifetime. The upper plot shows black points that represent the data, while the solid blue line corresponds to the total fit, which includes the Λ_b^0 signal (red dashed line) and the background (green dotted line). The signal region exhibits an exponential decay, characteristic of a particle's lifetime distribution, while the background is modeled with a separate component, primarily combinatorial in nature. The lower plot shows the residuals, defined as the difference between the data and the fit, normalized by the uncertainty in the data points.

5.3 Λ_b decay modes

Below, we present the main decay channels along with their corresponding branching ratio values, in accordance with those reported by the PDG [77]:

- $\Lambda_b^0 \to \Lambda_c^+ \; l^- \overline{\nu}_l$ anything $\quad \Gamma_i/\Gamma = (10.9 \pm 2.2)\%$
- $\Lambda_b^0 \to \Lambda_c^+ \; l^- \overline{\nu}_l \quad \Gamma_i/\Gamma = (6.2^{+1.4}_{-1.3})\%$
- $\Lambda_b^0 \to \Lambda_c^+ \; \pi^+ \; \pi^- \; l^- \; \overline{\nu}_l \quad \Gamma_i/\Gamma = (5.6 \pm 3.1)\%$
- $\Lambda_b^0 \to \Lambda_c^+ \; \tau^- \overline{\nu}_\tau \quad \Gamma_i/\Gamma = (1.9 \pm 0.5)\%$
- $\Lambda_b^0 \to \Lambda_c(2625)^+ \; l^- \overline{\nu}_l \quad \Gamma_i/\Gamma = (1.3^{+0.6}_{-0.5})\%$
- $\Lambda_b^0 \to \Lambda_c^+ \; D_s^- \quad \Gamma_i/\Gamma = (1.10 \pm 0.10)\%$
- $\Lambda_b^0 \to \Lambda_c(2596)^+ \; l^- \overline{\nu}_l \quad \Gamma_i/\Gamma = (7.9^{+4.0}_{-3.5}) \times 10^{-3}$
- $\Lambda_b^0 \to \Lambda_c^+ \; \pi^+ \; \pi^- \; \pi^- \quad \Gamma_i/\Gamma = (7.6 \pm 1.1) \times 10^{-3}$
- $\Lambda_b^0 \to \Lambda_c^+ \; \pi^- \quad \Gamma_i/\Gamma = (4.9 \pm 0.4) \times 10^{-3}$

In the case of our analysis, the relevant decays are those leading to the production of (anti)nucleons in the final state, as they are the particles involved in the production of antideuterons. The study of these decay channels, which were carried out through simulations, will be shown in the next chapter.

5.4 Λ_b cross-section

Λ_b cross-section in pp collisions at 7 TeV

The differential cross section as a function of the transverse momentum p_T for the production of Λ_b baryons and antibaryons in proton-proton collisions in $\sqrt{s} = 7\,\text{TeV}$ was measured by the CMS Collaboration using the $\Lambda_b \to J/\psi\Lambda$ decay channel. The Λ_b baryons were reconstructed from the decay chains $J/\psi \to \mu^+\mu^-$ and $\Lambda \to p\pi$, with a data sample corresponding to an integrated luminosity of 1.9 fb^{-1}. The differential cross section $d\sigma/dp_T$ was calculated using the formula:

$$\frac{d\sigma(pp \to \Lambda_b X)}{dp_T} \times B(\Lambda_b \to J/\psi\Lambda) = \frac{n_{\text{sig}}}{2 \cdot \epsilon \cdot B \cdot L \cdot \Delta p_T} \tag{5.2}$$

where n_{sig} represents the number of signal events, ϵ is the average efficiency for reconstructing the signal, L is the integrated luminosity, Δp_T is the bin width in p_T, and B is the product of branching fractions $B(J/\psi \to \mu^+\mu^-) = 5.93 \times 10^{-2}$ and $B(\Lambda \to p\pi) = 0.639$. The factor of 2 accounts for the inclusion of Λ_b and $\overline{\Lambda}_b$ in the analysis. In Fig. [5.3], the measured cross sections were compared to theoretical predictions from `POWHEG` and `PYTHIA`. The p_T spectrum was observed to fall more steeply than predicted by both `POWHEG` and `PYTHIA`, especially in the high p_T region, where the experimental data show a lower cross section compared to the theoretical expectations.

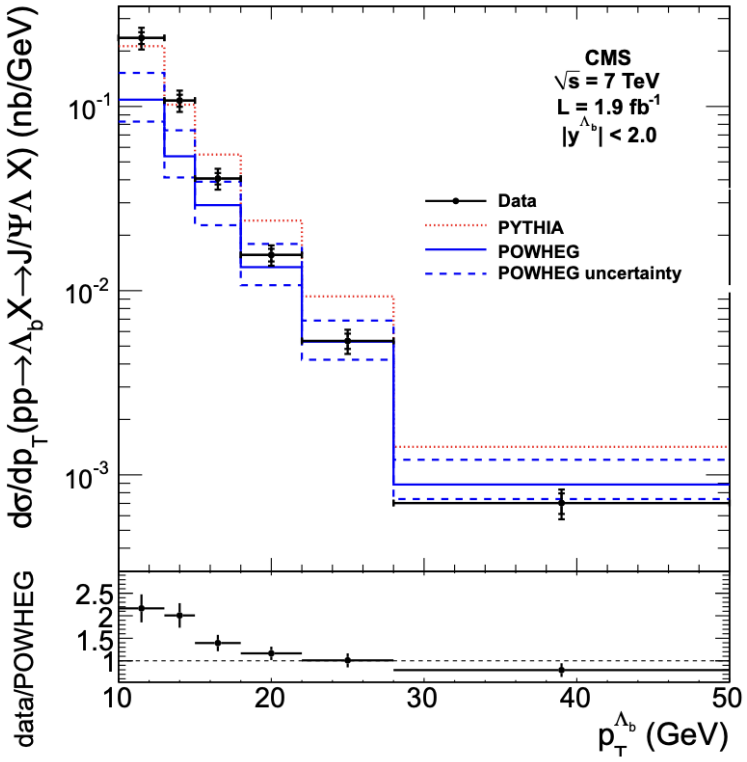

Figure 5.3: Measured differential cross-sections $d\sigma/dp_T \times B(\Lambda_b \to J/\psi\Lambda)$ as a function of p_T, compared to the theoretical predictions from `POWHEG` and `PYTHIA`. The error bars represent the statistical and systematic uncertainties. We can observe that the experimental data shows a faster decline in cross-section at high p_T compared to both theoretical predictions, particularly in the region $p_T > 20\,\text{GeV}$. From: [39].

In Figure 5.4, the product of the differential production cross-sections and the corresponding branching fractions for the decays $\Lambda_b^0 \to J/\psi p K^-$ and $B^0 \to J/\psi K^{*0}$ is shown as a function of transverse momentum p_T in different rapidity ranges. The measurements were carried out by the LHCb Collaboration using data collected in 2011 at $\sqrt{s} = 7\,\text{TeV}$ and 2012 at $\sqrt{s} = 8\,\text{TeV}$, with a combined integrated luminosity of 3 fb^{-1}. The product of the differential cross section and the branching fraction, $d^2\sigma/dp_T dy \times B$, is calculated as:

$$\frac{d^2\sigma}{dp_T dy} \times B = \frac{N(p_T, y)}{\epsilon(p_T, y) L B_{\text{inter}} \Delta p_T \Delta y} \tag{5.3}$$

where $N(p_T, y)$ represents the signal yield, $\epsilon(p_T, y)$ is the efficiency as a function of p_T and rapidity y, L is the integrated luminosity, and B_{inter} is the product of

branching fractions of the intermediate decays: $J/\psi \to \mu^+\mu^-$ for Λ_b^0, or $J/\psi \to \mu^+\mu^-$ and $K^{*0} \to K^-\pi^+$ for B^0. The measurements are conducted in the kinematic region $p_T < 20\,\text{GeV/c}$ and $2.0 < y < 4.5$. The results show that the production cross-sections for both Λ_b^0 and B^0 baryons decrease with increasing p_T. The error bars represent the total uncertainties, which include both statistical and systematic components. From the comparison of Λ_b^0 and B^0 production cross-sections across different rapidity ranges, it can be observed that the B^0 mesons have a higher production rate than Λ_b^0 baryons throughout the p_T range. This result aligns with known differences in fragmentation fractions between beauty hadrons and indicates a higher production of B^0 mesons compared to Λ_b^0 baryons in proton-proton collisions at the LHC.

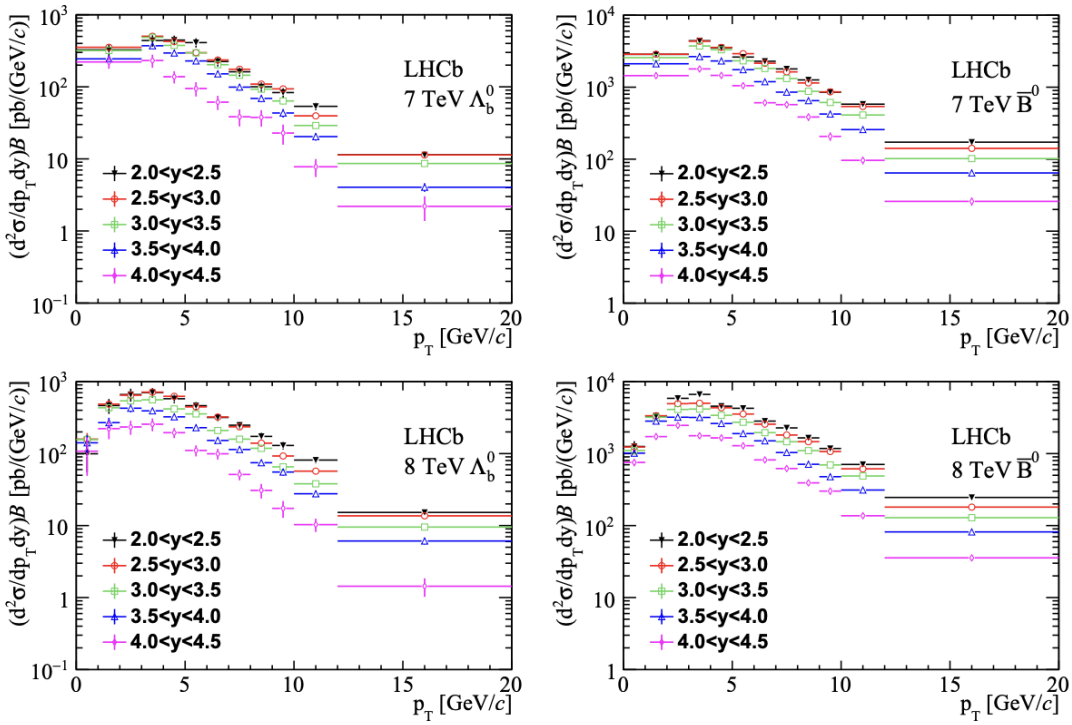

Figure 5.4: Products of differential production cross-sections and branching fractions as functions of p_T in different rapidity bins for (left) $\Lambda_b^0 \to J/\psi p K^-$ and (right) $B^0 \to J/\psi K^{*0}$. The top plots represent the 2011 data sample at $\sqrt{s} = 7\,\text{TeV}$, while the bottom plots represent the 2012 data sample at $\sqrt{s} = 8\,\text{TeV}$. The error bars represent total uncertainties. From: [1].

Chapter 6

Determination of the $\overline{\Lambda}_b \to \overline{\mathrm{d}} + X$ branching ratio

This chapter is dedicated to the analysis performed in order to estimate the branching ratio of $\overline{\Lambda}_b$ decaying into antideuterons in the final state, which is the core of this thesis. The starting point is the explanation of the setup of the simulation carried out using `PYTHIA 8.3`, including the parameters used and the results obtained. Next, the two coalescence models used to generate antideuterons in the final state are described. The first model, a classical approach, follows the work introduced in Sec. 1.3. The second, a quantum-mechanical approach, follows the MC coalescence method outlined in Sec.2.4. Finally, the results are presented and discussed in light of possible studies of the Λ_b decay into antideuteron with the ALICE and LHCb detectors at the LHC.

6.1 Λ_b Tune in `PYTHIA 8.3`

To perform the analysis, I implemented a simulation using `PYTHIA` with a focus on the production of $\overline{\Lambda}_b$ particles. These particles can decay, producing antinucleons (specifically antiprotons and antineutrons) in the final state. Through the coalescence process, these antinucleons can bind to form antideuterons. The tune used for the simulation is the Monash Tune 2013 [67], corresponding to option 14. The version of `PYTHIA` used is 8.3.
One of the key parameters in the simulation is `probQQtoQ`. This parameter, introduced in Section 1.3, is tuned to match the LEP measurement of $f(b \to \Lambda_b) \simeq 0.1$. In `PYTHIA`, `probQQtoQ` controls the suppression of diquark production relative to quark production, which corresponds to baryon production relative to meson production. The default value of this parameter is 0.081, but to reproduce the LEP measurement, we use a value of 0.24. The first step of the analysis was to reproduce the results reported in Table I of [75], which are related to the results discussed in Sec. 1.3.

Experiment ($\sqrt{s}$)	Channel	Measurement	Pythia (default) / Λ_b-tune
LEP 91.2 GeV [77, 9]	$f(b \to \Lambda_b)$	$0.101^{+0.039}_{-0.031}$	0.037 / 0.099
LEP 91.2 GeV [8]	$f(b \to \Lambda_b, \Xi_b, \Omega_b)$	0.117 ± 0.021	0.042 / 0.113
Tevatron CDF 1.96 TeV [7]	$\frac{f(b\to\Lambda_b)}{f(b\to B)}$	$0.281^{+0.141}_{-0.103}$	0.043 / 0.124
LHCb 13 TeV [3]	$\frac{f(b\to\Lambda_b)}{f(b\to B)}$	0.259 ± 0.018	0.043 / 0.124

Table 6.1: Comparison between `PYTHIA` simulations using the default value of `probQQtoQ` = 0.081 and the Λ_b-tune value of `probQQtoQ` = 0.24.

The values in the first two rows of Table [6.1] were obtained from e^+e^- collisions at a center-of-mass energy corresponding to the Z boson mass. The decay of the Z boson into a b-quark was then considered, followed by the hadronization of the b-quark into the particles for which the transition fractions were measured. The third value corresponds to a simulation of measurements performed at the Tevatron [7], where proton-antiproton collisions occurred at $\sqrt{s} = 1.96$ TeV. The last value was derived from a proton-proton simulation at $\sqrt{s} = 13$ TeV, aiming to reproduce the measurement performed by the LHCb Collaboration [3].

6.2 `PYTHIA` simulation

The simulation performed consists of proton-proton collisions at $\sqrt{s} = 13.6$ TeV. This value corresponds to the energy collision at the LHC during Run 3.
The code I developed is designed to configure, run and save the simulation of particle collisions, including various adjustable parameters for specific physics processes.

Simulation Parameters

The following settings are applied in the simulation:

- `Beams:idA = 2212`: This parameter specifies the type of particle in beam A, which in this case is set to 2212, the Particle Data Group (PDG) code for a proton.
- `Beams:idB = 2212`: Similarly to `beams: idA`, this sets beam B to also consist of protons.
- `Beams:eCM = 13600`: This parameter defines the energy of the proton-proton collision in the center-of-mass frame. The value is set to 13.6 TeV, which represents the collision energies at the LHC Run 3 and currently the top reachable energy.
- `StringFlav:probQQtoQ = 0.24`: This parameter modifies the flavor dynamics in the string fragmentation model. Specifically, it adjusts the probability for the process in which a quark-antiquark pair is produced from a string, influencing the production of quark flavors during fragmentation.
- `PartonVertex:setVertex = on`: Enabling this option ensures that the vertex positions of partons are set during the event generation. This is important for tracking parton-level interactions before hadronization occurs.

- `Fragmentation:setVertices = on`: This parameter ensures that the fragmentation process, in which partons convert to hadrons, also tracks the spatial vertices of the fragmentation. This provides spatial information about where hadrons are produced in the event.

- `SoftQCD:inelastic = on`: This enables soft QCD inelastic processes, such as low-energy quark-quark interactions, which are crucial for modeling the non-perturbative regime of QCD. These processes dominate total cross sections in proton-proton collisions at the LHC.

- `PartonLevel:FSR = on`: This setting allows Final State Radiation (FSR), where particles emit radiation (e.g., gluons) after a hard scattering event, to be included in the parton-level simulation. FSR is important for simulating the full kinematic range of events.

- `HadronLevel:Hadronize = on`: This parameter enables hadronization, the process in which quarks and gluons (which cannot exist as free particles) transform into hadrons (such as protons, pions, etc.) after the parton-level interaction.

Parallelization

The parallelization in this code has been implemented with the purpose of utilizing the Open Physics Hub cluster at the Department of Physics and Astronomy "A. Righi" of the University of Bologna [57]. The OPH cluster is a high-performance computing (HPC) facility that researchers use to run large-scale simulations and data analysis. It provides multiple computational nodes, each equipped with multiple CPUs and a large amount of memory, allowing users to run simulations in parallel across several cores or nodes, thus reducing the time required for computationally expensive tasks.
In the software employed for this analysis, parallelization is achieved by assigning a unique random seed to each instance of the simulation, which allows independent simulations to run concurrently on different nodes or processors of the OPH cluster. The random seed ensures that each simulation generates a unique set of events, avoiding redundancy between parallel jobs. The following commands are used to set the seed:

- `Random:setSeed = on`: This command activates the use of a random number generator in `PYTHIA 8.3`, necessary for simulating stochastic processes such as particle collisions.

- `std::string seedstr = "Random:seed = "; seedstr += argv[2];`: This line constructs the random seed string by appending the second command-line argument (`argv[2]`), which is passed by the user. This enables different seeds to be assigned to each parallel simulation job.

In the OPH cluster, this configuration allows the execution of multiple simulations in parallel, each with its own seed, ensuring unique and independent event sets across different nodes or CPUs. This approach maximizes computational efficiency and significantly reduces the total run-time required for large simulations, which can involve millions of particle collision events.

Output

The program accepts two command-line arguments:

- The first argument (`argv[1]`) specifies the number of events to simulate, defined as $\mathtt{n}_{events}$.
- The second argument (`argv[2]`) specifies the random seed for the simulation.

The output is stored in a HepMC3 format [36] file, which contains all event data, such as the final-state particles, their momenta, and decay products. This HepMC3 file contains detailed information about the generated events.

Event Generation

The simulation runs for a specified number of events (set by `argv[1]`). During each event, the code checks if specific particles such as $\overline{\Lambda}_b$ baryons (ID = -5122) are produced and if so, the event is saved in the HepMC3 file. Each event is looped through to check the properties of the particles produced in the collision, and specific information about the decay products is processed.

6.2.1 Effect of varying the `probQQtoQ` parameter in the simulation

To investigate the effects related to the variation of the `probQQtoQ` parameter, the proton p_T distribution for the default value of the `probQQtoQ` parameter (orange, indicated as "without tune") is compared to the one obtained with the tuned value (blue, named "with tune") in Fig. 6.1, based on a simulation of pp collisions at $\sqrt{s} = 13.6$ TeV with the parameters set as explained in Sec. 6.2.

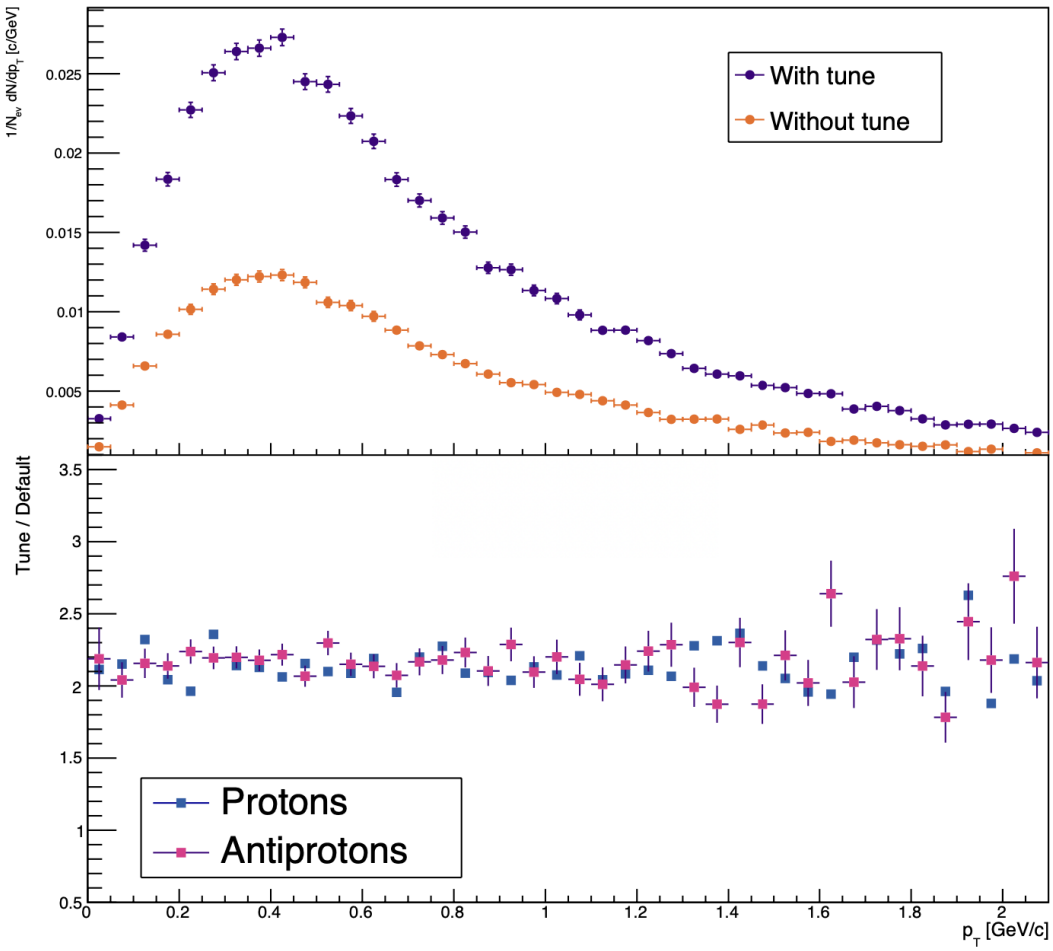

Figure 6.1: Transverse momentum spectra comparison of protons with and without tuning of the `probQQtoQ` parameter. The top plot shows the transverse momentum distributions for protons, comparing the default value of `probQQtoQ = 0.081` and the tuned value of `probQQtoQ = 0.24`. The lower plot presents the ratio of the two configurations for both protons and antiprotons.

In the lower panel of Fig. 6.1, the ratios between the two cases for protons (blue) and antiprotons (pink) show that with the new tune, the number of particles produced is more than double and the effect is the same on particles and antiparticles, as expected.

Another important check to evaluate the reliability of the simulations is to compare the spectra of protons and antiprotons obtained from the simulation with the measured p_T distributions. In this study, the aim is to observe how varying the `probQQtoQ` parameter affects the ability of the simulation to reproduce data. The comparison was performed by simulating pp collisions at $\sqrt{s} = 13$ TeV using the parameters described in Sec. 6.2. This energy value was chosen to compare the simulated proton and antiproton spectra with the ALICE data collected during the LHC Run 2 [18], while the data at $\sqrt{s} = 13.6$ TeV are not available. A rapidity selection is applied corresponding to $|y| < 0.5$ to match the same rapidity interval of the measurement. The uncertainties on the experimental data account both statistical and systematic uncertainties.

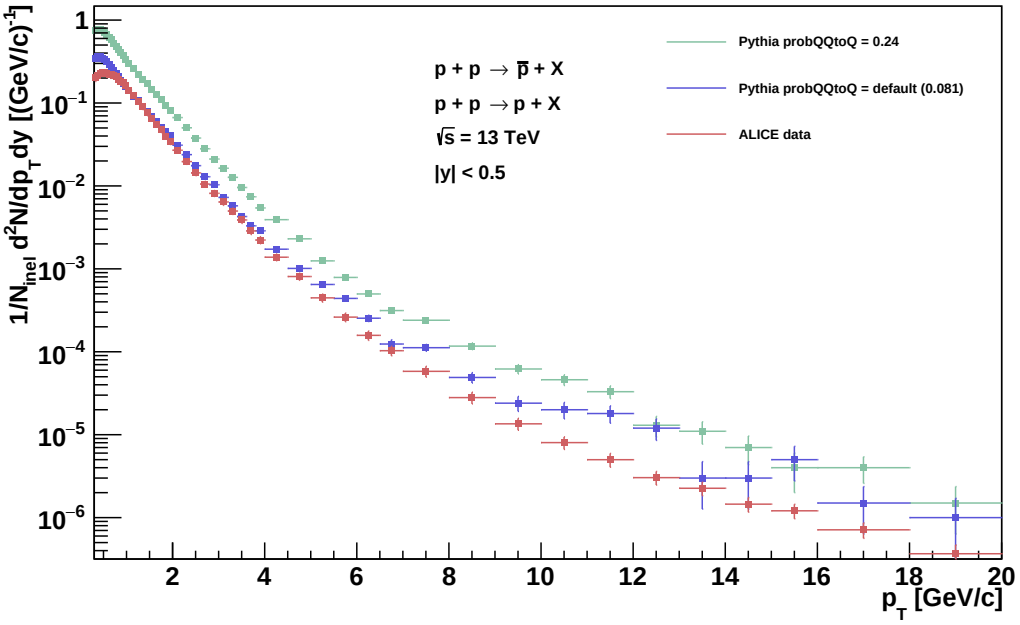

Figure 6.2: Comparison of transverse momentum spectra for protons and antiprotons from simulations and data. The red points correspond to the ALICE experimental data [18], the purple curve represents the simulated data with the default `probQQtoQ` value (0.081), and the green curve corresponds to the simulation with an increased `probQQtoQ` value (0.24). The comparison is performed at a center-of-mass energy of $\sqrt{s} = 13$ TeV and within a rapidity range of $|y| < 0.5$.

Figure 6.2 shows that as the `probQQtoQ` parameter increases, the production of (anti)protons also increases, as expected. In fact, this behavior is one of the critical aspects stressed in [44]. The underlying event, particularly in the context of coalescence, is strongly influenced by this parameter, as it will be explained in the following section. It is important to note that, to derive the spectra, we excluded protons and antiprotons originating from the following weakly decaying particles: Λ, $\Sigma^{\pm}$, Ξ^{0}, $\Xi^{\pm}$, and $\Omega^{\pm}$.

6.2.2 Branching ratios of $\overline{\Lambda}_b$ from `PYTHIA` simulation

In Fig. [6.3] and Fig. [6.4], the branching ratios extracted from the `PYTHIA` simulations are shown for the case in which the value of the `probQQtoQ` parameter is the default one and the tuned version.

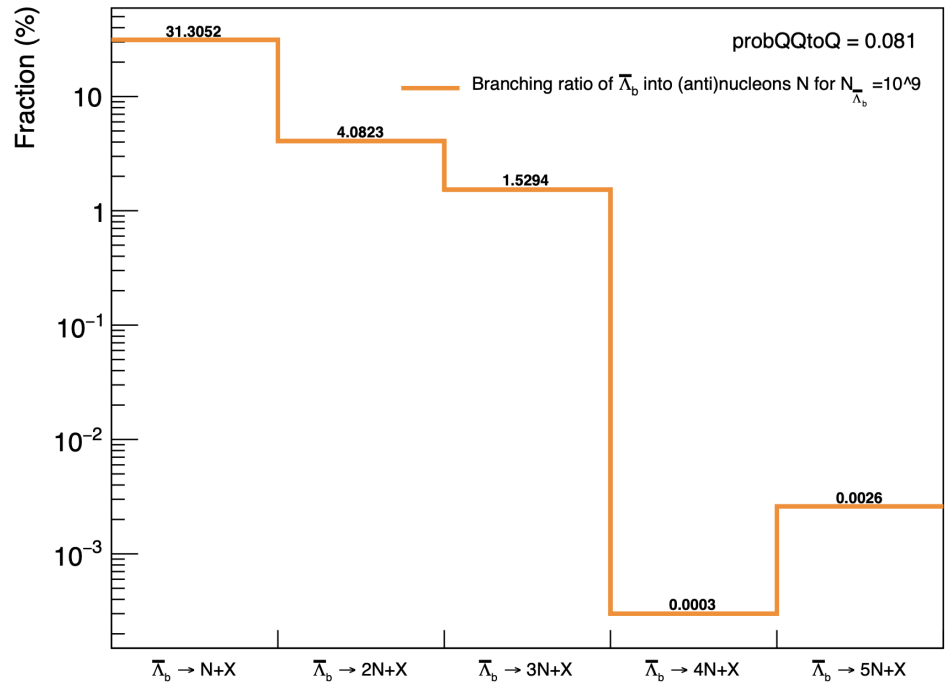

Figure 6.3: Fractions (%) of the $\overline{\Lambda}_b$ decay channels into (anti)nucleons. The case presented is the one where the parameter `probQQtoQ` = 0.081.

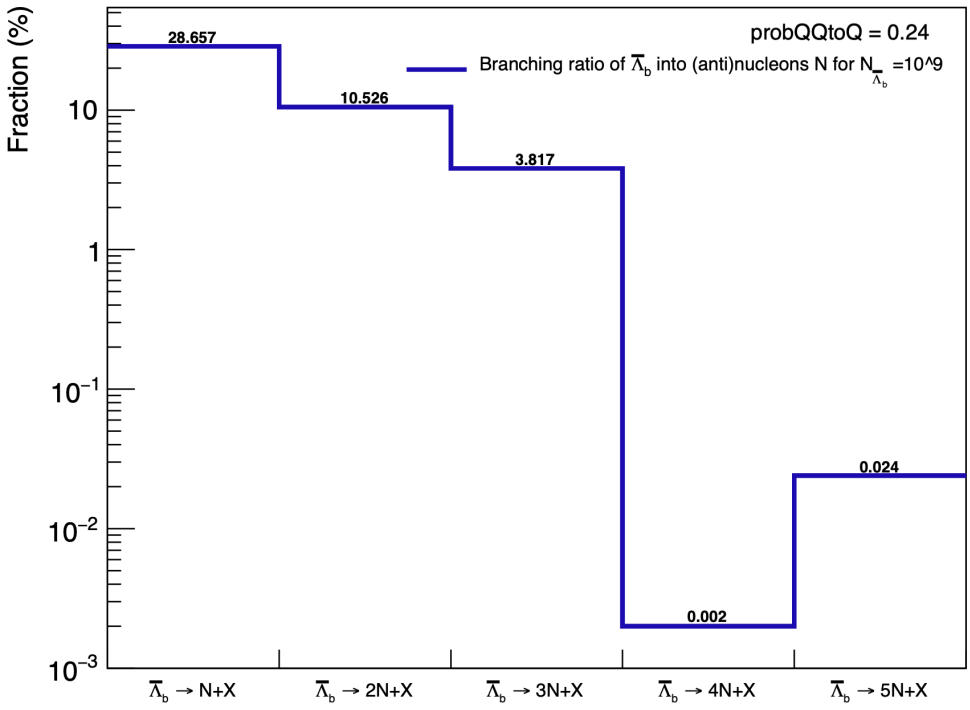

Figure 6.4: Fractions (%) of the $\overline{\Lambda}_b$ decay channels into (anti)nucleons. The case presented is the one where the parameter `probQQtoQ`= 0.24.

For a number of $\overline{\Lambda}_b$ equal to 10^9, the fractions (%) of the decay channels up to 5 (anti)nucleons were extracted. This analysis allows us to understand when the production of (anti)nuclei from $\overline{\Lambda}_b$ could significantly influence the final production of antideuterons. It is also possible to observe that, except for the decay into a single (anti)nucleon, the other channels show higher percentages in the case of the tuned-PYTHIA simulation. Finally, this analysis is also significant in the case where one chooses to study the formation of antinuclei that are heavier than antideuterons, such as antihelium-3.

6.2.3 Antiproton and antineutron spectra at $\sqrt{s} = 13.6$ TeV

The antinucleon spectra produced in the PYTHIA simulation of pp collisions at $\sqrt{s} = 13.6$ TeV are reported in Fig. [6.5] and distinguished in those coming from the decay of $\overline{\Lambda}_b$ and those that are produced in the underlying event (UE). The spectra of antiprotons and antineutrons are not exactly identical in the two cases and that the antinucleons produced by the $\overline{\Lambda}_b$ exhibit a harder spectrum (i.e., shifted towards higher momenta) compared to those from the underlying event.

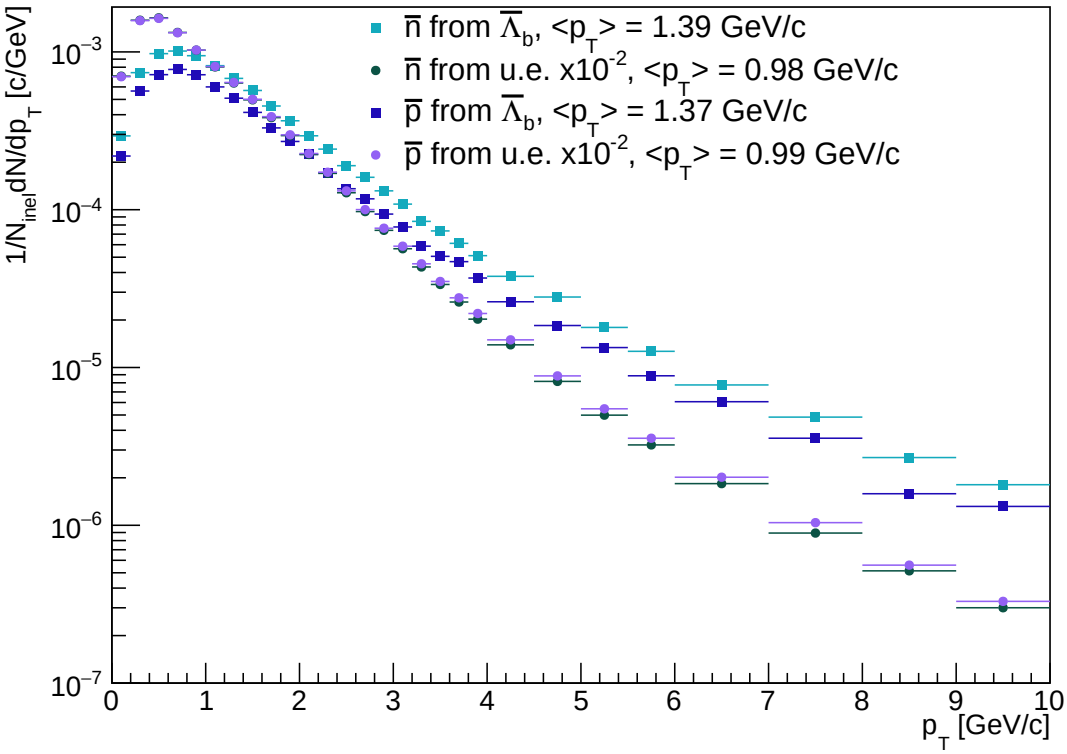

Figure 6.5: Transverse momentum distributions of antinucleons from the decay of the $\overline{\Lambda}_b$ (square markers) and from the underlying event (circles) from simulated pp collisions at $\sqrt{s} = 13.6$ TeV. The average transverse momenta are reported in the legend. In order to compare the spectra from the UE with those from $\overline{\Lambda}_b$, the former have been multiplied by a scaling factor of 10^{-2}.

The study of these spectra is very interesting as these will be the particles involved in the coalescence process for the formation of antideuterons. Another important quantity for the analysis is the ratio between antiprotons and antineutrons produced by $\overline{\Lambda}_b$, as shown in Fig. [6.6]. In the simulation, the $\bar{p}/\bar{n}$ ratio is below unity.

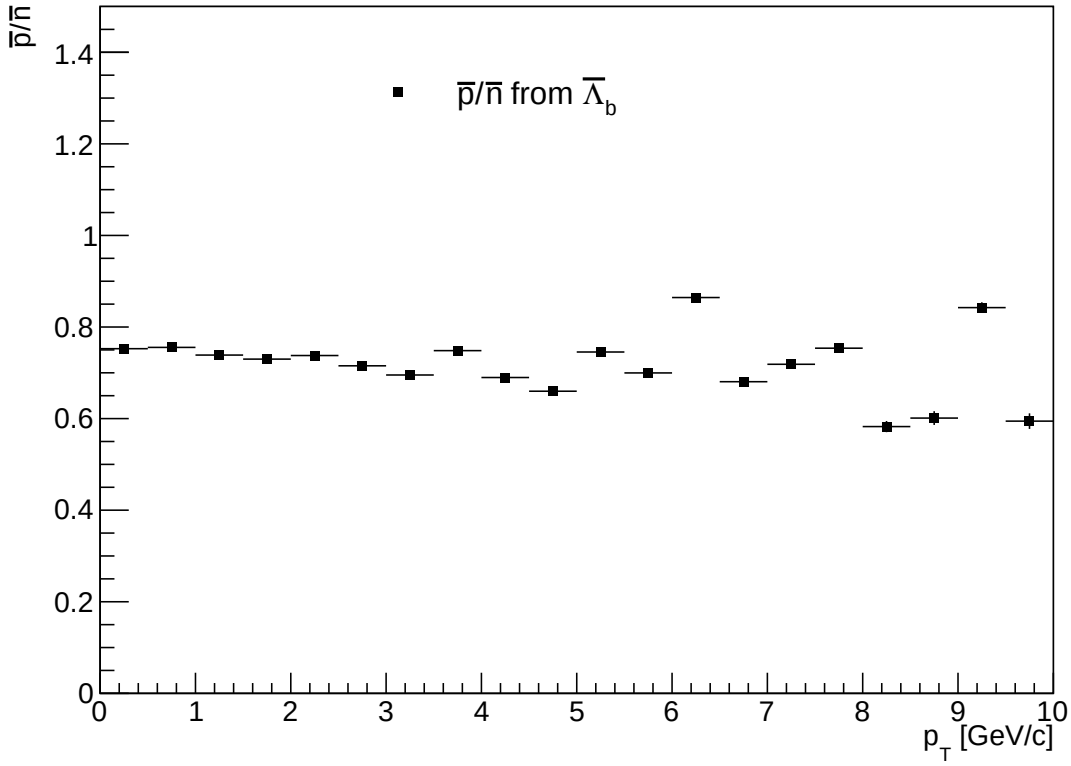

Figure 6.6: Ratio between the number of antiprotons and the number of antineutrons produced as a function of the transverse momentum p_T.

This result does not significantly affect the production of antideuterons studied in this dissertation, but it could provide new interesting insights into the effects this may have on the production of heavier antinuclei. For instance, this estimate could suggest that the decays of the $\overline{\Lambda}_b$ might slightly favor the production of antinuclei containing more antineutrons than antiprotons.

6.3 Implementation of the coalescence afterburner

The production of antideuterons in high-energy collision events is simulated through two different implementations of the coalescence model that are applied in cascade to the tuned `PYTHIA 8.3` simulation by means of a so-called *afterburner*. The afterburner is applied to antiprotons and antineutrons to determine whether they satisfy the criteria for coalescence to form antideuterons. Two different implementations of coalescence, a classic approach, summarised by Eq. 2.1, and a quantum-mechanical approach, described in Sec. 2.4, are employed.

The goal of this whole approach is to study the formation of light antinuclei in the context of different production processes, such as the decay of $\overline{\Lambda}_b$ baryons or the underlying event. Therefore, three cases are distinguished:

- **Antinucleons from $\overline{\Lambda}_b$ decay**: In this scenario, both the antiproton and antineutron originate from the decay of a $\overline{\Lambda}_b$ baryon. Since they are produced in close proximity in space and time, causality is inherently preserved and the particles can readily coalesce.

- **Antinucleons from the Underlying Event**: The UE consists of secondary

parton-parton interactions that occur along with the primary collision, producing additional particles that are not directly involved in the hard scattering process.

- **Mixed Scenario**: This scenario involves one antinucleon from $\overline{\Lambda}_b$ decay and the other from the UE. In this case, causality is explicitly checked to ensure that the particles could have interacted before forming an antideuteron.

6.3.1 Coalescence model - Classical approach

I implemented this simulation considering the coalescence process driven by the principle that antiprotons and antineutrons can form a bound state (such as an antideuteron) if their relative momentum is below a certain threshold, defined as the coalescence momentum $p_c/2$. This threshold represents the maximum relative momentum for which two particles can form a bound system (see Eq. 2.1).
The coalescence condition is verified in the center of mass system (CMS) of a pair of antinucleons. To do this, the momenta of the antiproton and antineutron are boosted from the laboratory frame to the center-of-mass frame of their total momentum. In this frame, if the relative momentum between the particles is below $p_c/2$, coalescence occurs, and the two particles are treated as a single antideuteron. In this code, the default value for $p_c/2$ is set to 0.219 GeV/c according to [74] for two-body coalescence.

Lorentz Transformations

The core of the coalescence mechanism involves transforming the momenta of the antinucleons from the laboratory frame to the center of mass of the pair of particles. The code uses the `TLorentzVector` class from ROOT to handle the 4-momenta of particles. For each event, the momentum vectors of the particles are first summed to obtain the total momentum of the pair, and then the boost vector (β) is calculated. After the boost, the relative momenta of the particles are checked against the coalescence condition. This transformation ensures that the coalescence condition is evaluated in the appropriate reference frame where the relative motion of the particles is minimized.

Causality in Coalescence

Causality is a crucial condition that I applied in the case of "mixed coalescence", where one antinucleon originates from the decay of a $\overline{\Lambda}_b$ baryon, while the other comes from the underlying event. Since these particles are produced in different regions of space and time, the code implements a causality check to ensure that the two particles could physically interact.
The causality condition consists in calculating the distance between the production vertices of the two particles and comparing it with the time difference between their production. Specifically, the velocity of the first particle is used to propagate its position forward in time until the second particle is produced. The distance traveled by the first particle is compared with the spatial separation between the two production points. If the first particle could have reached the production point of the second particle within the allowed time, causality is preserved, and coalescence

is allowed. The propagation of the first particle's position is computed using the formula:

$$x_{\text{new}} = x_{\text{initial}} + v_x \cdot \Delta t, \quad y_{\text{new}} = y_{\text{initial}} + v_y \cdot \Delta t, \quad z_{\text{new}} = z_{\text{initial}} + v_z \cdot \Delta t \quad (6.1)$$

where v_x, v_y, v_z are the velocity components of the first particle, and Δt is the time difference between the two production events. The distance between these particles is then calculated and if the spatial separation is less than 1 fm (the approximate size of a proton), causality is considered valid and coalescence is allowed to proceed.

6.3.2 Coalescence model - Quantum-mechanical approach

The coalescence mechanism modeled in this algorithm follows quantum-mechanical principles, taking into account both spatial and momentum correlations between nucleon pairs. Unlike classical coalescence models, this algorithm incorporates a more sophisticated quantum-mechanical framework. The spatial distance between the proton and neutron in their rest frame is calculated using Lorentz transformations. This distance is then compared with the size of the deuteron wave function, and a probability function is used to decide if coalescence occurs.
The key difference between this model and the simpler coalescence model is the use of wave functions to describe the relative motion of the nucleons. Specifically, nuclear wave functions such as the Hultén [64] and Argonne v_{18} [76] wave functions can be employed, which offer a more accurate representation of the bound state structure of (anti)deuterons. The quantum mechanical coalescence condition is enforced by using a function that calculates the overlap probability between the proton and neutron wave functions. The implementation of the wave functions as well as of the afterburner with the quantum-mechanical approach follows the treatment in [51].

Addition of the $\overline{\Lambda}_b$ decay

A significant modification made to this algorithm is the inclusion of the nucleons originating from $\overline{\Lambda}_b$ decay. The $\overline{\Lambda}_b$ decays into antiprotons and antineutrons, which are then considered candidates for antideuteron coalescence. Antiprotons and antineutrons originating from $\overline{\Lambda}_b$ decays are categorized separately from those produced in other processes, allowing us to study the contribution of heavy baryon decays to antideuteron production.
The logic for identifying antinucleons from $\overline{\Lambda}_b$ decays is implemented in the following way:

- Antiprotons and antineutrons produced from $\overline{\Lambda}_b$ decays are added to specific lists.
- Antiprotons and antineutrons produced through intermediate particles such as Δ^+, Δ^0, and Λ_c are handled separately to ensure that the decay chain is properly traced.
- The algorithm distinguishes between primordial antiprotons/antineutrons and those produced via heavy-flavor baryon decays, allowing us to track different production mechanisms.

Lorentz Transformations and Coalescence in the Pair Rest Frame

The coalescence process requires the transformation of the momenta and positions of the proton and neutron to their pair rest frames. This transformation is done using Lorentz boosts, which account for the motion of the center-of-mass of the nucleon pair. Once in the rest frame, the relative distance between the proton and neutron is calculated. The wave function overlap condition is then applied to determine if coalescence occurs.

Antideuteron Wave Function and Source Size

Several possible choices for the (anti)deuteron wave function are available to control the probability of coalescence, also used in literature, e.g. in [51]. These include:

- `SingleGaus`: a simple Gaussian probability distribution.
- `DoubleGausR` and `DoubleGausPhi`: Gaussian distributions for the radial and angular components, respectively.
- `Hultén` and `Argonne`: more realistic wave functions that represent the binding potential of (anti)deuterons. In particular, the `Hultén` wave function is derived from the Yukawa theory of strong interaction [64], whereas the `Argonne` v_{18} function is based on a phenomenological potential constrained to proton-neutron scattering experiment data [76].

The source size, which is a critical parameter for coalescence, can be dynamically set on the basis of experimental data (e.g. the ALICE measurement in pp collisions at $\sqrt{s} = 13$ TeV [15]) or fixed to a given value. The source size defines the spatial extent of the nucleon-nucleon wave function overlap, and it plays a key role in determining the coalescence probability.

Particle Classification

The particles are classified as follows:

- **Primordial Protons/Antiprotons and Neutrons/Antineutrons**: These (anti)nucleons are directly produced in the initial collision without any intermediate particle decays.
- **Feed-down Protons/Antiprotons and Neutrons/Antineutrons**: These (anti)nucleons are produced from the decays of particles such as Δ baryons and $\overline{\Lambda}_b$. The algorith tracks their origins to ensure proper handling of decay chains.

In addition to the implementation of the coalescence afterburner, a second post-analysis was developed to analyze the results stored in the output HepMC3 files. The analysis further distinguishes between the three specific production scenarios according to the provenance of the antinucleons, as described above.

6.3.3 Antideuteron spectra

The rapidity distributions of antideuterons obtained using both classical and quantum-mechanical coalescence methods are reported in Fig. [6.7]. The rapidity distribution does not allow us to significantly distinguish the production of antideuterons from $\overline{\Lambda}_b$ or from the underlying event. As expected, the production is maximal at mid-rapidity, where it presents a plateau.

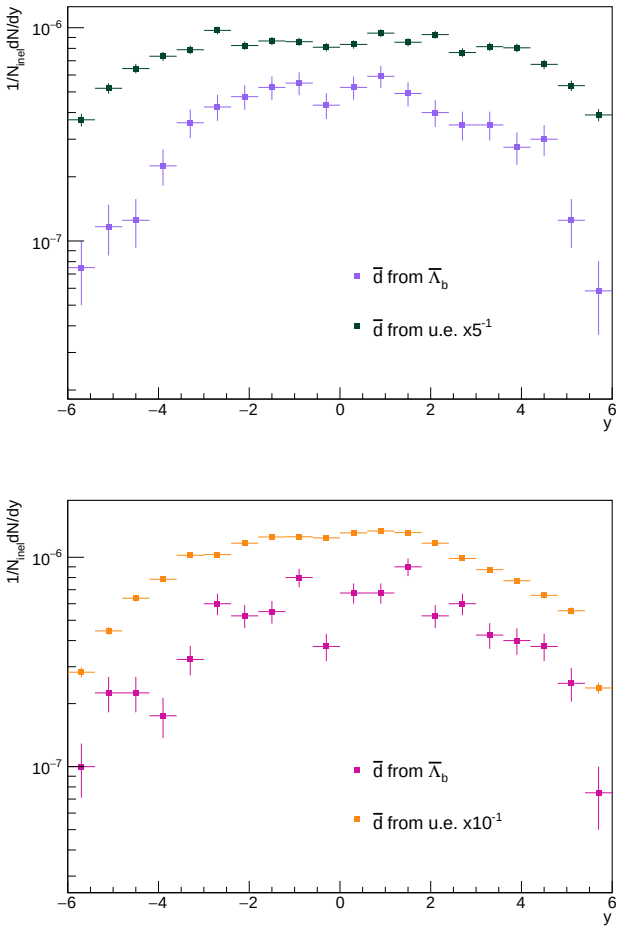

Figure 6.7: Rapidity spectra of antideuterons from the decay of $\overline{\Lambda}_b$ and the underlying event. The top panel shows the spectrum obtained using the classical coalescence method, while the bottom panel shows the spectrum obtained with the quantum-mechanical coalescence method. Two different scaling factors have been applied to allow for a comparison of the spectra from $\overline{\Lambda}_b$ and the underlying event.

In Fig. [6.8], the transverse momentum spectra of antideuterons produced using the two coalescence methods are shown. From these we can observe that the p_T distribution is different for antideuterons that come from $\overline{\Lambda}_b$ compared to those from the underlying event. The spectrum for antideuterons from $\overline{\Lambda}_b$ shows a more pronounced peak at lower p_T. This allows us to achieve a distinction that we were previously unable to obtain by looking at the rapidity distribution.

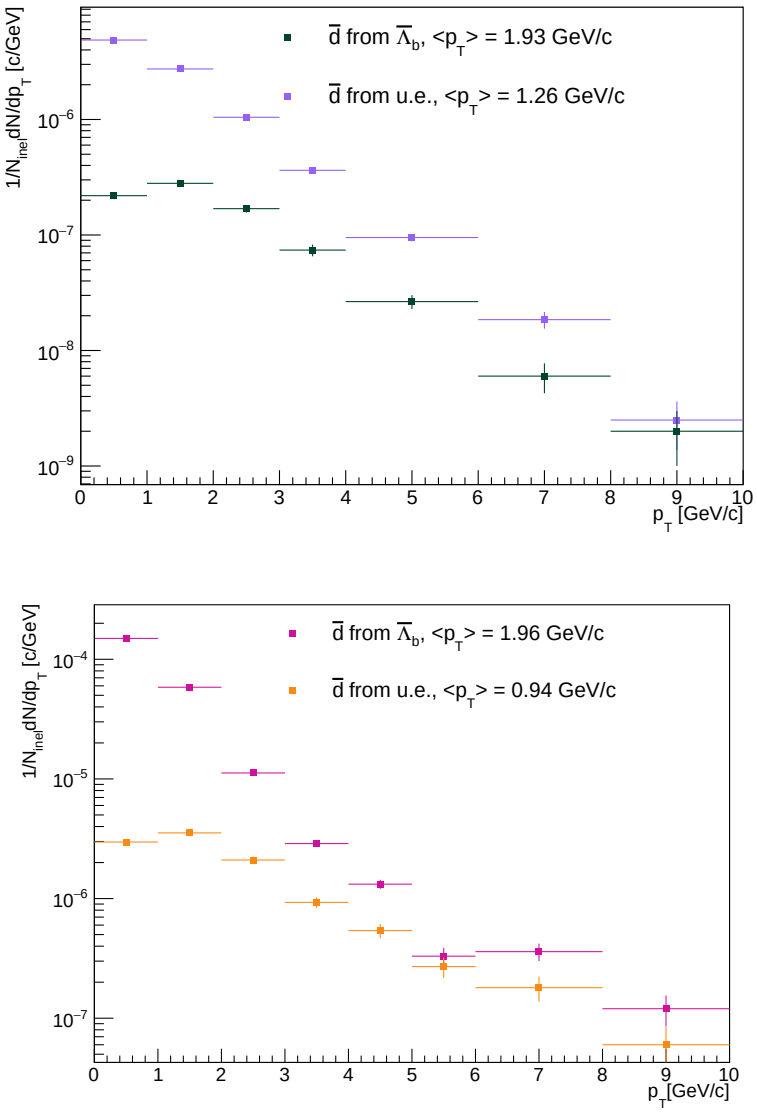

Figure 6.8: Transverse momentum spectra of antideuterons from the decay of $\overline{\Lambda}_b$ and the underlying event. The top plot shows the spectrum obtained using the classical coalescence method, while the bottom plot shows the spectrum obtained with the quantum-mechanical coalescence method. The average transverse momenta of each spectrum are also shown in the legend.

From Fig. [6.8] we can see that the antideuterons spectra coming from $\overline{\Lambda}_b$ exhibit a harder distribution with an average momentum twice as high as that of the UE case.

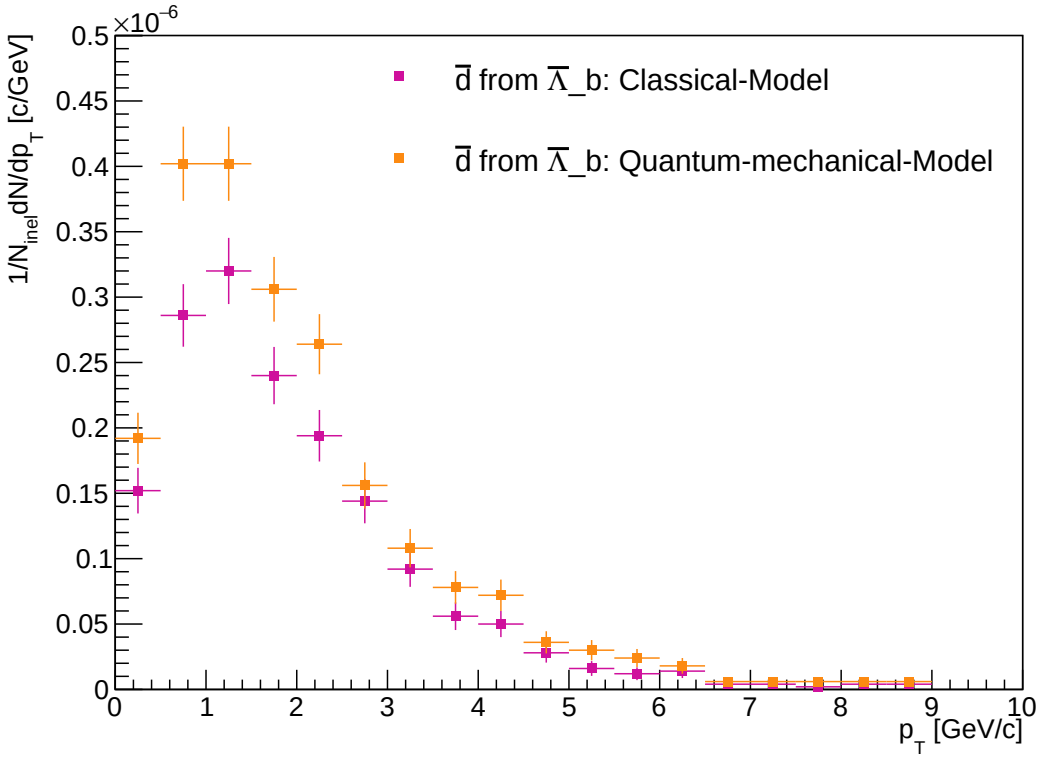

Figure 6.9: Transverse momentum spectra of antideuterons from the decay of $\overline{\Lambda}_b$ with the two coalescence models compared. At low p_T we can observe a higher production of antideuterons from the quantum-mechanical model.

In Fig. [6.9] a comparison between the antideuterons spectra produced from $\overline{\Lambda}_b$ is shown for the two models. We can see both that the production of antideuterons is greater and the average transverse momentum is larger for the quantum-mechanical model.

6.4 Determination of the branching ratio

The goal of the study is to determine the overall branching ratio of $\overline{\Lambda}_b \rightarrow \overline{d} + X$ to perform a first prediction of its value and to identify possible regions of interest for experimental measurement.

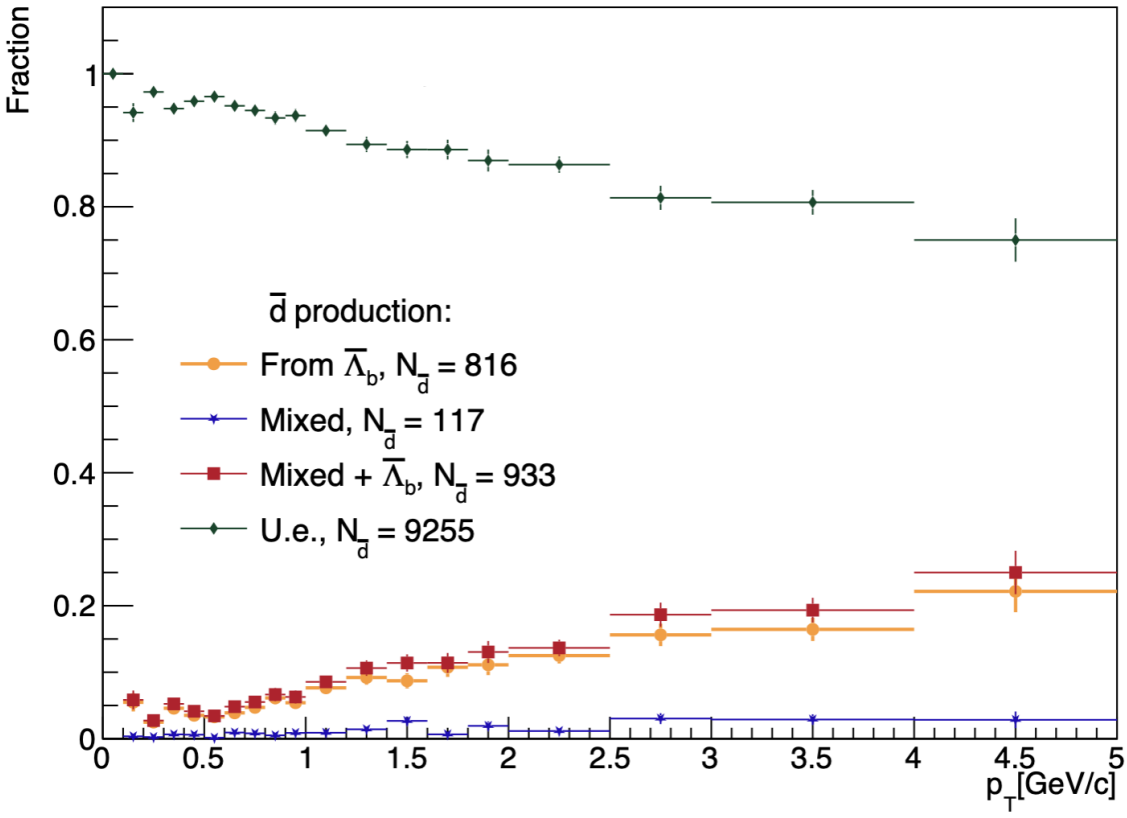

Figure 6.10: Fraction of antideuteron production as a function of transverse momentum obtained using the classical coalescence approach. . The orange points represent antideuterons produced from $\overline{\Lambda}_b$ decays, the blue stars represent the mixed contribution, and the red squares correspond to the total production from both mixed and $\overline{\Lambda}_b$ sources. The green diamonds represent the contribution from the underlying event (UE). The total number of antideuterons ($N_{\bar{d}}$) produced in each scenario is indicated in the legend.

The results of the analysis carried out by simulating the antinucleons with the tuned `PYTHIA` and applying the coalescence afterburner based on the classical method introduced in section 7.3 are shown in Fig. [6.10]. Finally, the branching ratio extracted as the ratio of antideuterons produced to the total number of $\overline{\Lambda}_b$ is:

$$\mathrm{BR}(\overline{\Lambda_b} \to \overline{d} + X) = (7.3 \pm 0.3) \times 10^{-4} \tag{6.2}$$

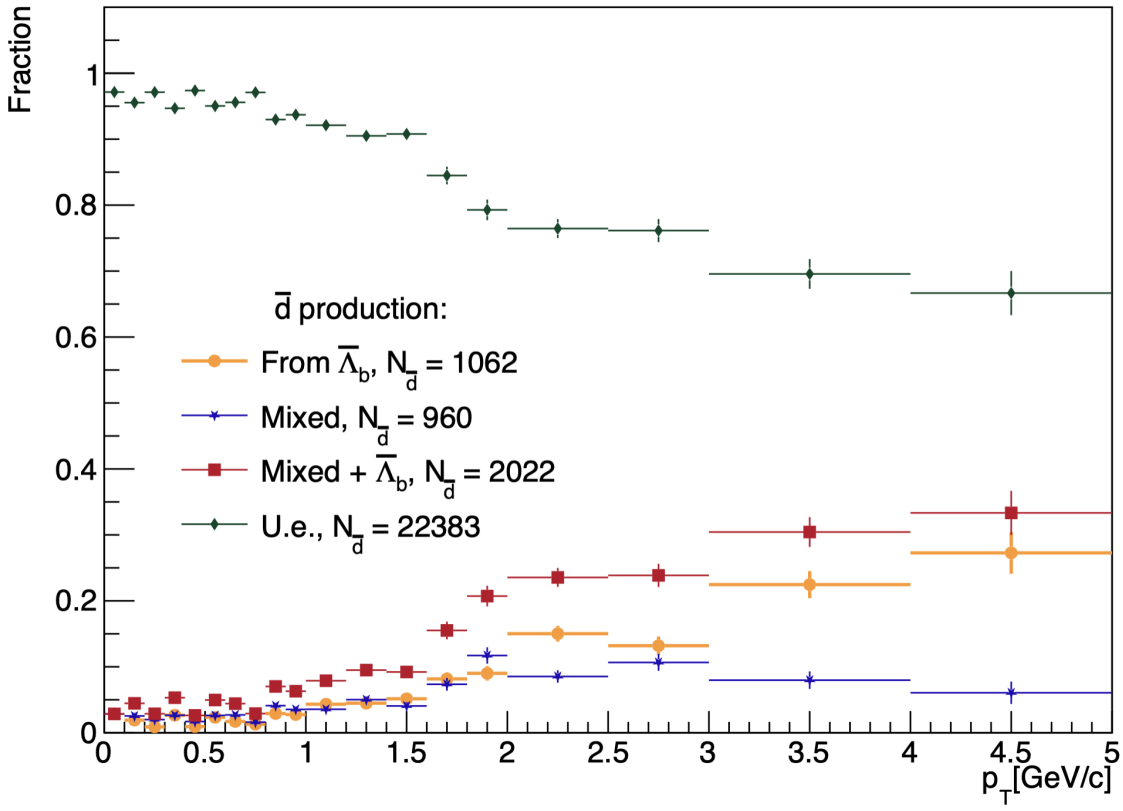

Figure 6.11: Fraction of antideuteron production as a function of transverse momentum p_T, obtained using the quantum mechanical coalescence approach. The orange points represent antideuterons produced from $\overline{\Lambda}_b$ decays, the blue stars represent the mixed contribution, and the red squares correspond to the total production from both mixed and $\overline{\Lambda}_b$ sources. The green diamonds represent the contribution from the underlying event (UE). The total number of antideuterons ($N_{\bar{d}}$) produced in each scenario is indicated in the legend.

The Fig. [6.11] shows the result of the coalescence afterburner based on the quantum mechanical approach introduced in Sec.6.3.2 using a Gaussian wavefunction. The branching ratio extracted as the ratio of antideuterons produced to the total number of $\overline{\Lambda}_b$ is:

$$\mathrm{BR}(\overline{\Lambda_b} \to \overline{d} + X) = (9.5 \pm 0.3) \times 10^{-4} \tag{6.3}$$

The two branching ratio values of Eqs. 6.2 and 6.3 have been extracted for the first time through the analysis conducted in this thesis. In the literature, there are currently no references to possible branching ratio values related to this particular decay channel.

	C-model	QM-model
Branching Ratio	$(7.3 \pm 0.3) \times 10^{-4}$	$(9.5 \pm 0.3) \times 10^{-4}$

Table 6.2: Branching ratios table. C-model is referred to the classical model, QM-model is referred to the quantum-mechanical model. The values extracted with the two different models are reported in this table to make the comparison easier.

The ratio between the two is of the order of 30%, with more antideuterons produced in the case of the QM-model. However, we should give more weight to

the value extracted with the quantum-model because it is based on a more precise evaluation, as explained in Chapter 2. For the purpose of the estimates of the branching ratio, the discrepancy between the two measurements can be taken as a confidence interval. It is important to note that the difference is also p_T dependent, as can be seen from Fig. [6.11] and Fig. [6.10], while at low p_T (below 1 GeV/c) the fraction of antideuterons from $\overline{\Lambda}_b$ is similar for the two models, at higher p_T the QM-model gives a higher fraction of antideuterons. In addition, different choices of the wave function for the quantum-mechanical approach may introduce differences in the final prediction and may be subject for further dedicated study.

6.5 Antideuterons from $\overline{\Lambda}_b$ decay in ALICE and LHCb

In this work, we explore the feasibility of observing antideuterons produced in the decay channel $\overline{\Lambda}_b \to \overline{d} + X$ in the LHCb and ALICE detectors. The main objective is to analyze the pseudorapidity and transverse (total) momentum distributions of the produced antideuterons and to evaluate the capability of these two experiments to detect them. Each experiment covers different kinematic regions, offering complementary insights into the process.
ALICE operates in the pseudorapidity range $-0.8 < \eta < 0.8$, covering the mid-rapidity region. The key subdetectors involved in the tracking and identification of antideuterons in ALICE are the Inner Tracking System (ITS), the Time Projection Chamber (TPC) and the Time-Of-Flight (TOF) detector.
In contrast, LHCb operates in the forward pseudorapidity region $2 < \eta < 5$ using RICH detectors to perform antinuclei detection.
The Fig. [6.12] reports the pseudorapidity distribution for the antideuterons on the x-axis and the pseudorapidity distribution for the $\overline{\Lambda}_b$ produced in the process on the y-axis. The plot refers to $N_{ev} = 10^9$ simulated pp collision at $\sqrt{s} = 13.6$ TeV. The number of produced $\overline{\Lambda}_b$ and $\overline{d}$ are reported in Table [6.3].

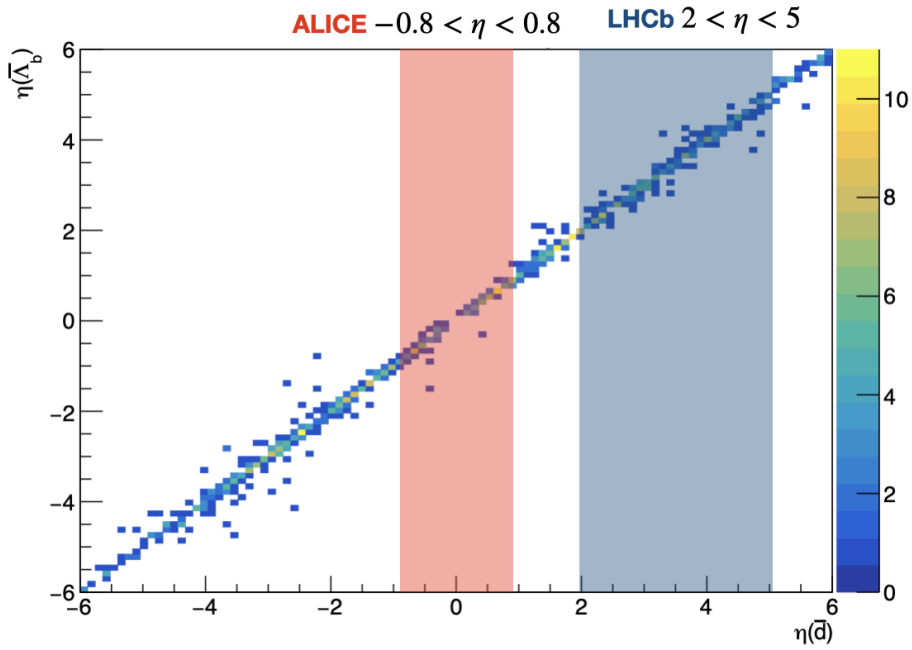

Figure 6.12: Comparison of pseudorapidity and transverse momentum distributions for antideuterons in ALICE and LHCb. ALICE is shown in red, covering mid-rapidity $-0.8 < \eta < 0.8$, while LHCb is shown in blue, covering forward rapidity $2 < \eta < 5$.

	LHCb $2 < \eta < 5$	**ALICE** $-0.8 < \eta < 0.8$
$N(\overline{\Lambda}_b)$	250071	243144
$N(\overline{d})$	204	92

Table 6.3: Comparison between LHCb and ALICE. $N(\overline{\Lambda}_b)$ corresponds to the number of $\overline{\Lambda}_b$ that each detector could detect in the process. The same is valid for $N(\overline{d})$.

From this first analysis, we can see that at LHCb, the production of antideuterons per number of $\overline{\Lambda}_b$ is greater than in ALICE by a factor of two.
The next step is to look at the antideuteron transverse momentum spectrum for ALICE and the antideuteron total momentum spectrum for LHCb.
The reason why we look at different spectra is due to their different configurations, as the former is a mid-rapidity detector, while the latter is a forward-rapidity detector. Antideuteron identification in LHCb is based on the RICH1 and RICH2 detectors, with momentum thresholds above 35.4 GeV/c and 59.3 GeV/c, respectively. ALICE can track particles with p > 0.150 GeV/c and identify (anti)deuterons in the range $0.7 < p_T < 5$ GeV/c.

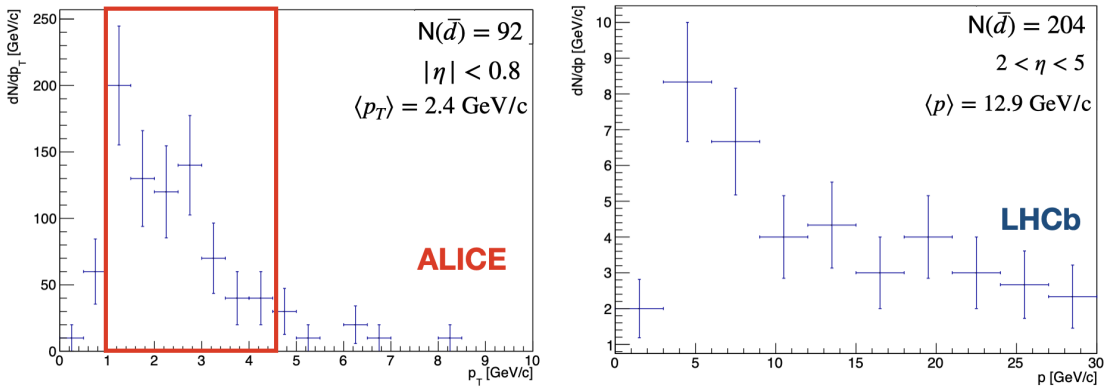

Figure 6.13: Left: Antideuteron spectrum in terms of transverse momentum. The red square represents the kinematical region explored by the ALICE detector. Right: Antideuteron spectrum in terms of total momentum. With its subdetector, LHCb is not able to explore the region of the antideuteron production from the $\overline{\Lambda}_b$ decay.

Because of these high thresholds, LHCb is sensitive to high-momentum antideuterons. Since the mean momentum of the distribution is around $\langle p \rangle = 12.9\,\text{GeV/c}$, this detector is not able to explore the region of our interest at low p_T. On the contrary, ALICE is able to detect antideuterons produced from $\overline{\Lambda}_b$ decays since the mean transverse momentum of the distribution is $\langle p_T \rangle = 2.4\,\text{GeV/c}$.

In conclusion, through this analysis, it was possible to determine that, in the current state, only the ALICE detector is potentially capable of detecting the antideuterons signal produced from the decay of $\overline{\Lambda}_b$. The strength of the study conducted in this section lies in the fact that, by analyzing antideuteron spectra, it was possible to exclude the possibility that LHCb is capable of performing studies related to antideuteron production from $\overline{\Lambda}_b$, without the need for a full detector simulation. The LHCb collaboration is currently working on a new reconstruction technique, known as `TRACKBETATOOL` [50], with the goals of extracting the velocity of the candidates performing the PID combining it with the reconstructed momentum and extending the explored momentum range at values of $p < 10$ GeV/c. If successful for the application to (anti)deuteron, such a technique might open the possibility for a measurement of the $\overline{\Lambda}_b$ decay into antideuterons, providing complementary information (in the forward rapidity region) with respect to a measurement by ALICE.

Conclusion

The aim of this thesis work was to analyze the features of a new possible decay channel of the heavy baryon $\overline{\Lambda}_b$ into antideuterons at the LHC. For this purpose, the Monte Carlo-based software `PYTHIA` version 8.3 was used. A custom code was developed to simulate pp collisions at $\sqrt{s} = 13.6$ TeV. The parameter `probQQtoQ` was adjusted to enhance baryon production over meson production and to match LEP data for Λ_b. As discussed in Chapter 4, the current predictions from `PYTHIA` for the baryon-to-meson ratio do not perfectly match the experimental data, making this aspect particularly interesting to investigate. By modifying the parameter, the production of protons and antiprotons was found to have doubled compared to simulations with default settings and to overestimate the transverse momentum spectra of protons and antiprotons as measured with ALICE in pp collisions at $\sqrt{s} = 13$ TeV. Next, we extracted the branching ratios for the production of nucleons and antinucleons from $\overline{\Lambda}_b$, which allowed us to assess the impact of this particle on antinuclei production. The analysis was performed by calculating the branching ratios for up to five (anti)nucleons in the final state, beyond which mass conservation would no longer hold. The transverse momentum spectra of antinucleons were then extracted from simulated pp collisions at $\sqrt{s} = 13.6$ TeV, comparing cases where they are produced by $\overline{\Lambda}_b$ and from the underlying event. In particular, the ratio between antiprotons and antineutrons produced by $\overline{\Lambda}_b$ was studied. Since this ratio is below unity, it suggests that, when considering the formation of heavier antinuclei than antideuterons, $\overline{\Lambda}_b$ could contribute more significantly to the formation of antinuclei with a greater number of antineutrons than antiprotons. At this stage, after obtaining the $\overline{\Lambda}_b$ particles, two coalescence methods were used to study the production of antideuterons from the antinucleons produced by the decay of $\overline{\Lambda}_b$. This allowed us, in both cases, to do a first estimation of the branching ratio for the decay of $\overline{\Lambda}_b$ into antideuterons based on simulations, a result not yet reported in the literature. Additionally, we obtained the rapidity and transverse momentum spectra of antideuterons. From these results, we concluded that antideuterons from $\overline{\Lambda}_b$ and those from the underlying event exhibit the same behavior in terms of rapidity, while the transverse momentum spectra of antideuterons from $\overline{\Lambda}_b$ are sharper, with a more pronounced peak at low p_T. Finally, a comparison was performed between the ALICE and LHCb detectors at the LHC, which explore complementary regions of pseudorapidity. It was found that, although the production of $\overline{\Lambda}_b$ and antideuterons is higher in the LHCb pseudorapidity acceptance (forward rapidity) compared to the ALICE one (midrapidity), the momentum spectra of antideuterons showed that LHCb's current subdetectors are not capable of detecting antideuterons from $\overline{\Lambda}_b$. However, the transverse momentum spectra indicated that, for ALICE, these particles fall within the detector range, making their detection and indentification feasible. The work presented here could be expanded by performing a full

simulation of the ALICE detector to evaluate the feasibility of measuring or observing this decay channel. A natural continuation of this work would be to analyze the data collected by ALICE during Run 3 based on the findings of this thesis.

The significance of this analysis is evident not only in its implications for antinuclei production at accelerators but also for its potential contribution to the indirect detection of dark matter through the production of antinuclei, a topic of current interest. Moreover, the inclusion of the $\overline{\Lambda}_b$ baryon adds further relevance to this study, as it offers the opportunity to explore aspects of b-quark physics that remain unresolved. This research contributes also to the ERC-funded CosmicAntiNuclei project, which aims to validate coalescence models and improve the predictions for signal and background rates of light antinuclei originating from dark matter interactions. The ultimate goal is to improve our understanding of the mechanisms involved in their formation.

Bibliography

[1] R. Aaij et al. Study of the production of Λ_b^0 and $\overline{B}^0$ hadrons in pp collisions and first measurement of the $\Lambda_b^0 \to J/\psi p K^-$ branching fraction. *Chin. Phys. C*, 40(1):011001, 2016.

[2] Roel Aaij et al. LHCb Detector Performance. *Int. J. Mod. Phys. A*, 30(07):1530022, 2015.

[3] Roel Aaij et al. Measurement of b hadron fractions in 13 TeV pp collisions. *Phys. Rev. D*, 100(3):031102, 2019.

[4] Roel Aaij et al. Measurement of the $\Lambda b0 \to \Lambda(1520)\mu+\mu-$ Differential Branching Fraction. *Phys. Rev. Lett.*, 131(15):151801, 2023.

[5] Roel Aaij et al. Enhanced Production of $\Lambda b0$ Baryons in High-Multiplicity pp Collisions at s=13 TeV. *Phys. Rev. Lett.*, 132(8):081901, 2024.

[6] Roel Aaij et al. The LHCb Upgrade I. *JINST*, 19(05):P05065, 2024.

[7] T. Aaltonen et al. Measurement of Ratios of Fragmentation Fractions for Bottom Hadrons in $p\bar{p}$ Collisions at $\sqrt{s} = 1.96$-TeV. *Phys. Rev. D*, 77:072003, 2008.

[8] D. Abbaneo et al. Combined results on b hadron production rates and decay properties. 6 2001.

[9] G. Abbiendi et al. A Measurement of the product branching ratio f(b —> Lambda(b)) x BR(Lambda(b) —> Lambda X) in Z0 decays. *Eur. Phys. J. C*, 9:1–9, 1999.

[10] K. Abe et al. The results from BESS-Polar experiment. *Adv. Space Res.*, 60:806–814, 2017.

[11] Shreyasi Acharya, Jaroslav Adam, Dagmar Adamová, Jonatan Adolfsson, Madan Mohan Aggarwal, Gianluca Aglieri Rinella, Michelangelo Agnello, Neelima Agrawal, Zubayer Ahammed, Nazeer Ahmad, et al. Production of deuterons, tritons, he 3 nuclei, and their antinuclei in pp collisions at s= 0.9, 2.76, and 7 tev. *Physical review C*, 97(2):024615, 2018.

[12] Shreyasi Acharya et al. Production of deuterons, tritons, ^{3}He nuclei and their antinuclei in pp collisions at $\sqrt{s} = 0.9$, 2.76 and 7 TeV. *Phys. Rev. C*, 97(2):024615, 2018.

[13] Shreyasi Acharya et al. Charged-particle production as a function of multiplicity and transverse spherocity in pp collisions at $\sqrt{s} = 5.02$ and 13 TeV. *Eur. Phys. J. C*, 79(10):857, 2019.

[14] Shreyasi Acharya et al. Multiplicity dependence of π, K, and p production in pp collisions at $\sqrt{s} = 13$ TeV. *Eur. Phys. J. C*, 80(8):693, 2020.

[15] Shreyasi Acharya et al. Search for a common baryon source in high-multiplicity pp collisions at the LHC. *Phys. Lett. B*, 811:135849, 2020.

[16] Shreyasi Acharya et al. Measurement of beauty and charm production in pp collisions at $\sqrt{s} = 5.02$ TeV via non-prompt and prompt D mesons. *JHEP*, 05:220, 2021.

[17] Shreyasi Acharya et al. Production of light-flavor hadrons in pp collisions at $\sqrt{s} = 7$ and $\sqrt{s} = 13$ TeV. *Eur. Phys. J. C*, 81(3):256, 2021.

[18] Shreyasi Acharya et al. Production of light-flavor hadrons in pp collisions at $\sqrt{s} = 7$ and $\sqrt{s} = 13$ TeV. *Eur. Phys. J. C*, 81(3):256, 2021.

[19] Shreyasi Acharya et al. Study of flavor dependence of the baryon-to-meson ratio in proton-proton collisions at s=13 TeV. *Phys. Rev. D*, 108(11):112003, 2023.

[20] Shreyasi Acharya et al. ALICE upgrades during the LHC Long Shutdown 2. *JINST*, 19(05):P05062, 2024.

[21] Jaroslav Adam et al. Pseudorapidity and transverse-momentum distributions of charged particles in proton–proton collisions at $\sqrt{s} = 13$ TeV. *Phys. Lett. B*, 753:319–329, 2016.

[22] O. Adriani et al. PAMELA results on the cosmic-ray antiproton flux from 60 MeV to 180 GeV in kinetic energy. *Phys. Rev. Lett.*, 105:121101, 2010.

[23] M. Aguilar et al. The Alpha Magnetic Spectrometer (AMS) on the International Space Station. I: Results from the test flight on the space shuttle. *Phys. Rept.*, 366:331–405, 2002. [Erratum: Phys.Rept. 380, 97–98 (2003)].

[24] M. Aguilar et al. Antiproton flux, antiproton-to-proton flux ratio, and properties of elementary particle fluxes in primary cosmic rays measured with the alpha magnetic spectrometer on the international space station. *Phys. Rev. Lett.*, 117:091103, Aug 2016.

[25] M. Aguilar et al. The Alpha Magnetic Spectrometer (AMS) on the international space station: Part II — Results from the first seven years. *Phys. Rept.*, 894:1–116, 2021.

[26] S. Albergo et al. Light nuclei production in heavy ion collisions at relativistic energies. *Phys. Rev. C*, 65:034907, 2002.

[27] J. Altmann, A. Dubla, V. Greco, A. Rossi, and P. Skands. Towards the understanding of heavy quarks hadronization: from leptonic to heavy-ion collisions. 5 2024.

[28] Carl D Anderson. The positive electron. *Physical Review*, 43(6):491, 1933.

[29] Bo Andersson, Gösta Gustafson, Gunnar Ingelman, and Torbjörn Sjöstrand. Parton fragmentation and string dynamics. *Physics Reports*, 97(2-3):31–145, 1983.

[30] T Aramaki, CJ Hailey, SE Boggs, P Von Doetinchem, H Fuke, SI Mognet, RA Ong, K Perez, and J Zweerink. "antideuteron sensitivity for the gaps experiment". *Astroparticle Physics*, 74:6–13, 2016.

[31] Luísa Arruda, Fernando Barao, and Rui Pereira. Particle identification with the ams-02 rich detector: D/p and anti-d/anti-p separation. *arXiv preprint arXiv:0801.3243*, 2008.

[32] S. W. Barwick et al. Measurements of the cosmic ray positron fraction from 1-GeV to 50-GeV. *Astrophys. J. Lett.*, 482:L191–L194, 1997.

[33] Francesco Becattini. An introduction to the statistical hadronization model. *arXiv preprint arXiv:0901.3643*, 2009.

[34] Francesca Bellini and Alexander Philipp Kalweit. Testing production scenarios for (anti-)(hyper-)nuclei and exotica at energies available at the CERN Large Hadron Collider. *Phys. Rev. C*, 99(5):054905, 2019.

[35] Christian Bierlich et al. A comprehensive guide to the physics and usage of PYTHIA 8.3. *SciPost Phys. Codeb.*, 2022:8, 2022.

[36] Andy Buckley, Philip Ilten, Dmitri Konstantinov, Leif Lönnblad, James Monk, Witold Pokorski, Tomasz Przedzinski, and Andrii Verbytskyi. The HepMC3 event record library for Monte Carlo event generators. *Comput. Phys. Commun.*, 260:107310, 2021.

[37] S. T. Butler and C. A. Pearson. Deuterons from High-Energy Proton Bombardment of Matter. *Phys. Rev.*, 129:836–842, 1963.

[38] Owen Chamberlain, Emilio Segrè, Clyde Wiegand, and Thomas Ypsilantis. Observation of antiprotons. *Physical Review*, 100(3):947, 1955.

[39] Serguei Chatrchyan et al. Measurement of the Λ_b Cross Section and the $\bar{\Lambda}_b$ to Λ_b Ratio with $J/\Psi\Lambda$ Decays in pp Collisions at $\sqrt{s} = 7$ TeV. *Phys. Lett. B*, 714:136–157, 2012.

[40] S. Chekanov et al. Measurement of (anti)deuteron and (anti)proton production in DIS at HERA. *Nucl. Phys. B*, 786:181–205, 2007.

[41] Andrey E Egorov, Nikolay P Topchiev, Arkadiy M Galper, Oleg D Dalkarov, Alexey A Leonov, Sergey I Suchkov, and Yuriy T Yurkin. Dark matter searches by the planned gamma-ray telescope gamma-400. *Journal of Cosmology and Astroparticle Physics*, 2020(11):049, 2020.

[42] Philip Hauer. The upgraded ALICE TPC. *Nucl. Instrum. Meth. A*, 1039:167023, 2022.

[43] Sebastian Hornung. (Anti-)nuclei production and flow in pp, p–Pb and Pb–Pb collisions with ALICE. *PoS*, EPS-HEP2019:313, 2020.

[44] M. Kachelriess, S. Ostapchenko, and J. Tjemsland. Comment on "Dark Matter Annihilation Can Produce a Detectable Antihelium Flux through $\bar{\Lambda}_b$ Decays". 5 2021.

[45] M. Kachelriess, S. Ostapchenko, and J. Tjemsland. On nuclear coalescence in small interacting systems. *Eur. Phys. J. A*, 57(5):167, 2021.

[46] Joseph I. Kapusta. Mechanisms for deuteron production in relativistic nuclear collisions. *Phys. Rev. C*, 21:1301–1310, 1980.

[47] Michael Korsmeier, Fiorenza Donato, and Nicolao Fornengo. Prospects to verify a possible dark matter hint in cosmic antiprotons with antideuterons and antihelium. *Physical Review D*, 97(10):103011, 2018.

[48] Deepak Kumar. *Search for dark matter produced in association with a Higgs boson decaying to a pair of bottom quarks in proton-proton collisions at $\sqrt{s}$= 13 TeV using CMS 2017 and 2018 data*. PhD thesis, Indian Institute of Technology Madras (IN), 2023.

[49] Christian Lippmann. Upgrade of the ALICE Time Projection Chamber. Technical report, 3 2014.

[50] Chiara Lucarelli. Extending the physics reach of the fixed-target programme at the LHCb experiment, 2023. Presented 24 Jan 2024.

[51] Maximilian Mahlein, Luca Barioglio, Francesca Bellini, Laura Fabbietti, Chiara Pinto, Bhawani Singh, and Sushanta Tripathy. A realistic coalescence model for deuteron production. *Eur. Phys. J. C*, 83(9):804, 2023.

[52] Thomas Massam, Th Muller, B Righini, M Schneegans, and Antonino Zichichi. Experimental observation of antideuteron production. *Il Nuovo Cimento A*, 63:10–14, 1965.

[53] W. Menn et al. The PAMELA space experiment. *Adv. Space Res.*, 51:209–218, 2013.

[54] J.W. Mitchell et al. Precise measurements of the cosmic ray antiproton spectrum with bess including the effects of solar modulation. *Advances in Space Research*, 35(1):135–141, 2005. Mars International Reference Atmosphere, Living With a Star and Fundamental Physics.

[55] S. Navas et al. Review of particle physics. *Phys. Rev. D*, 110(3):030001, 2024.

[56] E. Norrbin and T. Sjostrand. Production and hadronization of heavy quarks. *Eur. Phys. J. C*, 17:137–161, 2000.

[57] University of Bologna Department of Physics and Astronomy A.Righi. Open Physics Hub. https://site.unibo.it/openphysicshub/en.

[58] C. Patrignani et al. Review of Particle Physics - Section 29.1. Primary spectra. *Chin. Phys. C*, 40(10):100001, 2016.

[59] Ivan Ravasenga. Commissioning and Performance of the New ALICE Inner Tracking System in the First Phase of LHC Run 3. *JPS Conf. Proc.*, 42:011002, 2024.

[60] Vera C Rubin. Dark matter in spiral galaxies. *Scientific American*, 248(6):96–109, 1983.

[61] N. Saffold et al. Cosmic antihelium-3 nuclei sensitivity of the GAPS experiment. *Astropart. Phys.*, 130:102580, 2021.

[62] Kenichi Sakai, K Abe, H Fuke, S Haino, T Hams, M Hasegawa, K Kim, M Lee, Y Makida, J Mitchell, et al. New result of antideuteron search in bess-polar ii. In *Proceedings of the 37th International Cosmic Ray Conference—PoS (ICRC2021), Berlin, Germany*, pages 12–23, 2021.

[63] Stefan Schael, R Barate, R Brunelière, I De Bonis, D Decamp, C Goy, S Jézéquel, J-P Lees, F Martin, E Merle, et al. Deuteron and anti-deuteron production in e+ e- collisions at the z resonance. *Physics Letters B*, 639(3-4):192–201, 2006.

[64] Rudiger Scheibl and Ulrich W. Heinz. Coalescence and flow in ultrarelativistic heavy ion collisions. *Phys. Rev. C*, 59:1585–1602, 1999.

[65] M Simon, A Molnar, and S Roesler. A new calculation of the interstellar secondary cosmic-ray antiprotons. *The Astrophysical Journal*, 499(1):250, 1998.

[66] Albert M Sirunyan et al. Measurement of b hadron lifetimes in pp collisions at $\sqrt{s} = 8$ TeV. *Eur. Phys. J. C*, 78(6):457, 2018. [Erratum: Eur.Phys.J.C 78, 561 (2018)].

[67] Peter Skands, Stefano Carrazza, and Juan Rojo. Tuning PYTHIA 8.1: the Monash 2013 Tune. *Eur. Phys. J. C*, 74(8):3024, 2014.

[68] F. Spada. Ams-02 on the international space station. *EPJ Web of Conferences*, 70, 03 2014.

[69] Maurizio Spurio. *Probes of Multimessenger Astrophysics. Charged cosmic rays, neutrinos, γ-rays and gravitational waves.* Astronomy and Astrophysics Library. Springer, 2018.

[70] Samuel J. Ting. Latest Results from the AMS Experiment on the International Space Station, CERN Colloquium, 2018.

[71] Shankar C. Venkataramani and Alan C. Newell. Pattern dark matter and galaxy scaling relations: Is dark matter the self-organized behavior and manifestation of things we already knew? *The European Physical Journal Special Topics*, 230(9):2139–2165, 2021.

[72] P Von Doetinchem, K Perez, T Aramaki, S Baker, S Barwick, R Bird, M Boezio, SE Boggs, M Cui, A Datta, et al. Cosmic-ray antinuclei as messengers of new physics: status and outlook for the new decade. *Journal of Cosmology and Astroparticle Physics*, 2020(08):035, 2020.

[73] Bryan R Webber. A qcd model for jet fragmentation including soft gluon interference. *Nuclear Physics B*, 238(3):492–528, 1984.

[74] Martin Wolfgang Winkler and Tim Linden. Dark matter annihilation can produce a detectable antihelium flux through λ^- b decays. *Physical Review Letters*, 126(10):101101, 2021.

[75] Martin Wolfgang Winkler and Tim Linden. Response to Comment on "Dark Matter Annihilation Can Produce a Detectable Antihelium Flux through $\bar{\Lambda}_b$ Decays". 5 2021.

[76] Robert B. Wiringa, V. G. J. Stoks, and R. Schiavilla. An Accurate nucleon-nucleon potential with charge independence breaking. *Phys. Rev. C*, 51:38–51, 1995.

[77] R. L. Workman et al. Review of Particle Physics. *PTEP*, 2022:083C01, 2022.

[78] T. Yoshida et al. Bess-polar experiment. *Advances in Space Research*, 33(10):1755–1762, 2004. The Next Generation in Scientific Ballooning.